Analysis of Pressurized Arch-Shells

By

Julian K. S. Goh

Thesis submitted to the Faculty of

Virginia Polytechnic Institute and State University

in partial fulfillment of the requirements for the degree of

MASTER OF SCIENCE

IN

CIVIL ENGINEERING

Approved by:

Raymond H. Plaut, Chairman

Siegfried M. Holzer

Rakesh K. Kapania

December 1998

Blacksburg, VA

Keywords: arch, Rayleigh-Ritz method, shell, snow load, structural analysis, wind load.

Analysis of Pressurized Arch-Shells

By

Julian K. S. Goh

Raymond H. Plaut, Chairman

Civil Engineering

(ABSTRACT)

A pressurized arch-shell structural component made of flexible material is considered. The component is inflated with high internal pressure. The behavior of similar types of structures, such as a pair of leaning pressurized arches and pressurized arch-supported membrane shelters, has been investigated in the past. More recently, several types of pressurized structures have been incorporated as part of the framework for a variety of structural systems. Particularly, the U.S. Army has been investigating the use of large lightweight and transportable pressurized arch-shell structures to be used as maintenance shelters for vehicles, helicopters, and airplanes.

The formulated equations using thin shell theory are applied to a pressurized arch-shell component. A numerical investigation based on the Rayleigh-Ritz method is utilized to determine the behavior of arch-shells under various types of loading. The types of loading include a uniformly distributed vertical load representing snow, a wind load, and a horizontal side load distributed along the arc length. Deflections, stress resultants, and moments at various locations are computed for two types of shapes: circular and non-circular arch-shells.

ACKNOWLEDGEMENTS

I wish to express my deepest appreciation and gratitude to Dr. Raymond Plaut for being an excellent advisor. He is always there for questions and advice, and is very dedicated and committed to his students. His guidance, patience, and invaluable advice have been extremely beneficial to this thesis. I would also like to thank Dr. Siegfried Holzer and Dr. Rakesh Kapania for their time, helpful suggestions, for reviewing my thesis, and for being members of my graduate committee.

My gratitude also goes to the U.S. Army Research Office which provided the financial support of this research under Grant No. DAA H04-95-1-0175.

I would also like to thank my friends. Thank you to Iskander Kurnia for the help with the Spider system. My sincere thanks goes to Dr. Lee Yew Haur for your friendship and support during my stay in Blacksburg. My sincerest gratitude goes to the Dasuki family for their love, support, and for accepting me as part of their family.

I also wish to express my deepest appreciation to my family for their love, support, and countless prayers. In particular, I thank my father for being such a wonderful mentor and role model. His dedication, commitment, and advice are invaluable in helping me to fulfill my dream. Also, I thank my sister Jasmine for her love and amazing patience and willingness to lend an ear or a hand whenever needed.

Finally and foremost, I would like to thank God for his guidance, grace, and mercy throughout this time of my life.

TABLE OF CONTENTS

LIST OF FIGURES

CHAPTER 1 INTRODUCTION

1.1 Overview

The U. S. Army has a science and technology objective to develop Large Area Night Maintenance Shelters (LANMaS). These large tent-like structures will provide maintenance capability for expensive vehicles, such as tanks and aircraft, under extreme environmental conditions like arctic and desert-like weather. The ideal properties of LANMaS include the following: low cost, lightweight, durable, and short setup and disassembly times. One of the possible support structures for LANMaS being considered is a single inflatable toroidal arch tube made of specially woven fabric. The fabric will most likely be made of non-homogeneous and orthotropic material to allow the desired arch shape to be achieved through inflation pressure.

1.2 Scope

This thesis investigates an arch-shell component in the form of a pressurized curved shell subjected to a variety of loading conditions. Formulated equations using thin shell theory from Kigudde (1996) are applied on the component to model the behavior under several types of service loads. A numerical investigation using the program Mathematica is applied to the formulated equations to find the displacements, moments, and stresses along the arch. The purpose is to compare the results using these formulated equations to other methods of analysis.

Two shapes of arch-shell are being considered, a circular arch-shell and a non-circular arch-shell. This allows the behavior of two forms of the structure to be analyzed and compared with each other under the various loadings. Four types of service loads are investigated: full and half snow load, wind load, and a uniform side load applied along the central half of the arc length between the bases. The properties of the arch-shell are similar to those used in the LANMaS.

This thesis is organized in the following manner. First, the formulated equations to analyze the arch-shell are described as well as the assumptions made for the analysis and the method of analysis. Next, the two different arch-shell shapes are considered. The results for the two general shapes are compared. Finally, conclusions and recommendations for further work are presented.

CHAPTER 2 LITERATURE REVIEW

2.1 Overview

The structure under investigation is a pressurized arch-shell structure. There have been a number of studies on the behavior of this type of structure using the finite element method. In this thesis, the Rayleigh-Ritz method is applied to the arch-shell to study its behavior under various types of loading. Presented here are some descriptions of previous investigations conducted on inflatable structures and fundamental theories related to this type of structure.

2.2 Pressurized-Arch Supported Membrane Structures

Some air-supported structures consist of a membrane connected to a stiff framework inflated by high-pressure air. The framework may consist of several inflated arch-shaped tubes. These tubes are made of fabric or some other flexible material, with an airtight liner, and they are lightweight, durable, and easy to transport and deploy. Several studies have been conducted on this type of structure to study their behavior under various types of service loads.

Carradine (1998) experimented with different scale models of arch-supported membrane shelters to investigate their behavior under wind and snow loading. Two scale models were tested, 1:100 and 1:50. Each model consisted of several arches placed vertically and several at the ends leaning away from the vertical at angles of 30°, 45°, and 60°. The difference between the two scale models was primarily the arch tubes; the larger scale model used a more flexible arch than the smaller scale model.

Carradine (1998) observed that the 1:100 scale model had a failure mode of tearing of the membrane under full snow load. The larger scale model of 1:50 failed when the vertical arches had a critical snap-through of the centers of the arches. This response

suggested that the failure mode for this type of structure depends largely on the strength of the supporting arches.

Kim et al. (1998) investigated a similar type of pressurized arch structure numerically through the finite element method. The arches and skin of the structure were modeled as thin shells, using the finite element computer software ABAQUS. The frameworks consisted of six vertical arches, and two at each end leaning at angles of 20° and 40°. The arch-shells had a parabolic shape and a circular cross section. At the supports, the arches were assumed to be fixed and each tube had an internal pressure of 500 kN. The structure was modeled with S4R rectangular shell elements for both the arches and the skin. Each arch was represented by 400 elements and the skin between adjacent arches was represented by 100 elements.

Kim et al. (1998) observed that the displacement under a symmetrical full snow load tends to increase as one moves away from the center of the structure in both vertical and horizontal displacement parallel to the longitudinal axis of the structure. For a snow load on one side only, the vertical displacements are much smaller than for the full snow load since the total load is less. The sideways displacements become more significant because of the asymmetrical loading. They also obtained vibration modes for the first few modes of the entire structure. These vibration modes can be used to model the response of the structure to dynamic loads, such as wind gusts or earthquakes. For the first mode, the structure sways back and forth to the side. The second mode depicts the structure twisting about a vertical axis through its center. In the third mode, the structure shows a vertical motion, up and down about the equilibrium configuration. When the top moves downward, the cross sections bulge outward at the sides, with the largest bulge occurring at the ends.

2.3 Flat Triangular Shell Element

Mohan and Kapania (1998a) investigated the large deformation of a shell element under deformation-dependent pressure loads. Deformation-dependent pressure loads

assume that the pressure load vectors are functions of the displacements and the changing directions affect the tangent stiffness matrix in a geometrically non-linear analysis. They applied a three-node flat triangular shell element in this analysis. This flat shell element is obtained by combining the Discrete Kirchhoff Theory (DKT) plate bending element and a membrane element similar to the Allman element.

They derived the pressure stiffness matrix and the deformation dependent pressure load vector in a Cartesian coordinate system using the principle of virtual work. They applied this new formulation to several types of large inflatable structures to determine the accuracy of the formulation in predicting the non-linearity of the structures. They investigated a cantilever arch-tube under uniform external pressure and compared the deformation results to those using the four-node curved shell element S4R from the finite element software ABAQUS. The results obtained were in good agreement. They also found that excluding the pressure stiffness matrix in the analysis significantly slowed down the rate of convergence of the solution, particularly for large deformations and rotations.

A thin circular arch under non-uniform pressure was also investigated. Under this analysis, the magnitude of the pressure distribution along the arch is treated as a function of the deformed configuration. They compared their formulation results with S4R and STRI3 elements of ABAQUS. STRI3 element refers to a flat triangular shell element in ABAQUS. From the results obtained, the formulation results are in good agreement with those of S4R, but not with the results obtained using STRI3. They believed that their formulation was more reliable due to the use of a better membrane representation than that used in STRI3.

Mohan and Kapania (1998b) also conducted a nonlinear analysis of a three node flat triangular element for thin laminated shells for three types of responses: large-rotation static response, dynamic response, and thermal post-buckling. Their objective was to find an inexpensive and simple thin shell element that has a good membrane representation. The element will be used for nonlinear analysis of large inflatable structures made of woven fabric composite. In their analysis, the rigid-body modes are

not removed and all nonlinear terms in the strain-displacement relations are considered for computing the stresses and the tangent stiffness matrix. They compared their results obtained from the nonlinear analysis with those obtained from S4R, STRI3, and S4R5 elements of ABAQUS. They found that, in general, their results agreed well with those from ABAQUS. In problems involving large rotations, their element requires more steps to obtain the convergence of the solution than the S4R element. However, their flat triangular element does not suffer from in-plane rotational singularity, shear-locking, etc. This indicates that the flat triangular element is very reliable for non-linear analysis of large flexible structures.

2.4 Leaning Arch-Shells

Molloy (1998) examined the behavior of a pair of pressurized leaning arch-shells under snow and wind loads. The finite element method was applied to a three-dimensional structure using shell elements. These elements allow the fabric and bladder to be modeled as a unit. A numerical investigation was conducted using the finite element analysis software ABAQUS. Four-node S4R shell elements with six degrees of freedom per node were utilized. Each arch was represented by 24 elements around the circumference of the cross section, 200 elements along the arc length, and 2 rings of elements for the disks at the bases. Geometric non-linearity was taken into account because of the large deflection expected for this type of structure.

He considered arch-shells of parabolic shape with a circular cross section. He assumed the material to be linear elastic, isotropic, and homogeneous. However, most woven or braided fabrics have different properties in various directions, which may significantly impact the behavior of the structure.

Two types of boundary conditions were considered: pinned and fixed bases. The leaning arches in Molloy's analysis had tilt angles of 15° and 30°. For each angle, three types of loads were applied: full snow load, half snow load, and wind load. The results of the analysis showed that buckling occurred for both full and half snow loads on arches with pinned bases tilted at both 15° and 30°; however, buckling only occurred for full

snow load on leaning arches with fixed bases tilted at 15°. The boundary conditions of the leaning arches played a significant impact on the behavior of the leaning arches. Fixed bases caused the structure to be much stiffer, stronger, and more stable, and to have higher vibration frequencies compared with the case of pinned bases.

Molloy (1998) found that the first vibration mode was often a twisting mode for pinned arches and a side-sway mode for fixed arches. This suggested that the lower restraint at the pinned bases causes the pinned arches to be much weaker in twisting than the fixed arches. His analysis also found that leaning arches were a more efficient structure than a single arch. In one comparison, a single arch with fixed bases buckled at a total load of 45 kN, whereas a pair of leaning arches tilted at 15° buckled at 253 kN. The addition of a second arch increased the load carrying capacity of the structure by five and a half times in this example.

2.5 Sanders' Linear Elastic Thin Shell Theory

Linear theories of thin shells are primarily based on Love's first approximation and second approximation of thin shells or slight modifications of them. The main difference between Love's approximation theories is that the first approximation neglects the effects of transverse shear and normal strain. These assumptions lead to an inconsistency as not all strains vanish for small rigid-body rotations of the shell. Sanders (1959) derived an improved first approximation theory for thin shells, which removed the inconsistency without complicating the system of equilibrium equations.

His modified first approximation theory is almost entirely developed as a two-dimensional one with the use of the principle of virtual work in the derivation. It is not based on three-dimensional equations of elasticity or on a variational principle. The numerical results obtained for displacements, stresses, and moments are based on the use of lines of curvature as coordinate curves in the middle surface. The compatibility equations for the strain quantities involve the stress resultants and couples in terms of a

set of stress functions. These expressions for stress quantities satisfy the equilibrium equations for thin shells identically.

Zhang and Redekop (1992b and 1992c) published several papers in which they investigated the behavior of a toroidal shell using Sanders' thin shell theory. They investigated local loads on a toroidal shell and surface loading of a thin-walled toroidal shell. In both cases, they developed equations based on toroidal coordinates and solved the case of a pad load of uniform normal pressure. Numerical results were obtained from Sanders' equilibrium equations and were compared with results from the finite element method. All results assumed linear elastic, small displacement behavior. They found that results from Sanders' equilibrium equations agreed very closely with results from the finite element method.

Zhang and Redekop (1992a) also compared elastic solutions for three-point bending of curved pipes based on two theories, Mushtari-Vlasov-Donnell (MVD) theory and Sanders' thin shell theory, to solutions from the finite element method. For all cases, a pad load of uniform normal pressure was applied. They concluded that Sanders theory is superior to MVD theory, as the results obtained for curved pipes based on Sanders' theory agreed well with results from the finite element method.

CHAPTER 3 METHOD OF ANALYSIS

3.1 Material

In the general formulation, the arch-shell material is assumed to be a non-homogeneous, linearly elastic, and orthotropic material. In the numerical examples, the special case of a homogeneous, isotropic material will be considered.

3.2 Geometry of the Mid-surface

The equations in this section are taken from Kigudde (1996). The geometry of the mid-surface of the arch-shell is defined by two independent coordinates, f and s. The coordinate f is the angle between the axis of the cross section lying in the x-y plane and a line drawn from the center of the cross section to a point on the mid-surface, and is measured positive as shown in Fig. 3.1. The coordinate s is the arc length from the global y-axis along the locus of the center of the cross sections with the top of the arch being the origin. The arch-shell in this study will consist of two types of shapes: a half circle and a shape with curvature assumed to be a quadratic function of arc length. Both shapes will have a circular cross section (r = constant) in the numerical examples as shown in Fig. 3.2. The arch-shell is geometrically symmetric about the x-y and y-z planes.

The locus of the center of the cross sections in the global x-y plane is shown as the dashed line in Fig. 3.1. It is defined by a function f (x) in the global x-y plane:

$$y = f(x) \tag{3.2.1}$$

The slope in the x-y plane at any position s on the locus is:

$$y' = \frac{dy}{dx} \tag{3.2.2}$$

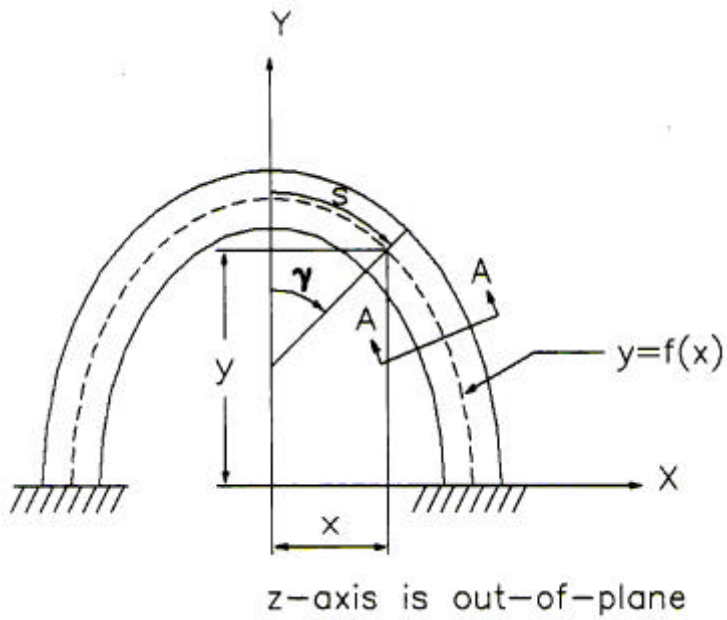

Figure 3.1 Mid-surface Profile of Arch

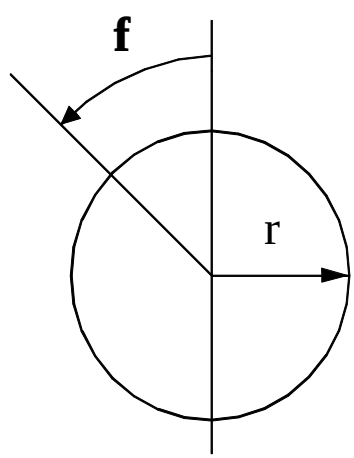

Section A - A

Figure 3.2 Cross Section of Arch

The angle γ between the global y-axis and the normal to the locus in the x-y plane satisfies:

$$\sin\ g = \frac{-y'}{\sqrt{1+(y')^2}} \tag{3.2.3}$$

$$\cos\ g = \frac{1}{\sqrt{1+(y')^2}} \tag{3.2.4}$$

The arc length is:

$$s = \int_0^x \sqrt{1+(y')^2}\ dx \tag{3.2.5}$$

Differentiating (3.2.5) with respect to x gives:

$$\frac{ds}{dx} = \sqrt{1+(y')^2} \tag{3.2.6}$$

The radius of the cross section is assumed to be a function of the angle ϕ but not a function of *s*:

$$r = r(f) \tag{3.2.7}$$

The position vector $\bar{r}$ of any point on the mid-surface relative to the origin can be expressed in terms of the two independent coordinates f and *s*, and unit vectors $\hat{i}, \hat{j}, \hat{k}$ parallel to the global x, y, and z axes, respectively:

$$\bar{r} = (x + r\sin\ g\cos f)\hat{i} + (y + r\cos\ g\cos f)\hat{j} + (r\sin\ f)\hat{k} \tag{3.2.8}$$

3.2.1 Lamé Parameters A_ϕ and A_s

The Lamé parameter A_ϕ is defined by:

$$A_f = \left| \frac{\partial \bar{r}}{\partial f} \right| \tag{3.2.9}$$

where $\frac{\partial \bar{r}}{\partial f}$ is the tangent to the principal curve of constant coordinate s. Using (3.2.8):

$$\begin{aligned} \frac{\partial \bar{r}}{\partial f} &= (r' \cos f - r \sin f) \sin g \hat{i} + (r' \cos f - r \sin f) \cos g \hat{j} \\ &\quad + (r' \sin f + r \cos f) \hat{k} \end{aligned} \tag{3.2.10}$$

where $r' = \frac{dr}{df}$ is the variation of the radius of the cross section with respect to f. From (3.2.9) and (3.2.10), one obtains:

$$A_f = \sqrt{(r)^2 + (r')^2} \tag{3.2.11}$$

For a circular cross section of radius r, $A_f = r$.

The Lamé parameter A_s is defined by:

$$A_s = \left| \frac{\partial \bar{r}}{\partial s} \right| \tag{3.2.12}$$

where $\frac{\partial \bar{r}}{\partial s}$ is the tangent to the principal curve of constant coordinate f. It can be written as:

$$\frac{\partial \bar{r}}{\partial s} = \frac{\partial \bar{r}}{\partial x}\frac{\partial x}{\partial s} \tag{3.2.13}$$

Differentiating (3.2.3), (3.2.4) and (3.2.8) with respect to x yields the following:

$$\frac{d}{dx}(\sin\ g) = k\,, \qquad \frac{d}{dx}(\cos\ g) = y'k\,, \tag{3.2.14}$$

$$\frac{\partial \bar{r}}{\partial x} = (1 + r\,k\cos f)\hat{i} + y'(1 + r\,k\cos f)\hat{j} \tag{3.2.15}$$

where κ, the negative of the curvature of the locus, is

$$k = \frac{-y''}{[1 + (y')^2]^{\frac{3}{2}}} \tag{3.2.16}$$

From (3.2.6):

$$\frac{dx}{ds} = \frac{1}{\sqrt{1 + (y')^2}} \tag{3.2.17}$$

Using (3.2.12), (3.2.13), (3.2.15), and (3.2.17), the following is obtained:

$$A_s = 1 + r\,k\cos f \tag{3.2.18}$$

According to Dym (1990), $F = M = 0$ are the necessary conditions for f and s to be principal coordinates. F and M are the vector dot products:

$$F = \frac{\partial \bar{r}}{\partial f} \bullet \frac{\partial \bar{r}}{\partial s} \qquad M = -\hat{n} \bullet \frac{\partial^2 \bar{r}}{\partial f\,\partial s} \tag{3.2.19}$$

Following Kigudde (1996), using (3.2.10), (3.2.13), (3.2.15), and (3.2.17), F becomes

$$F = \frac{(1 + rk\cos f)(r'\cos f - r\sin f)(\sin g + y'\cos g)}{\sqrt{1 + (y')^2}} \tag{3.2.20}$$

Using (3.2.14), this gives $F = 0$.

For the vector dot product in M,

$$\frac{\partial^2 \bar{r}}{\partial f \partial s} = \frac{\partial}{\partial f}\left(\frac{\partial \bar{r}}{\partial s}\right) = \frac{k(r'\cos f - r\sin f)\hat{i} + y'k(r'\cos f - r\sin f)\hat{j}}{\sqrt{1 = (y')^2}} \tag{3.2.21}$$

$$\hat{n} = \frac{\bar{g}}{|\bar{g}|} \tag{3.2.22}$$

where

$$\bar{g} = \frac{\partial \bar{r}}{\partial f} \times \frac{\partial \bar{r}}{\partial s} = \frac{\begin{vmatrix} \hat{i} & \hat{j} & \hat{k} \\ (r'\cos f - r\sin f)\sin g & (r'\cos f - r\sin f)\cos g & (r'\sin f + r\cos f) \\ (1 + rk\cos f) & y'(1 + rk\cos f) & 0 \end{vmatrix}}{\sqrt{1 + (y')^2}} \tag{3.2.23}$$

(3.2.23) can be simplified as

$$\bar{g} = \frac{\{1 + rk\cos f\}\begin{Bmatrix} -y'(r'\sin f + r\cos f)\hat{i} + (r'\sin f + r\cos f)\hat{j} \\ -(r'\cos f - r\sin f)(\sec g)\hat{k} \end{Bmatrix}}{\sqrt{1 + (y')^2}} \tag{3.2.24}$$

With the use of (3.2.11), (3.2.18), and (3.2.24),

$$|\bar{g}| = (1 + rk\cos f)\sqrt{(r)^2 + (r')^2} = A_s A_f \tag{3.2.25}$$

Thus,

$$\hat{n} = \frac{\bar{g}}{A_f A_s} \tag{3.2.26}$$

This leads to

$$\hat{n} = \frac{-y'(r'\sin f + r\cos f)\hat{i} + (r'\sin f + r\cos f)\hat{j} - (r'\cos f - r\sin f)(\sec g)\hat{k}}{A_f\sqrt{1+(y')^2}} \tag{3.2.27}$$

where $\hat{n}$ is the unit normal vector to the mid-surface (positive if outward). From (3.2.19), (3.2.21), and (3.2.27), it follows that $M = 0$.

Since $F = M = 0$, f and s are principal coordinates. This allows the maximum and minimum curvatures for any given point on the mid-surface of the arch to be located along the f and s coordinate lines. Therefore, the Lamé parameters derived in this section and the principal curvatures to be derived in section 3.2.2 are applicable to the equilibrium and strain-displacement relations, which are based on lines of principal curvature. The strain-displacement and equilibrium relations will be discussed in sections 3.3 and 3.4, respectively.

3.2.2 Principal Radii of Curvature

Having established f and s as principal coordinates, formulae given by Dym (1990) are used to calculate the principal curvatures that appear in the strain-displacement and equilibrium expressions. The principal radii of curvature R_ϕ and R_s in the f and s directions, respectively, are expressed as follows (Kigudde, 1996):

$$\frac{1}{R_f} = \frac{L}{E} \quad , \quad \frac{1}{R_s} = \frac{N}{G} \tag{3.2.28}$$

where E, G, L, and N are vector dot products given by

$$E = \frac{\partial \bar{r}}{\partial f} \bullet \frac{\partial \bar{r}}{\partial f} = (A_f)^2 \qquad , \qquad G = \frac{\partial \bar{r}}{\partial s} \bullet \frac{\partial \bar{r}}{\partial s} = (A_s)^2 ,$$

$$L = -\hat{n} \bullet \frac{\partial^2 \bar{r}}{\partial f^2} \qquad , \qquad N = -\hat{n} \bullet \frac{\partial^2 \bar{r}}{\partial s^2} \tag{3.2.29}$$

According to Kigudde (1996), the second partial derivatives of the position vector (with respect to f and s) used in L and N in (3.2.29) are given in the following:

$$\begin{aligned} \frac{\partial^2 \bar{r}}{\partial s^2} &= (r'' \cos f - 2r' \sin f - r \cos f)(\sin g)\hat{i} \\ &+ (r'' \cos f - 2r' \sin f - r \cos f)(\cos g)\hat{j} \\ &+ (r'' \sin f + 2r' \cos f - r \sin f)\hat{k} \end{aligned} \tag{3.2.30}$$

where

$$r' = \frac{dr}{df} \qquad , \qquad r'' = \frac{d^2 r}{df^2}$$

and

$$\frac{\partial^2 \bar{r}}{\partial s^2} = \frac{\partial}{\partial x}\left(\frac{\partial \bar{r}}{\partial s}\right)\frac{dx}{ds} \tag{3.2.31}$$

Applying (3.2.13), (3.2.14), (3.2.15), and (3.2.17) into (3.2.31), one obtains

$$\frac{\partial^2 \bar{r}}{\partial s^2} = \frac{1}{1 + (y')^2} \left\{ \begin{array}{c} [y' k(1 + rk \cos f)\sqrt{1 + (y')^2} + rk' \cos f]\hat{i} \\ + [(y')^2 k(1 + rk \cos f)\sqrt{1 + (y')^2} + y''(1 + rk \cos f) + y' rk' \cos f]\hat{j} \end{array} \right\} \tag{3.2.32}$$

where

y' is defined in (3.2.2)

κ is defined in (3.2.16)

$$y'' = \frac{dr}{df}$$

$$k' = \frac{dk}{dx}$$

If the radius r of the cross section is constant, $r' = 0$ and $r'' = 0$, and from (3.2.3), (3.2.4), (3.2.16), (3.2.22), and (3.2.24):

$$E = r^2 \quad , \quad G = (1 + rk\cos f)^2 \quad ,$$
$$L = r \quad , \quad N = (1 + rk\cos f)k\cos f \qquad (3.2.33)$$

Then, from (3.2.28),

$$R_f = r \quad , \quad R_s = r + \frac{1}{k\cos f} \qquad (3.2.34)$$

when r is independent of s and f, and k may be a function of s.

3.3 Strain-Displacement Relationships

The strain-displacement relations of Sanders (1959) are applied. According to Kirchhoff's assumptions for non-deformable normals and transverse shears, normal strains are neglected (Jones, 1975). These assumptions allow us to express the changes in curvatures and torsion strains directly in terms of the mid-surface translational displacements u_f, u_s, and w. The strain-displacement relations are as follows (Gould, 1988):

$$e_f = \frac{1}{A_f}\frac{\partial u_f}{\partial f} + \frac{1}{A_f A_s}\frac{\partial A_f}{\partial s}u_s + \frac{w}{R_f} \quad , \qquad (3.3.1)$$

$$e_s = \frac{1}{A_s}\frac{\partial u_s}{\partial s} + \frac{1}{A_f A_s}\frac{\partial A_s}{\partial f}u_f + \frac{w}{R_s} \quad , \tag{3.3.2}$$

$$g_{fs} = \frac{1}{A_f A_s}(A_s\frac{\partial u_s}{\partial f} + A_f\frac{\partial u_f}{\partial s} - \frac{\partial A_f}{\partial s}u_f - \frac{\partial A_s}{\partial f}u_s) \quad , \tag{3.3.3}$$

$$k_f = \frac{1}{A_f}\frac{\partial}{\partial f}(\frac{u_f}{R_f} - \frac{1}{A_f}\frac{\partial w}{\partial f}) + \frac{1}{A_f A_s}\frac{\partial A_f}{\partial s}(\frac{u_s}{R_s} - \frac{1}{A_s}\frac{\partial w}{\partial s}) \quad , \tag{3.3.4}$$

$$k_s = \frac{1}{A_s}\frac{\partial}{\partial s}(\frac{u_s}{R_s} - \frac{1}{A_s}\frac{\partial w}{\partial s}) + \frac{1}{A_f A_s}\frac{\partial A_s}{\partial f}(\frac{u_f}{R_f} - \frac{1}{A_f}\frac{\partial w}{\partial f}) \quad , \tag{3.3.5}$$

$$\begin{aligned}\bar{k}_{fs} = \frac{1}{2A_f A_s}\{&A_s\frac{\partial}{\partial f}(\frac{u_s}{R_s} - \frac{1}{A_s}\frac{\partial w}{\partial s}) + A_f\frac{\partial}{\partial s}(\frac{u_f}{R_f} - \frac{1}{A_f}\frac{\partial w}{\partial f}) \\ &- \frac{\partial A_f}{\partial s}(\frac{u_f}{R_f} - \frac{1}{A_f}\frac{\partial w}{\partial f}) - \frac{\partial A_s}{\partial f}(\frac{u_s}{R_s} - \frac{1}{A_s}\frac{\partial w}{\partial s}) \\ &+ \frac{1}{2}(\frac{1}{R_s} - \frac{1}{R_f})[\frac{\partial}{\partial f}(A_s u_s) - \frac{\partial}{\partial s}(A_f u_f)]\}\end{aligned} \tag{3.3.6}$$

where

e_f and e_s are the extensional strains in the f and s directions, respectively

g_{fs} is the in-plane shearing strain

k_f and k_s are the changes in curvature in the f and s directions, respectively

k_{fs} and k_{sf} are the twisting strains of the arch-shell

$\bar{k}_{fs} = \frac{1}{2}(k_{fs} + k_{sf})$

A_f, A_s, R_f, and R_s are defined in sections 3.2.1 and 3.2.2

u_f and u_s are mid-surface displacements in the local f and s directions, respectively

w is the displacement normal to the mid-surface (w is positive on a surface of positive Gaussian curvature if it points away from the two centers of principal curvature)

3.4 Equilibrium Equations

The shell equilibrium equations are applied to determine the stresses in the arch-shell due to the applied loads. The contribution of the bending stiffness to the overall stiffness of the material is considered to be significant under the external loading. The load acting on the surface, at any point on the arch-shell, can be decomposed into three traction forces, q_f, q_s, and q_n acting in the f, s and normal direction, respectively. The traction forces can either be functions of coordinates f and s, or constant, depending on the loading under consideration. Figure 3.3 shows a differential shell element on the mid-surface, with in-plane stress resultants and surface traction forces acting on it. Figure 3.4 depicts the same differential shell element with the resultant moments acting on it. Both the summations of all forces and moments in any direction must equal zero in order for the element to be in equilibrium.

The following equations are the Sanders' equilibrium equations (Sanders, 1959) without any prestressing terms:

$$\frac{\partial}{\partial f}(A_s N_f) + \frac{\partial}{\partial s}(A_f \overline{N}_{fs}) + \frac{\partial A_f}{\partial s}\overline{N}_{fs} - \frac{\partial A_s}{\partial f}N_s + \frac{A_f A_s}{R_f}Q_f + \frac{1}{2}A_f\frac{\partial}{\partial s}[(\frac{1}{R_f} - \frac{1}{R_s})\overline{M}_{fs}] = -A_f A_s q_f \tag{3.4.1}$$

$$\frac{\partial}{\partial s}(A_f N_s) + \frac{\partial}{\partial f}(A_s \overline{N}_{fs}) + \frac{\partial A_s}{\partial f}\overline{N}_{fs} - \frac{\partial A_f}{\partial s}N_f + \frac{A_f A_s}{R_s}Q_s + \frac{1}{2}A_s\frac{\partial}{\partial f}[(\frac{1}{R_s} - \frac{1}{R_f})\overline{M}_{fs}] = -A_f A_s q_s \tag{3.4.2}$$

$$\frac{\partial}{\partial f}(A_s Q_f) + \frac{\partial}{\partial s}(A_f Q_s) - (\frac{N_f}{R_f} + \frac{N_s}{R_s})A_f A_s = -A_f A_s q_n \tag{3.4.3}$$

$$\frac{\partial}{\partial f}(A_s M_f) + \frac{\partial}{\partial s}(A_f \overline{M}_{fs}) + \frac{\partial A_f}{\partial s}\overline{M}_{fs} - \frac{\partial A_s}{\partial f}M_s - A_f A_s Q_f = 0 \tag{3.4.4}$$

$$\frac{\partial}{\partial s}(A_f M_s) + \frac{\partial}{\partial f}(A_s \overline{M}_{fs}) + \frac{\partial A_s}{\partial f}\overline{M}_{fs} - \frac{\partial A_f}{\partial s}M_f - A_f A_s Q_s = 0 \tag{3.4.5}$$

where

N_f and N_s are the normal stress resultants in the f and s directions, respectively

N_{fs} and N_{sf} are the in-plane shear stress resultants

$\overline{N}_{fs} = \frac{1}{2}(N_{fs} + N_{sf})$

M_f and M_s are the resultant bending moments, per unit length

$\overline{M}_{fs} = \frac{1}{2}(M_{fs} + M_{sf})$ where M_{fs} and M_{sf} are the stress couples, per unit length

q_f, q_s, and q_n are surface traction forces, per unit area, acting on the element in the f, s and normal directions, respectively

Q_f and Q_s are the transverse shear stress resultants

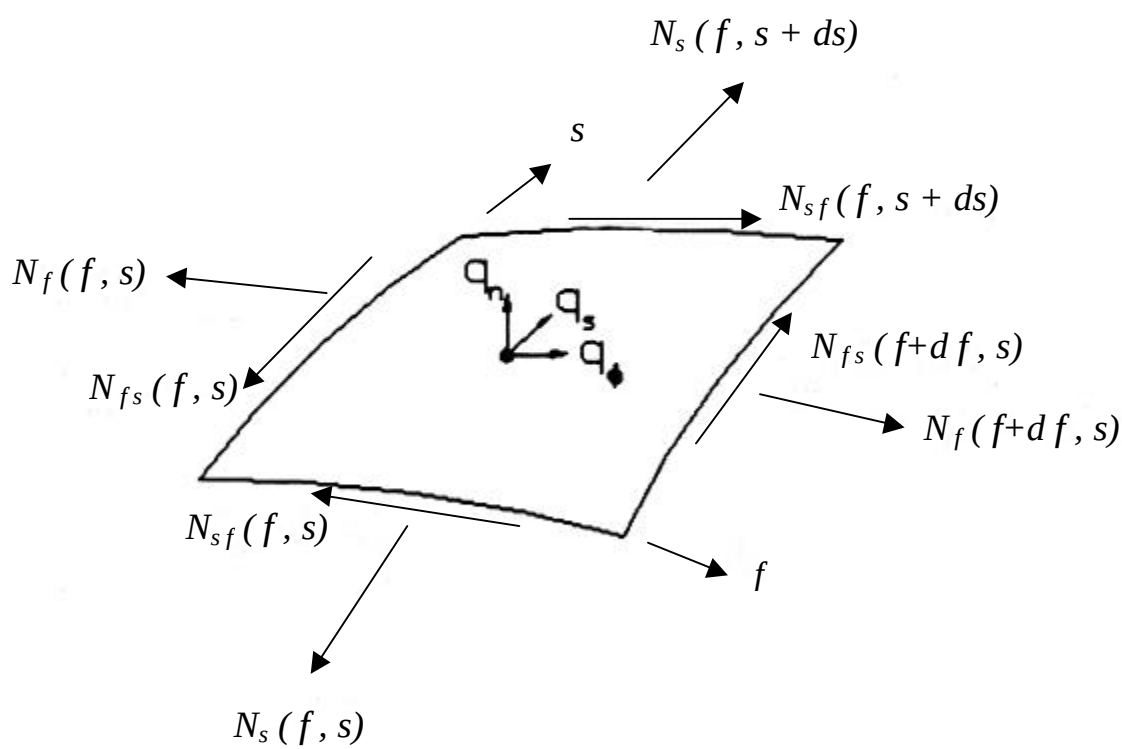

Figure 3.3 Differential element with tractions and stress resultants

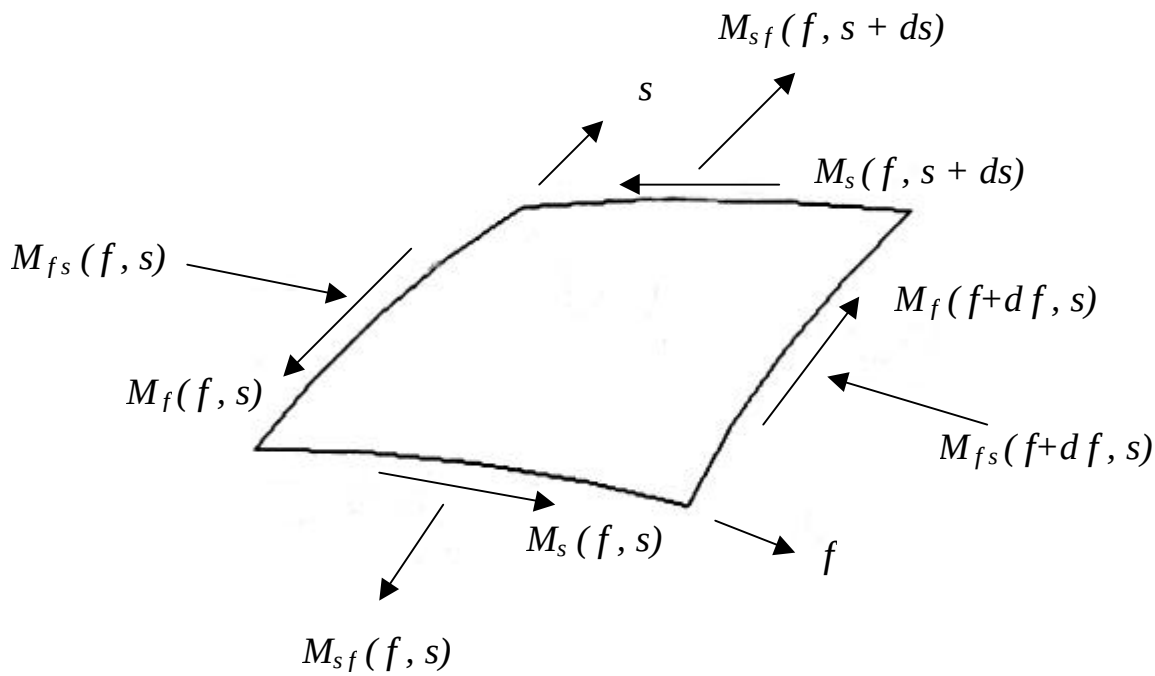

Figure 3.4 Differential element with resultant moments

Solving for Q_f and Q_s in (3.4.4) and (3.4.5), we obtain the following equations:

$$Q_f = \frac{1}{A_f A_s}[\frac{\partial}{\partial f}(A_s M_f) + \frac{\partial}{\partial s}(A_f \overline{M}_{fs}) + \frac{\partial A_f}{\partial s}\overline{M}_{fs} - \frac{\partial A_s}{\partial f}M_s] \quad , \qquad (3.4.6)$$

$$Q_s = \frac{1}{A_f A_s}[\frac{\partial}{\partial s}(A_f M_s) + \frac{\partial}{\partial f}(A_s \overline{M}_{fs}) + \frac{\partial A_s}{\partial f}\overline{M}_{fs} - \frac{\partial A_f}{\partial s}M_f] \quad , \qquad (3.4.7)$$

Substituting these expressions for Q_f and Q_s into (3.4.1) - (3.4.3), we obtain the following three differential equations:

$$\frac{\partial}{\partial f}(A_s N_f) + \frac{\partial}{\partial s}(A_f \overline{N}_{fs}) + \frac{\partial A_f}{\partial s}\overline{N}_{fs} - \frac{\partial A_s}{\partial f}N_s + \frac{1}{R_f}\frac{\partial}{\partial f}(A_s M_f)$$

$$+ \frac{1}{R_f}\frac{\partial}{\partial s}(A_f \overline{M}_{fs}) + \frac{1}{R_f}\frac{\partial A_f}{\partial s}\overline{M}_{fs} - \frac{1}{R_f}\frac{\partial A_s}{\partial f}M_s \tag{3.4.8}$$

$$+ \frac{1}{2}A_f \frac{\partial}{\partial s}[(\frac{1}{R_f} - \frac{1}{R_s})\overline{M}_{fs}] = -A_f A_s q_f$$

$$\frac{\partial}{\partial s}(A_f N_s) + \frac{\partial}{\partial f}(A_s \overline{N}_{fs}) + \frac{\partial A_s}{\partial f}\overline{N}_{fs} - \frac{\partial A_f}{\partial s}N_f + \frac{1}{R_s}\frac{\partial}{\partial s}(A_f M_s)$$

$$+ \frac{1}{R_s}\frac{\partial}{\partial f}(A_s \overline{M}_{fs}) + \frac{1}{R_s}\frac{\partial A_s}{\partial f}\overline{M}_{fs} - \frac{1}{R_s}\frac{\partial A_f}{\partial s}M_f \tag{3.4.9}$$

$$+ \frac{1}{2}A_s \frac{\partial}{\partial f}[(\frac{1}{R_s} - \frac{1}{R_f})\overline{M}_{fs}] = -A_f A_s q_s$$

$$\frac{\partial}{\partial f}\{\frac{1}{A_f}[\frac{\partial}{\partial f}(A_s M_f) + \frac{\partial}{\partial s}(A_f \overline{M}_{fs}) + \frac{\partial A_f}{\partial s}\overline{M}_{fs} - \frac{\partial A_s}{\partial f}M_s]\}$$

$$+ \frac{\partial}{\partial s}\{\frac{1}{A_s}[\frac{\partial}{\partial s}(A_f M_s) + \frac{\partial}{\partial f}(A_s \overline{M}_{fs}) + \frac{\partial A_s}{\partial f}\overline{M}_{fs} - \frac{\partial A_f}{\partial s}M_f]\} \tag{3.4.10}$$

$$- (\frac{N_f}{R_f} + \frac{N_s}{R_s})A_f A_s = -A_f A_s q_n$$

Sanders' equilibrium equations with prestressing require additional terms in (3.4.8) - (3.4.10) due to the stress resultants T_f, T_s, and T_{fs} from internal pressure. As a result (Plaut, 1998),

$$-\frac{A_f A_s}{R_f} b_f T_f \tag{3.4.11}$$

are added to the left side of (3.4.8),

$$-\frac{A_f A_s}{R_s} b_s T_s \tag{3.4.12}$$

are added to the left side of (3.4.9), and

$$-\frac{\partial}{\partial f}(A_s b_f T_f) - \frac{\partial}{\partial s}(A_f b_s T_s) \tag{3.4.13}$$

are added to the left side of (3.4.10), where

$$b_f = \frac{u_f}{R_f} - \frac{1}{A_f}\frac{\partial w}{\partial f} \quad , \qquad b_s = \frac{u_s}{R_s} - \frac{1}{A_s}\frac{\partial w}{\partial s} \tag{3.4.14}$$

3.5 Prestress due to Internal Pressure

The arch-shell is subjected to internal pressure p. It is assumed that the bending stresses under this initial pressure are negligible. Therefore, the membrane stress resultants T_f, T_s, and T_{fs} form the initial stress state.

To determine these prestresses, (3.4.8) – (3.4.10) are used with

$$\begin{aligned} N_f &= T_f \quad , & N_s &= T_s \quad , & \overline{N}_{fs} &= T_{fs} \quad , \\ M_f &= 0 \quad , & M_s &= 0 \quad , & \overline{M}_{fs} &= 0 \quad , \\ q_f &= 0 \quad , & q_s &= 0 \quad , & q_n &= p \end{aligned} \tag{3.5.1}$$

Also, with r constant, $A_f = r$ is constant. Then (3.4.8) – (3.4.10) become:

$$\frac{\partial}{\partial f}(A_s T_f) + r\frac{\partial T_{fs}}{\partial s} - \frac{\partial A_s}{\partial f}T_s = 0 \quad , \tag{3.5.2}$$

$$r\frac{\partial T_s}{\partial s} + \frac{\partial}{\partial f}(A_s T_{fs}) + \frac{\partial A_s}{\partial f}T_{fs} = 0 \quad , \tag{3.5.3}$$

$$\frac{T_f}{R_f} + \frac{T_s}{R_s} = p \tag{3.5.4}$$

With the use of (3.2.18) and (3.2.26), where r is constant and k can depend on s, the solution to (3.5.2) – (3.5.4) is (Plaut, 1997):

$$T_f = \frac{pr(2 + r\,k\cos f)}{2(1 + r\,k\cos f)} \quad , \quad T_s = \frac{pr}{2} \quad , \quad T_{fs} = 0 \qquad (3.5.5)$$

3.6 Constitutive Laws

The material properties are orthotropic and change continuously from point to point on the mid-surface of the arch-shell. The loads are conservative and the resulting slopes and deflections are small.

By applying the general orthotropic equations for laminated plates in Jones (1975) to the coordinates used for this analysis, the following stress and moment equations are obtained:

$$N_f = A_{11}(e_f + n_s e_s) \quad , \quad A_{11} = \frac{E_f h}{1 - n_f n_s} \quad , \qquad (3.6.1)$$

$$N_s = A_{22}(e_s + n_f e_f) \quad , \quad A_{22} = \frac{E_s h}{1 - n_f n_s} \quad , \qquad (3.6.2)$$

$$\overline{N}_{fs} = A_{66}\, g_{fs} \quad , \quad A_{66} = G_{fs} h \quad , \qquad (3.6.3)$$

$$M_f = D_{11}(k_f + n_s k_s) \quad , \quad D_{11} = \frac{E_f h^3}{12(1 - n_f n_s)} \quad , \qquad (3.6.4)$$

$$M_s = D_{22}(k_s + n_f k_f) \quad , \quad D_{22} = \frac{E_s h^3}{12(1 - n_f n_s)} \quad , \qquad (3.6.5)$$

$$\overline{M}_{fs} = 2D_{66}\overline{k}_{fs} \quad , \quad D_{66} = \frac{G_{fs} h^3}{12} \qquad (3.6.6)$$

where

G_{fs} is the in-plane shear modulus

h is the material thickness

E_f and E_s are the moduli of elasticity in the f and s directions, respectively

n_f and n_s are the Poisson's ratios in the f and s directions, respectively

A_{ij} and D_{ij} are the stiffness coefficients

3.7 Boundary Conditions

The arc length from the center of the arch-shell to each base is s_0. At each base, it is assumed that the displacement u_s along the arc length is zero, the circumferential displacement u_f is not constrained, and the radial displacement w is restrained by line springs with a high stiffness C per unit length (i.e., C has units of force per length squared). Figure 3.5 depicts the boundary conditions of the arch-shell in the circular case with s_0 = 50. It is assumed that $\partial w/\partial s$ is zero at the bases.

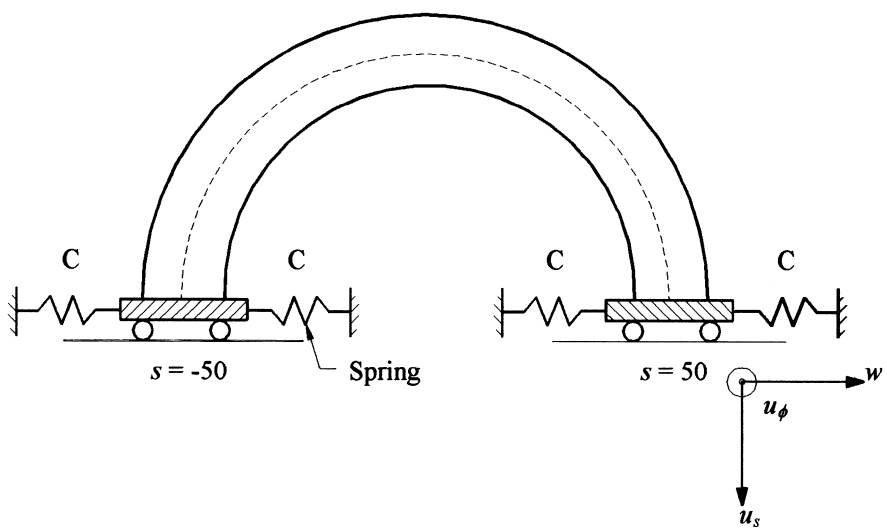

Figure 3.5 Boundary condition with line springs

3.8 Energy

The elastic strain energy stored in the arch-shell is:

$$U_E = \frac{1}{2}\int_{-s_0}^{s_0}\int_0^{2p} (N_f e_f + N_s e_s + \overline{N}_{fs}\, g_{fs} + M_f k_f + M_s k_s + 2\overline{M}_{fs}\, \overline{k}_{fs}) A_f A_s \, df\, ds \tag{3.8.1}$$

With the use of (3.6.1) – (3.6.6) and (Jones 1975; Reddy, 1984)

$$A_{12} = A_{11} n_s = A_{22} n_f \quad , \quad D_{12} = D_{11} n_s = D_{22} n_f \tag{3.8.2}$$

we can write (3.8.1) as

$$U_E = \frac{1}{2}\int_{-s_0}^{s_0}\int_0^{2p} (A_{11} e_f^{\,2} + 2A_{12} e_f e_s + A_{22} e_s^{\,2} + A_{66}\, g_{fs}^{\,2}) A_f A_s \, df\, ds + \frac{1}{2}\int_{-s_0}^{s_0}\int_0^{2p} (D_{11} k_f^{\,2} + 2D_{12} k_f k_s + D_{22} k_s^{\,2} + 4D_{66} \overline{k}_{fs}^{\,2}) A_f A_s \, df\, ds \tag{3.8.3}$$

The potential energy due to the initial stress resultants T_f, and T_s acting on the additional displacements due to the external loads is:

$$U_I = \frac{1}{2}\int_{-s_0}^{s_0}\int_0^{2p} [T_f (\frac{u_f}{R_f} - \frac{1}{A_f}\frac{\partial w}{\partial f})^2 + T_s (\frac{u_s}{R_s} - \frac{1}{A_s}\frac{\partial w}{\partial s})^2] A_f A_s \, df\, ds \tag{3.8.4}$$

The energy stored in the springs at the bases is:

$$U_B = \frac{1}{2} C \int_0^{2p} w^2(-s_0, f) df + \frac{1}{2} C \int_0^{2p} w^2(s_0, f) df \tag{3.8.5}$$

Finally, the potential of the external loads is:

$$U_L = -\int_{-s_0}^{s_0}\int_0^{2p} (q_f u_f + q_s u_s + q_n w) A_f A_s \, d\,f\, ds \tag{3.8.6}$$

Therefore the total potential energy U is given by:

$$U = U_E + U_I + U_B + U_L \tag{3.8.7}$$

where the strains and changes in curvature are defined in section 3.3 and the stiffness coefficients (A_{ij}'s and D_{ij}'s) are defined in section 3.6. From (3.8.7), the total potential energy can be expressed in terms of the mid-surface displacements (u_f, u_s, and w), the material stiffness, and the external loads.

3.9 Loads

There are two phases in which the loads are applied on the structure. The first phase involves the internal pressure. For most analyses in this thesis, an internal pressure of 500 kPa (72.5 psi) is applied. The second phase involves application of the external loads. Several different types are studied.

The first type of external load is a "full" snow load. This load is a symmetrical vertical load applied on top of the arch-shell for slopes between -30° and 30° with the horizontal in the longitudinal direction (global x direction). In this study, it is assumed that for slopes greater than 30° along the arch, the snow will fall off from the structure. Around the cross section, the loads are distributed vertically downward between the slopes -30° and 30° as well. The distribution of loads along the arch-shell and around the cross section is shown in Fig. 3.6.

The second type of external load is a "half" snow load. Essentially, this is the same as the full snow load with the exception that the loads are only applied on slopes

between 0° and 30° in the longitudinal direction as shown in Fig. 3.7. The application of load to the cross section is the same as for the full snow load. This loading models an asymmetric load on the structure.

The third type of external load is a “side” load. It is a uniform load *J* applied along the central half of the arc length between the bases. The loading on the cross section acts normally and, on the side portion of the cross section, acts between the slopes of 45° and -45° with the horizontal (global z direction).

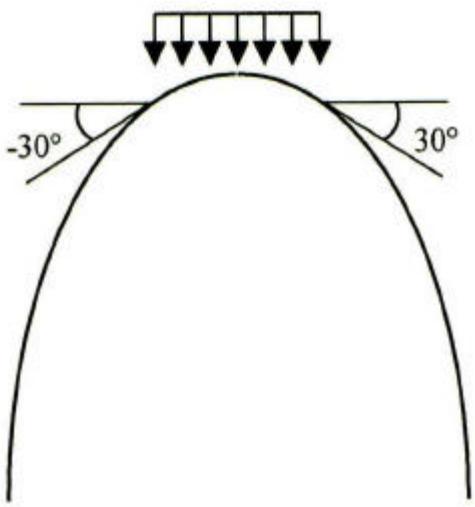

a) Meridian Profile

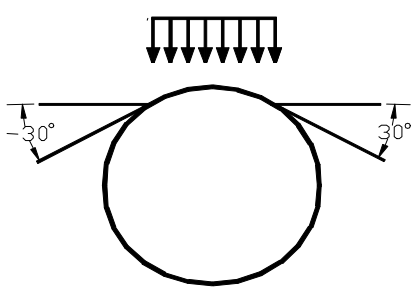

b) Cross Section Profile

Figure 3.6 Full snow load distribution

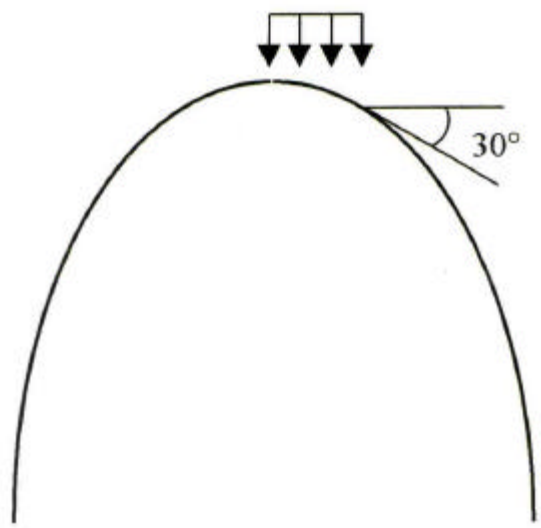

Figure 3.7 "Half " snow load distribution

The fourth type of external loading is a wind pressure Q. This pressure is a non-uniform pressure acting normal to the surface of the arch-shell. The pressure is applied around the cross section from -45° to 45° and all along the entire length of the arch-shell.

The self-weight of the structure is treated as one type of external load instead of being an initial load. The reason is to allow the use of (3.4.1) – (3.4.5) which simplifies the computation. If the self-weight were treated as an initial loading, additional terms would be required for (3.4.1) – (3.4.5) due to this loading. With these additional terms, the exact solutions for T_f, T_s, and T_{fs} would not be available. The self-weight of the structure is applied at all points of the structure.

All external loads on the surface of the arch-shell are decomposed into three traction forces, q_f, q_s, and q_n, acting in the f, s, and outward normal direction,

respectively. The projection of the load $\overline{F}$ onto the line parallel to vector $\overline{q}$ (traction forces) is:

$$\frac{\overline{F} \cdot \overline{q}}{|\overline{q}|} \tag{3.9.1}$$

It can be expressed in terms of two independent coordinates, f and g(defined in section 3.2.1), and unit vectors $\hat{i}, \hat{j}, \hat{k}$ parallel to the global x, y, and z-axes. The position vectors for the traction forces are as follows:

At $f = 0$

$$\overline{q}_n = q_n(\sin g\hat{i} + \cos g\hat{j}) \tag{3.9.2}$$

$$\overline{q}_s = q_s(\cos g\hat{i} - \sin g\hat{j}) \tag{3.9.3}$$

$$\overline{q}_f = q_f\hat{k} \tag{3.9.4}$$

At $f = \frac{p}{2}$

$$\overline{q}_n = q_n\hat{k} \tag{3.9.5}$$

$$\overline{q}_s = q_s(\cos g\hat{i} - \sin g\hat{j}) \tag{3.9.6}$$

$$\overline{q}_f = q_f(-\cos g\hat{j} - \sin g\hat{i}) \tag{3.9.7}$$

At $s = 0$

$$\overline{q}_n = q_n(\cos f\hat{j} + \sin f\hat{k}) \tag{3.9.8}$$

$$\overline{q}_s = q_s\hat{i} \tag{3.9.9}$$

$$\overline{q}_f = q_f(-\sin f\hat{j} + \cos f\hat{k}) \tag{3.9.10}$$

The projections of a downward vertical load $\overline{F} = -F\hat{j}$ are:

At $f = 0$:

$$n: \quad -F\,\hat{j}\cdot(\sin g\hat{i} + \cos g\hat{j}) = -F\cos g \tag{3.9.11}$$

$$s: \quad -F\,\hat{j}\cdot(\cos g\hat{i} - \sin g\hat{j}) = F\sin g \tag{3.9.12}$$

$$f: \quad -F\,\hat{j}\cdot\hat{k} = 0 \tag{3.9.13}$$

At $f = \frac{p}{2}$:

$$n: \quad -F\,\hat{j}\cdot\hat{k} = 0 \tag{3.9.14}$$

$$s: \quad -F\,\hat{j}\cdot(\cos g\hat{i} - \sin g\hat{j}) = F\sin g \tag{3.9.15}$$

$$f: \quad -F\,\hat{j}\cdot(-\cos g\hat{j} - \sin g\hat{i}) = F\cos g \tag{3.9.16}$$

At $s = 0$:

$$n: \quad -F\,\hat{j}\cdot(\cos f\hat{j} + \sin f\hat{k}) = -F\cos f \tag{3.9.17}$$

$$s: \quad -F\,\hat{j}\cdot\hat{i} = 0 \tag{3.9.18}$$

$$f: \quad -F\,\hat{j}\cdot(-\sin f\hat{j} + \cos f\hat{k}) = F\sin f \tag{3.9.19}$$

By combining all the cases, the general projections of $-F\,\hat{j}$ become:

$$\bar{q}_n: \quad -F\cos g\cos f \tag{3.9.20}$$

$$\bar{q}_s: \quad F\sin g \tag{3.9.21}$$

$$\bar{q}_f: \quad F\cos g\sin f \tag{3.9.22}$$

The snow load F_0 has units of force per unit horizontal area. Decomposing the snow load F_0 into the three traction forces q_f, q_s, and q_n, the units then become force per surface area and the following equations are obtained:

$$q_n = -F_0\cos^2 g\cos^2 f \tag{3.9.24}$$

$$q_s = F_0\sin g\cos g\cos f \tag{3.9.25}$$

$$q_f = F_0 \cos^2 g \sin f \cos f \tag{3.9.26}$$

where the loads are applied between the arc length of s = -16.67 to 16.67 for the full snow load and s = 0 to 16.67 for the half snow load (for a circular arch with s_0 = 50) with circumferential angle $f = -p/6$ to $p/6$ for both cases.

For the side load, the uniform load J is applied on the side between the limits of f = p/4 to 3p/4 and arc length s = -25 to 25. The following are the traction forces:

$$q_n = -J \tag{3.9.27}$$

$$q_s = 0 \tag{3.9.28}$$

$$q_f = 0 \tag{3.9.29}$$

The wind pressure distribution presented in this thesis is taken from Soare (1967). The wind pressure and suction are given by:

$$r_w = k\, g_w = \frac{1}{2} k r\, v^2 \tag{3.9.30}$$

where

g_w is the basic dynamic pressure

r is the density of air

v is the wind velocity

k is a shape factor written as a trigonometric expression in terms of q

$q = \dfrac{p(50+s)}{100}$, the angle from the horizontal to any point on the arc length (if s_0 = 50)

The rough wind pressure distribution is being used as the pressure distribution on the arch-shell:

$$k(q) = -0.258 + 0.488\cos q + 0.476\cos 2q + 0.328\cos 3q + 0.100\cos 4q \qquad (3.9.31)$$

For (3.9.31), positive values of k signify inward pressure, while negative values of k signify suction. A wind pressure of magnitude Q (with respect to internal pressure) is applied to the structure between the limits of $f = -p/4$ to $p/4$ and arc length $s = -s_0$ to s_0. The following are the traction forces:

$$q_n = -Qk(q)\cos f \qquad (3.9.32)$$

$$q_s = 0 \qquad (3.9.33)$$

$$q_f = 0 \qquad (3.9.34)$$

3.10 Computer Analysis

This thesis utilizes the commercial program Mathematica for the numerical integration of the potential energy (3.8.7). The material properties, strain-displacement equations, and energy functions are discussed in the following sections. A sample Mathematica program is included in Appendix A.

3.10.1 Material Properties

All material properties related to the potential energy (3.8.7) are non-dimensionalized with respect to combinations of internal pressure p and cross-sectional radius r. This allows the stiffness matrices in (3.8.7) to be computed without any units. The following are the non-dimensional parameters:

$$\hat{k} = rk \qquad \hat{s} = \frac{s}{r} \qquad \hat{h} = \frac{h}{r} \qquad \hat{E}_f = \frac{E_f}{p} \qquad \hat{E}_s = \frac{E_s}{p}$$

$$\hat{s}_0 = \frac{s_0}{r} \qquad \hat{A}_{ij} = \frac{A_{ij}}{pr} \qquad \hat{D}_{ij} = \frac{D_{ij}}{pr^3} \qquad c = \frac{C}{p} \qquad \hat{U} = \frac{U}{pr^3}$$

$$\hat{A}_f = \frac{A_f}{r} = 1 \qquad \hat{A}_s = 1 + \hat{k}\cos f \qquad \hat{R}_f = \frac{R_f}{r} = 1 \qquad \hat{R}_s = \frac{R_s}{r} = 1 + \frac{1}{\hat{k}\cos f}$$

$$\hat{G}_{fs} = \frac{G_{fs}}{p} \qquad \hat{N} = \frac{N}{pr} \qquad \hat{q} = \frac{q}{p} \qquad \hat{M} = \frac{M}{pr^2}$$

$$\hat{T}_f = \frac{2 + \hat{k}\cos f}{2 + 2\hat{k}\cos f} \qquad \hat{T}_s = \frac{1}{2} \qquad \hat{T}_{fs} = 0$$

$$\hat{u}_f = \frac{u_f}{r} \qquad \hat{u}_s = \frac{u_s}{r} \qquad \hat{w} = \frac{w}{r}$$

3.10.2 Strain-Displacement Relations

The Rayleigh-Ritz method is used, assuming the following displacement equations:

$$u_f = \sum_{n=1}^{N}\sum_{m=0}^{M}(v_m + v_{1mn}\cos nf + v_{2mn}\sin nf)\cos mpx \tag{3.10.1}$$

$$u_s = \sum_{n=1}^{N}\sum_{m=1}^{M}(u_m + u_{1mn}\cos nf + u_{2mn}\sin nf)\sin mpx \tag{3.10.2}$$

$$w = \sum_{n=1}^{N}\sum_{m=0}^{M}(w_m + w_{1mn}\cos nf + w_{2mn}\sin nf)\cos mpx \tag{3.10.3}$$

where (if $s_0 = 50$)

$$x = \frac{s + 50}{100}$$

The strain-displacement relations of Sanders (1959) can be fully expressed in terms of the displacement coefficients (v_m, v_{1mn}, etc.). In Chapters 4 and 5, the displacements u_f, u_s, and w (displacements in local x, y, and z directions) are expanded using a total of forty terms and expressed as follows:

$$u_f = \sum_{i=1}^{15} d_i p_i(f,s) \tag{3.10.4}$$

$$u_s = \sum_{i=16}^{25} d_i p_i(f,s) \tag{3.10.5}$$

$$w = \sum_{i=26}^{40} d_i p_i(f,s) \tag{3.10.6}$$

where

d_i represent the displacement coefficients (v_{mn}, v_{1mn}, etc.) for (3.10.1) - (3.10.3)

p_i represent the functions ($\cos n f, \sin n f$, etc.) in (3.10.1) – (3.10.3), listed in Appendix A

Substituting the above equations into the strain-displacement relations (3.3.1) - (3.3.6) of Sanders, the strain and curvature terms in the total potential energy (3.8.7) can be written as follows (where $\partial_f = \partial/\partial f$ and $\partial_s = \partial/\partial s$, and where $\hat{A}_f = 1$ and $\hat{R}_f = 1$ have been used):

$$e_f = \sum_{i=1}^{40} d_i r_i(f,s) \tag{3.10.7}$$

where

i = 1 to 15: $r_i = \partial_f p_i$

i = 16 to 25: $r_i = 0$

i = 26 to 40: $r_i = p_i$

$$e_s = \sum_{i=1}^{40} d_i t_i(f,s) \tag{3.10.8}$$

where

i = 1 to 15: $t_i = -\dfrac{\hat{k}\sin f}{\hat{A}_s} p_i$

i = 16 to 25: $$t_i = \frac{1}{\hat{A}_s} \partial_s p_i$$

i = 26 to 40: $$t_i = \frac{1}{\hat{R}_s} p_i$$

$$g_{fs} = \sum_{i=1}^{40} d_i F_i(f, s) \tag{3.10.9}$$

where

i = 1 to 15: $$F_i = \frac{1}{\hat{A}_s} \partial_s p_i$$

i = 16 to 25: $$F_i = \partial_f p_i + \frac{\hat{k} \sin f}{\hat{A}_s} p_i$$

i = 26 to 40: $$F_i = 0$$

$$k_f = \sum_{i=1}^{40} d_i G_i(f, s) \tag{3.10.10}$$

where

i = 1 to 15: $$G_i = \partial_f p_i$$

i = 16 to 25: $$G_i = 0$$

i = 26 to 40: $$G_i = -\partial_f(\partial_f p_i)$$

$$k_s = \sum_{i=1}^{40} d_i H_i(f, s) \tag{3.10.11}$$

where

i = 1 to 15: $$H_i = -\frac{\hat{k} \sin f}{\hat{A}_s} p_i$$

i = 16 to 25: $$H_i = \frac{1}{\hat{A}_s} \partial_s \left(\frac{p_i}{\hat{R}_s}\right)$$

i = 26 to 40: $$H_i = \frac{\hat{k} \sin f}{\hat{A}_s} \partial_f p_i - \frac{1}{\hat{A}_s} \partial_s \left(\frac{\partial_s p_i}{\hat{A}_s}\right)$$

$$k_{fs} = \sum_{i=1}^{40} d_i L_i(f,s) \tag{3.10.12}$$

where

i = 1 to 15: $$L_i = \frac{1}{2\hat{A}_s}[\frac{1}{2}(3 - \frac{1}{\hat{R}_s})\partial_s p_i]$$

i = 16 to 25: $$L_i = \frac{1}{2\hat{A}_s}[\hat{A}_s \partial_f(\frac{p_i}{\hat{R}_s}) + \frac{\hat{k}\sin f}{\hat{R}_s} p_i + \frac{1}{2}(\frac{1}{\hat{R}_s} - 1)\partial_f(\hat{A}_s p_i)]$$

i = 26 to 40: $$L_i = \frac{1}{2\hat{A}_s}[-\hat{A}_s \partial_f(\frac{\partial_s p_i}{\hat{A}_s}) - \partial_s(\partial_f p_i) - \frac{\hat{k}\sin f}{\hat{A}_s}\partial_s p_i]$$

Also,

i = 1 to 15: $$k_i = p_i \quad , \quad o_i = 0 \quad ,$$

i = 16 to 25: $$k_i = 0 \quad , \quad o_i = \frac{1}{\hat{R}_s} p_i \quad , \tag{3.10.13}$$

i = 26 to 40: $$k_i = -\partial_f p_i \quad , \quad o_i = -\frac{1}{\hat{A}_s}\partial_s p_i$$

3.10.3 Energy Functions

The total potential energy (3.8.7) is expressed in terms of displacements, material stiffness, and external loads. For equilibrium, the total potential energy is stationary with respect to kinematic variations in displacements u_f, u_s, and w. Applying (3.10.7) – (3.10.12) in (3.8.7), the total energy becomes (in non-dimensional terms):

$$
\begin{aligned}
\hat{U} = & \frac{1}{2}\sum_{i=1}^{40}\sum_{j=1}^{40}\int_{-\hat{s}_0}^{\hat{s}_0}\int_0^{2p}[\hat{A}_{11}r_i r_j + \hat{A}_{12}(r_i t_j + r_j t_i) + \hat{A}_{22}t_i t_j + \hat{A}_{66}F_i F_j]\hat{A}_s\, d\, f\, d\hat{s}\, d_i\, d_j \\
& + \frac{1}{2}\sum_{i=1}^{40}\sum_{j=1}^{40}\int_{-\hat{s}_0}^{\hat{s}_0}\int_0^{2p}[\hat{D}_{11}G_i G_j + \hat{D}_{12}(G_i H_j + G_j H_i) + \hat{D}_{22}H_i H_j + 4\hat{D}_{66}L_i L_j]\hat{A}_s\, d\, f\, d\hat{s}\, d_i\, d_j \\
& - \int_{-\hat{s}_0}^{\hat{s}_0}\int_0^{2p}(\hat{q}_f\sum_{i=1}^{15}d_i p_i + \hat{q}_s\sum_{i=16}^{25}d_i p_i + \hat{q}_n\sum_{i=26}^{40}d_i p_i)\hat{A}_s\, d\, f\, d\hat{s} \\
& + \frac{1}{2}\sum_{i=1}^{40}\sum_{j=1}^{40}\int_{-\hat{s}_0}^{\hat{s}_0}\int_0^{2p}[\hat{T}_f k_i k_j + \hat{T}_s o_i o_j]\hat{A}_s\, d\, f\, d\hat{s}\, d_i\, d_j \\
& + \frac{c}{2}\sum_{i=1}^{40}\sum_{j=1}^{40}\int_0^{2p}[p_i(-\hat{s}_0, f)\, p_j(-\hat{s}_0, f)]\, d\, f\, d_i\, d_j \\
& + \frac{c}{2}\sum_{i=1}^{40}\sum_{j=1}^{40}\int_0^{2p}[p_i(\hat{s}_0, f)\, p_j(\hat{s}_0, f)]\, d\, f\, d_i\, d_j
\end{aligned}
\tag{3.10.14}
$$

where

$\hat{A}_{ij}$ and $\hat{D}_{ij}$ are defined in Sections 3.5 and 3.10.1

r's, t's, F's, G's, H's, and L's are defined in Section 3.10.2

CHAPTER 4 CIRCULAR ARCH-SHELL

4.1 Introduction

This chapter considers a single pressurized arch tube of circular shape in a vertical plane. The single arch has been considered as a possible support structure for the LANMaS. Another arch-shell whose profile in the x-y plane is non-circular and the curvature is assumed to be a quadratic function of arc length will be discussed in Chapter 5. The purpose of this analysis is to gain an understanding of the behavior of pressurized arches of different shapes.

The arch studied in this chapter has the following properties:

Base span:	25 .465m (83.546 ft)
Height:	12.732 m (41.773 ft)
Shape:	Semi-circular
Cross sectional radius:	0.4 m (1.31 ft)
Shell thickness:	2.5 mm (0.098 in.)
Modulus of elasticity:	7 GPa (1015 ksi)
Poisson's ratio:	0.3
Boundary conditions:	Clamped in the vertical direction with horizontal rollers and radial line springs with high stiffness

Four types of loads are investigated first: full snow, half snow, wind, and uniform side loads as discussed in Section 3.9. In this Chapter, the self-weight of the structure also will be treated as one type of external load.

4.2 Full Snow Load

The full snow load is applied as described in section 3.9. The deflection of the apex will be monitored in the vertical plane (global x-y plane) and the cross section plane (global y-z plane).

A snow load F_0, which is non-dimensionalized with respect to internal pressure, is applied to the structure. Figure 4.1 shows the downward deflection of the top meridian (at $f = 0$) with the solid curve representing the original curve under no external load and the dotted curve corresponding to $F_0 = 1$. The deflection will increase when the load magnitude is increased. The non-dimensional arc length x is zero at the left support and 1 at the right support in figure 4.1. Figure 4.2 depicts the deformed cross section profile under the same load magnitude but at $s = 0$ with the undeformed profile represented by the solid curve. The following displacement equations showing only the dominant terms were obtained from (3.8.7) and utilized to plot figure 4.1 and figure 4.2:

$$u_f = \{1.552 \sin f - 1.555 \cos 2px \sin f\} F_0 \tag{4.3.1}$$

$$u_s = \{-0.9569 \sin 2px + 0.06219 \sin 2px \cos f\} F_0 \tag{4.3.2}$$

$$w = \{-1.553 \cos f + 1.553 \cos 2px \cos f\} F_0 \tag{4.3.3}$$

The following are the stresses and moment (only the dominant terms):

At $s = 0$,

$$N_f = 1.508 + \frac{1}{1 + \frac{100 \sec f}{p}} (-89.61 \cos f - 3.579 \cos 2f) + \frac{1}{1 + \frac{p \cos f}{100}} (17.34) - \frac{p \sin f}{100 + p \cos f} (298.8 \sin f + 6.022 \sin 2f) \tag{4.3.4}$$

At $f = 0$,

$$N_s = -4.498 - 0.8238 \cos 2px \tag{4.3.5}$$

$$M_s = -1.753 * 10^{-5} + 0.0001862 \cos 2px \qquad (4.3.6)$$

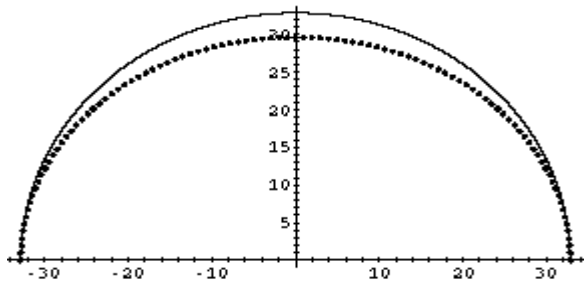

Figure 4.1 Deflection of the top meridian under full snow load at *f* = 0

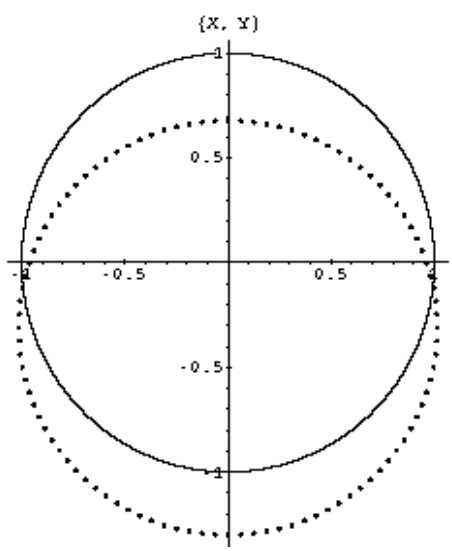

Figure 4.2 Deformation of the cross section under full snow load at *s* = 0

Figures 4.3 (a) – (f) show the plots of the three displacements versus the arc length *s* and angle *f*.

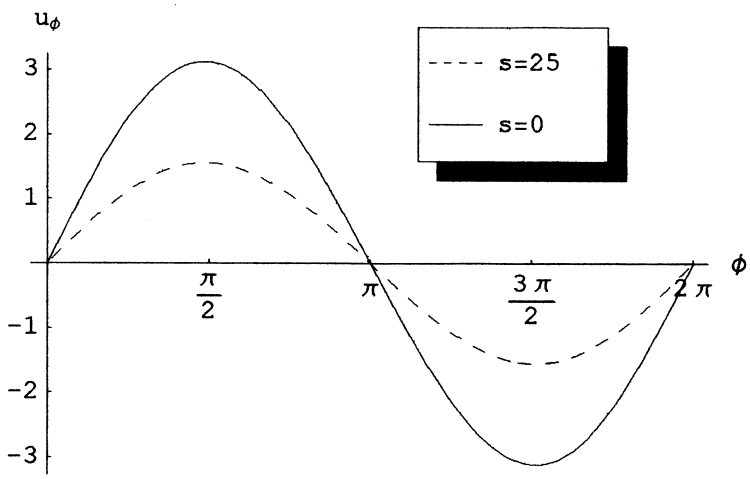

a) u_f versus f for full snow load

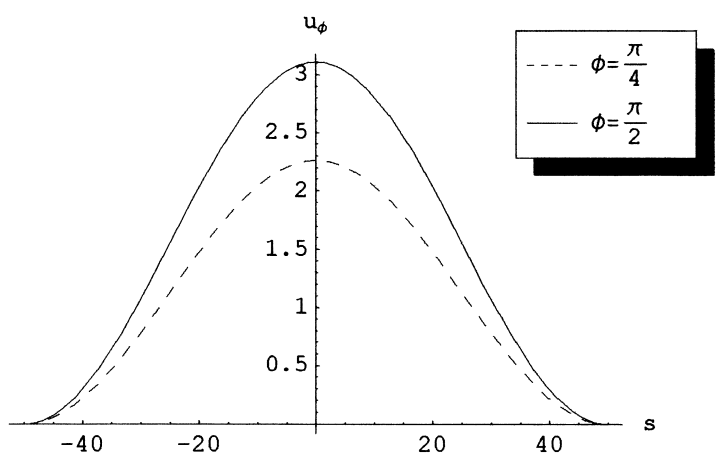

b) u_f versus s for full snow load

Figure 4.3

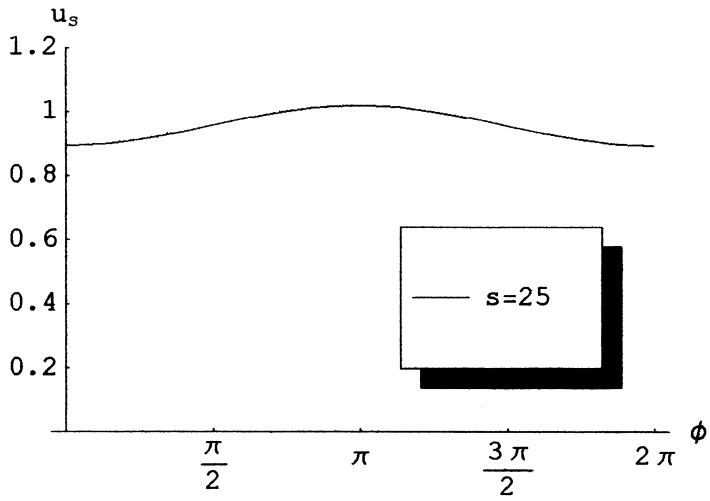

c) u_s versus f for full snow load

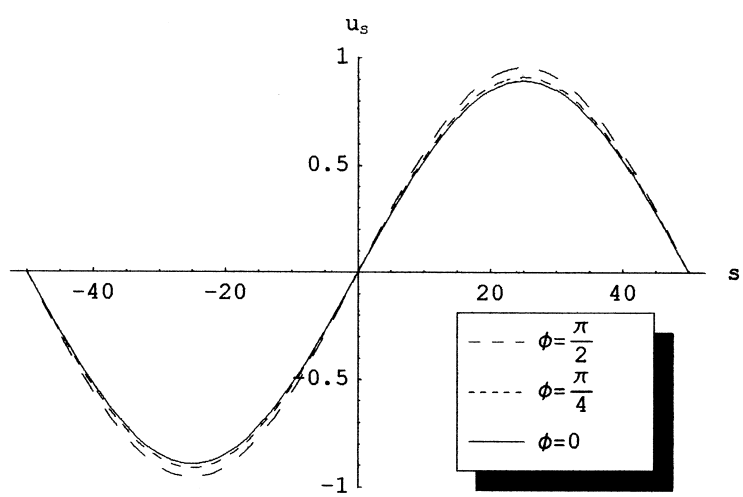

d) u_s versus s for full snow load

Figure 4.3

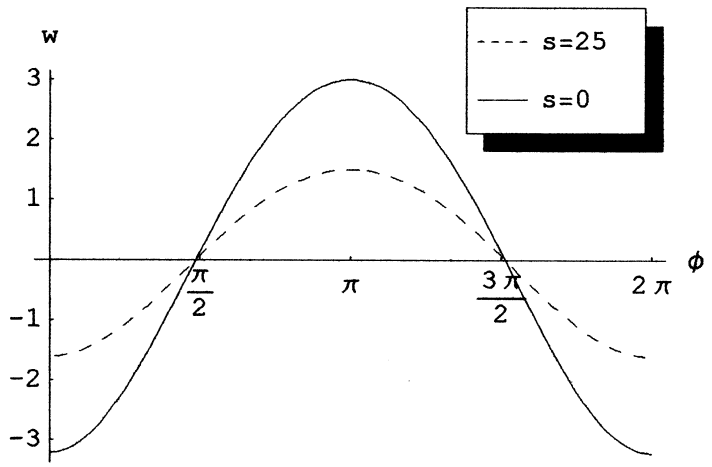

e) *w* versus *f* for full snow load

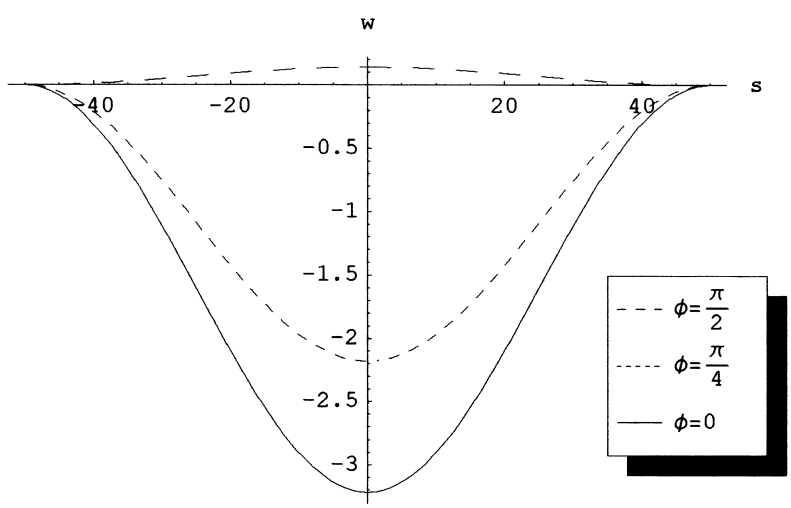

f) *w* versus *s* for full snow load

Figure 4.3 Displacements for full snow load

4.3 Half Snow Load

The half snow load is applied as described in section 3.9. The half snow load is only symmetric about the global y-z plane. The deflections in the x-y directions are monitored and plotted.

Figure 4.4 shows the downward deflection of the top meridian under a half snow load distribution F_0 = 1 with the solid curve representing the equilibrium configuration. Figure 4.5 depicts the deformed behavior of the cross section profile for F_0 = 1 at s = 0. The displacement results show that there is some non-symmetry in displacements u_s and w. Figure 4.6 shows the non-symmetry in displacement u_s plotted versus arc length s at f = 0. The asymmetrical terms for the displacement equations are very small compared to the symmetric terms. This indicates that the symmetric terms will dictate the behavior of the curve if the applied load magnitude is small compared to the internal pressure, particularly for displacement w. The following are the dominant terms for displacements, stresses, and moment:

$$u_f = \{0.5284 \sin f - 0.5294 \cos 2px \sin f\} F_0 \tag{4.4.1}$$

$$u_s = \{0.1321 \sin px - 0.2725 \sin 2px\} F_0 \tag{4.4.2}$$

$$w = \{-0.5288 \cos f + 0.5288 \cos 2px \cos f\} F_0 \tag{4.4.3}$$

At s = 0,

$$N_f = 0.5726 + \frac{1}{1 + \frac{100 \sec f}{p}} (-30.51 \cos f - 1.342 \cos 2f) - \frac{p \sin f}{100 + p \cos f} (101.7 \sin f + 2.258 \sin 2f) \tag{4.4.4}$$

At f = 0

$$N_s = -1.527 + 0.4023 \cos px \tag{4.4.5}$$

$$M_s = -6.567 * 10^{-6} + 6.968 * 10^{-6} \cos 2px \tag{4.4.6}$$

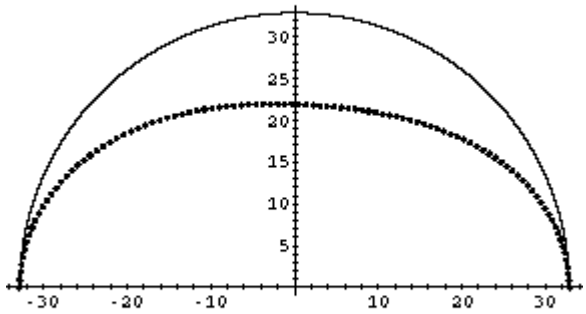

Figure 4.4 Deflection of the top meridian under half snow load at $f = 0$

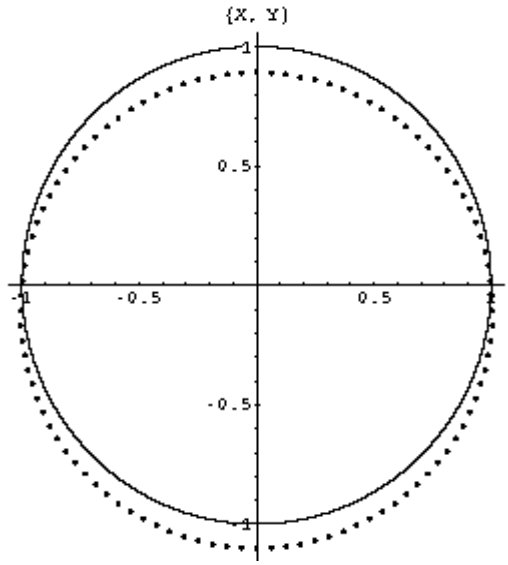

Figure 4.5 Deformation of the cross section under half snow load at $s = 0$

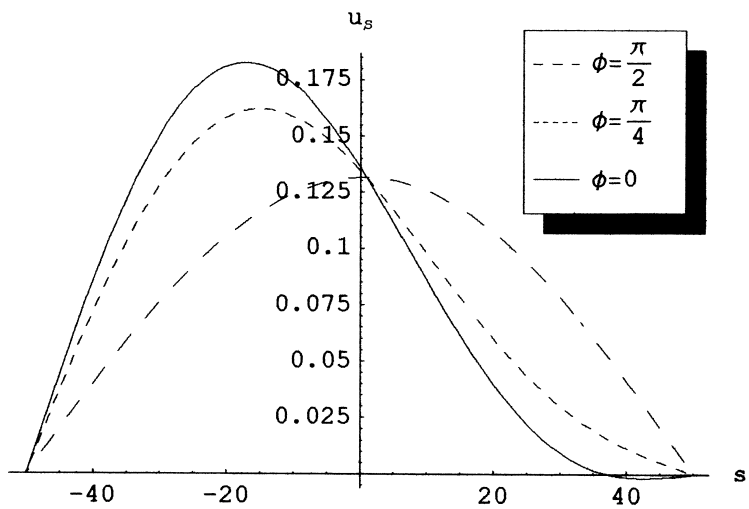

Figure 4.6 u_s versus s for half snow load at various f

4.4 Side Load

The uniform side load J is applied as described in section 3.9. Figure 4.7 shows how the deformation of the cross section of the arch-shell varies along the arch from arc length s = 0 at the center to s = 50 at the base of the arch-shell for J = 0.001. From the displacement results obtained, they indicate that there is little deformation at the ends due to the high spring stiffness that resists the radial displacement. The deformation is largest at the top of the arch at s = 0. Figure 4.8 depicts the deformation of the top meridian at f = 0 for J = 0.001 with the solid line representing the undeformed curve. The following are the dominant terms for displacement, stresses, and moment:

$$u_f = \{-214.9\cos f + 215.2\cos 2px\}J \tag{4.5.1}$$

$$u_s = \{13.38\sin 2px \sin f\}J \tag{4.5.2}$$

$$w = \{-214.9\sin f + 214.9\cos 2px \sin f\}J \tag{4.5.3}$$

At $s = 0$,

$$N_f = 21.80\sin f - 1.335\sin 2f + \frac{1}{1+\frac{100\sec f}{p}}(-12402\sin f)$$
$$+\frac{1}{1+\frac{p\cos f}{100}}(-24.26\sin f) - \frac{p\sin f}{100(1+\frac{p\cos f}{100})}(-12408\cos f) \tag{4.5.4}$$

At $f = 0$

$$N_s = 0.1473 - 0.1913\cos 2px \tag{4.5.5}$$

$$M_s = 2.116*10^{-5} - 2.125*10^{-5}\cos 2px \tag{4.5.6}$$

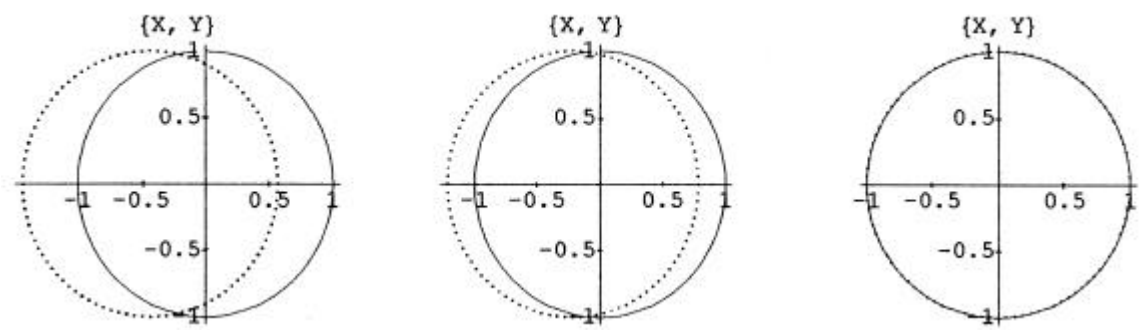

$s = 0$ $s = 25$ $s = 50$

Figure 4.7 Deformation of the cross section of the arch-shell

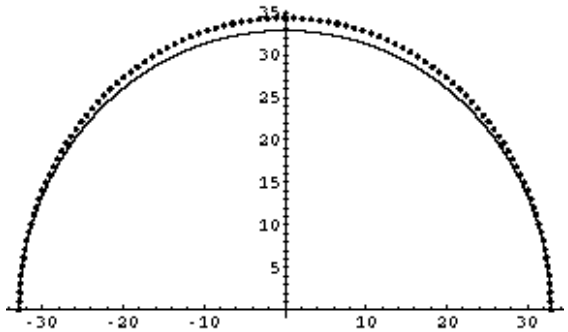

Figure 4.8 Deflection of the top meridian under side load at $f = 0$

Figures 4.9 (a) – (f) show the plots of the three displacements versus the arc length s and angle f for $J = 0.01$.

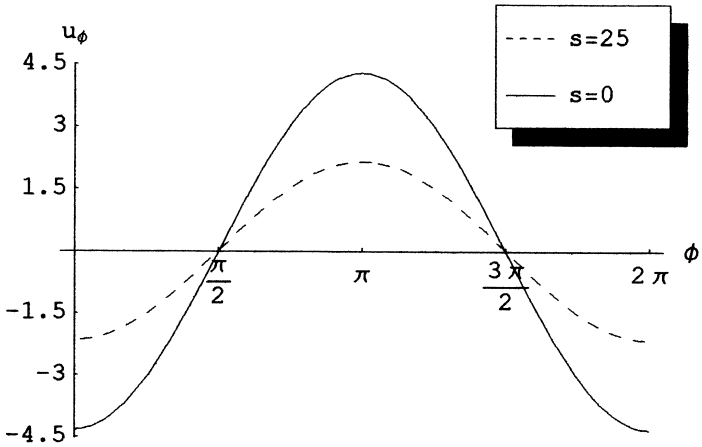

a) u_f versus f for uniform side load

Figure 4.9

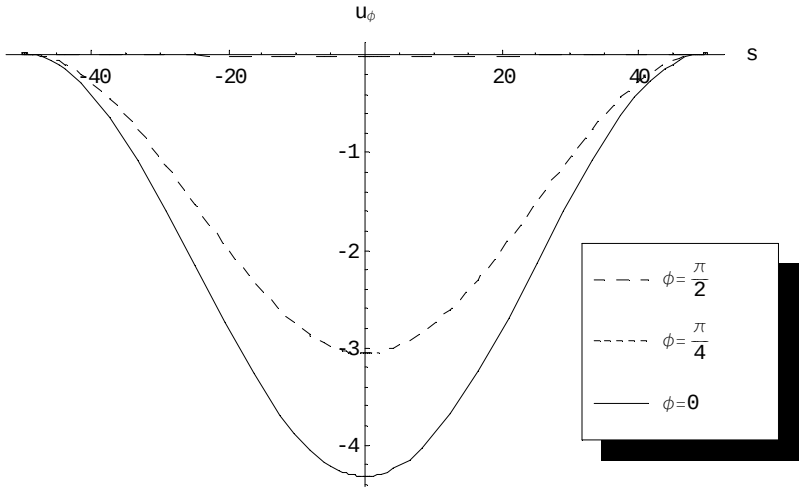

b) u_f versus s for uniform side load

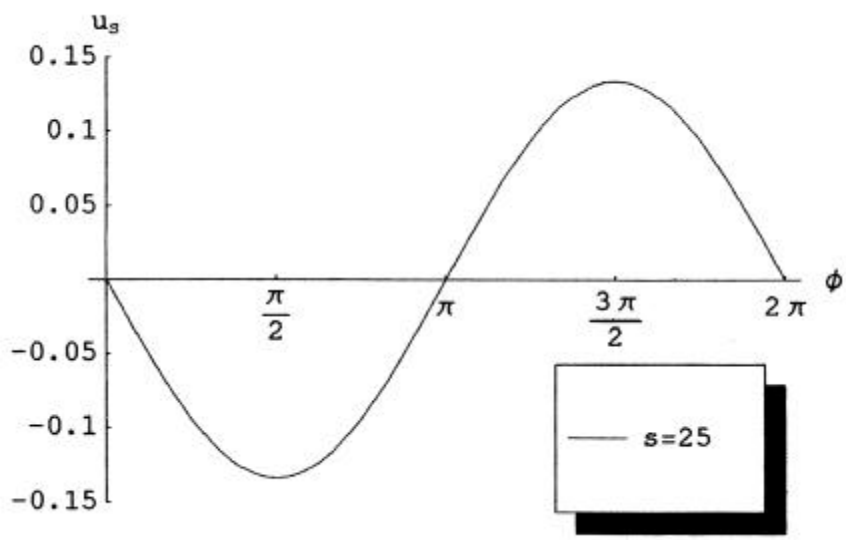

c) u_s versus f for uniform side load

Figure 4.9

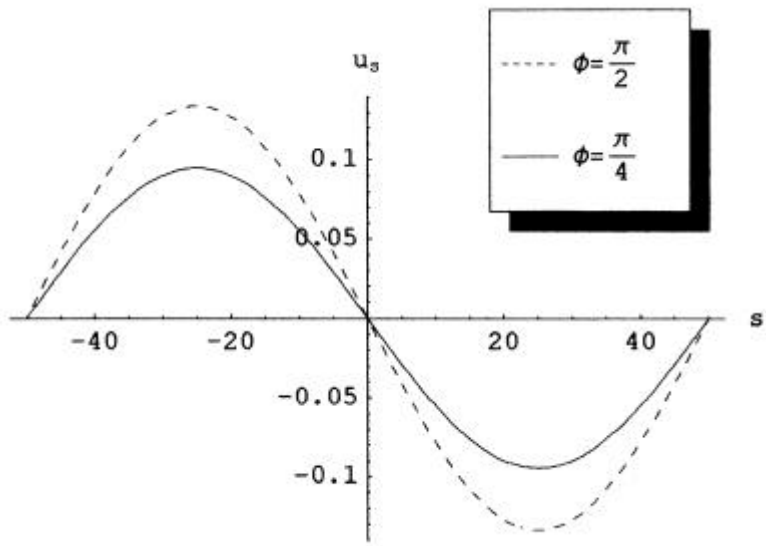

d) u_s versus s for uniform side load

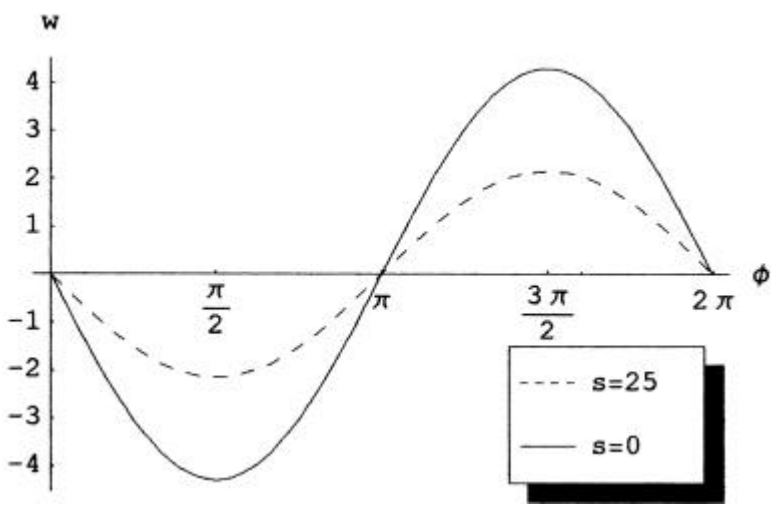

e) w versus f for uniform side load

Figure 4.9

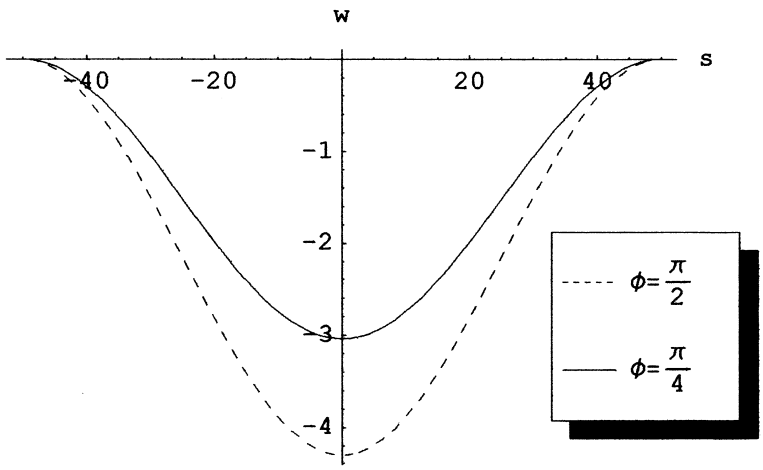

f) *w* versus *s* for uniform side load

Figure 4.9 Displacements for side load

4.5 Wind Load

The rough wind distribution as described in (3.9.31) is used as the pressure distribution on the circular arch-shell. The distribution is applied to the arch-shell as described in section 3.9.

Figures 4.10 and 4.11 show the deformed cross section and the top meridian (global x-y plane) profile under this type of loading for Q = 0.01. The following are the dominant terms for displacements, stresses, and moment:

$$u_f = \{-1.157 \sin f + 1.159 \cos 2px \sin f\}Q \tag{4.6.3}$$

$$u_f = \{0.5483 \sin 2px - 0.05486 \sin 2px \cos f\}Q \tag{4.6.4}$$

$$w = \{1.158 \cos f - 1.158 \cos 2px \cos f\}Q \tag{4.6.5}$$

At $s = 0$,

$$N_f = 0.01288 + \frac{1}{1+\frac{100\sec f}{p}}(2.227\cos f) + \frac{1}{1+\frac{p\cos f}{100}}(-0.03313)$$
$$+ \frac{1}{100(1+\frac{p\cos f}{100})}(0.6681\sin f) \tag{4.6.6}$$

At $f = 0$

$$N_s = 0.03327 - 0.003820\cos 2px \tag{4.6.7}$$

$$M_s = -1.247*10^{-7} + 3.127*10^{-6}\cos 2px \tag{4.6.8}$$

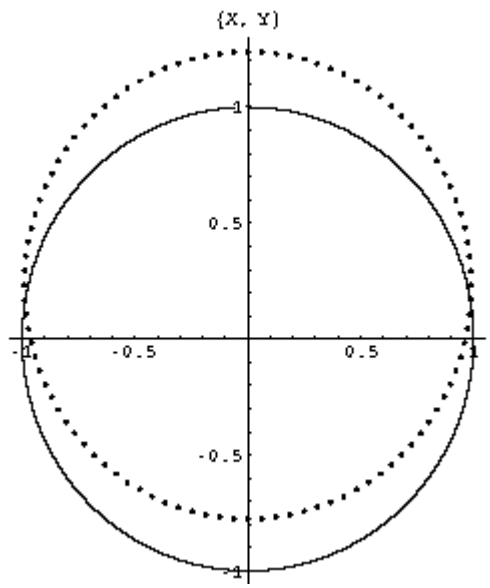

Figure 4.10 Deformation of the cross section under wind load at $s = 0$

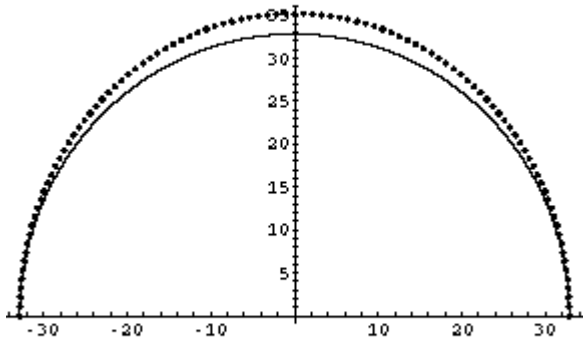

Figure 4.11 Deflection of the top meridian under wind load at $f = 0$

Figures 4.12 (a) – (f) show the plots of the three displacements versus the arc length *s* and angle *f*.

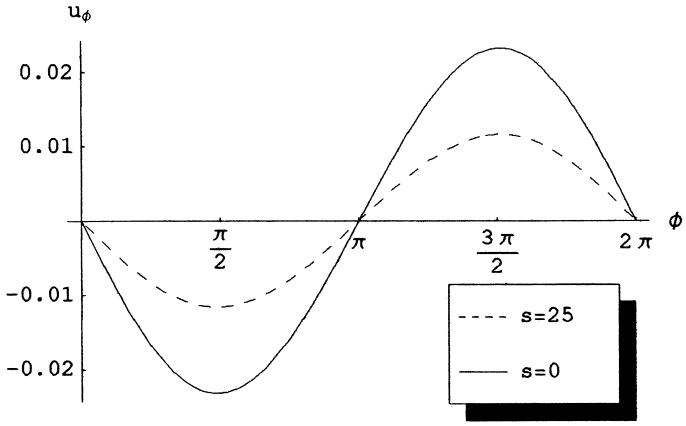

a) u_f versus f for wind load

Figure 4.12

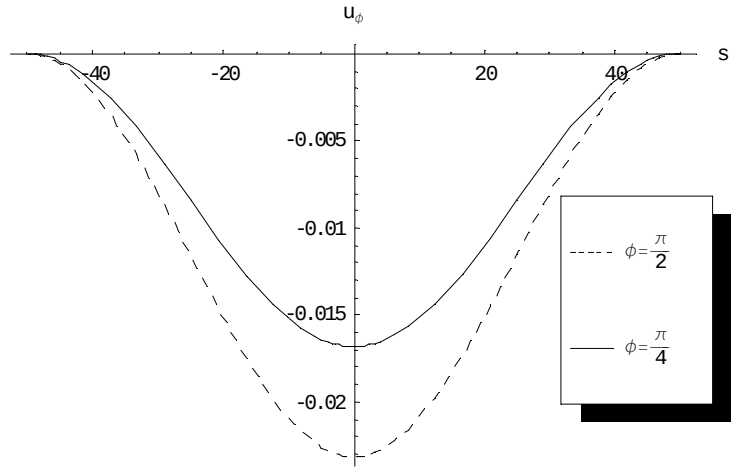

b) u_f versus s for wind load

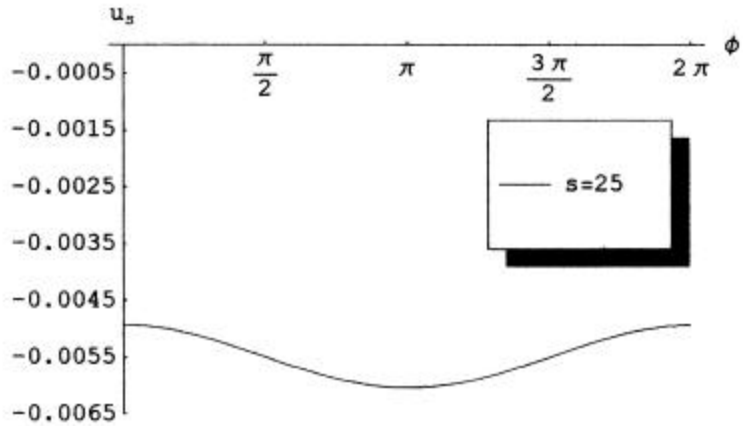

c) u_s versus f for wind load

Figure 4.12

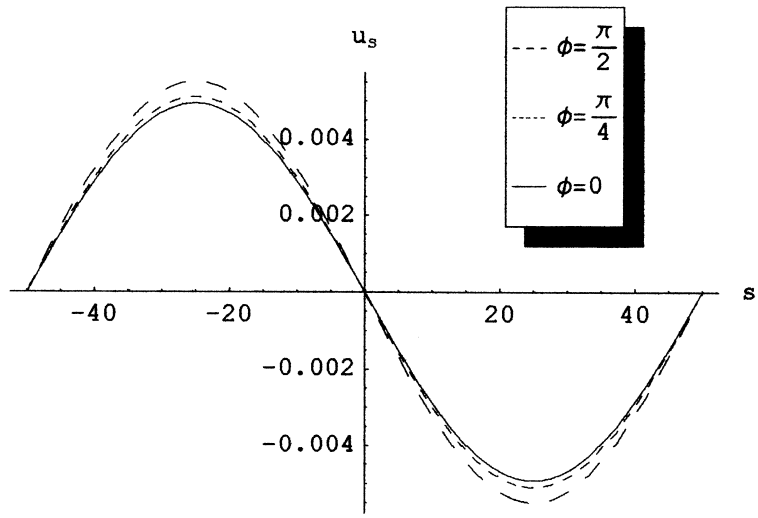

d) u_s versus s for wind load

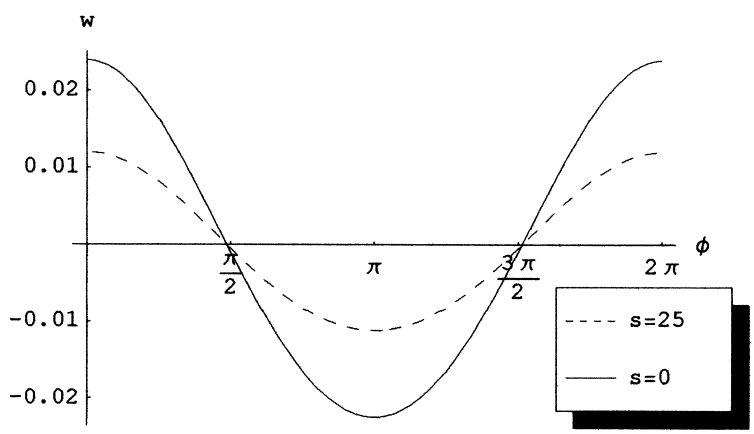

e) w versus f for wind load

Figure 4.12

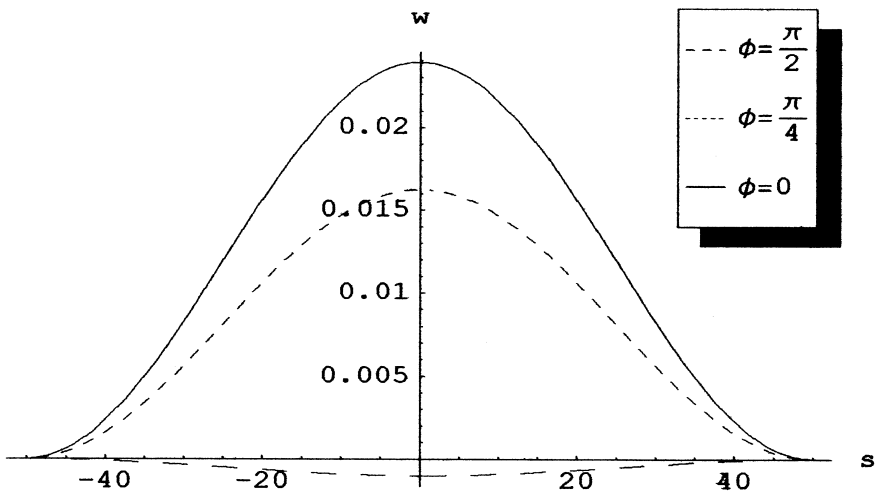

f) *w* versus *s* for wind load

Figure 4.12 Displacements for the wind load

4.6 Self-Weight

The self-weight of the arch-shell is treated as part of the external load and applied all along the structure, as mentioned in section 3.8. The self-weight of the structure is decomposed into three components: q_f, q_s, and q_n acting in the *f*, *s*, and normal directions, respectively. The following are the load formulas to represent the self-weight all along the structure:

$$q_n = -SW \cos g \cos f \tag{7.5}$$

$$q_s = SW \sin g \tag{7.6}$$

$$q_f = SW \cos g \sin f \tag{7.7}$$

where

SW represents the self-weight magnitude, which is relative to the internal pressure.

The magnitude of the self-weight is taken much less than the internal pressure *p*, as the material of the structure is lightweight and thin. The displacement resulting from the self-weight is first obtained and then could be superimposed onto the results obtained from the specific type of loading to find the actual behavior of the arch-shell under the different external loads. In this thesis, the self-weight contribution was not included in any of the displacement results obtained for the specific types of external loading. The reason is that the contribution from the self-weight of the structure is very small. The weight of the structure is more than 100 times smaller than the internal pressure applied on the structure and plays little significance in the behavior of the structure. The plots of the displacements versus the arc length *s* and angle f are similar to those for full snow load except for the magnitude. The following are the dominant terms for displacements:

$$u_f = \{11.66 \sin f - 11.68 \cos 2px \sin f\} SW \tag{7.8}$$

$$u_s = \{-7.775 \sin 2px + 0.4833 \sin 2px \cos f\} SW \tag{7.9}$$

$$w = \{-11.67 \cos f + 11.67 \cos 2px \cos f\} SW \tag{7.10}$$

CHAPTER 5 NON-CIRCULAR ARCH-SHELL

5.1 Introduction

This chapter considers a pressurized arch-shell whose profile is non-circular in the x-y plane and whose curvature is a quadratic function of arc length. The arch-shell has the same properties as the circular arch-shell discussed in section 4.1 except for its profile.

The behavior of the arch-shell is investigated under four types of loading conditions: full and half snow loads, wind load, and uniform side load. In this chapter, as before, all vertical deflections are measured from the pressurized equilibrium position with positive normal deflection being outward.

5.2 Quadratic Curvature

The non-dimensional curvature in this chapter is assumed to be:

$$\hat{k}(s) = a - b\, s^2 \tag{5.2.1}$$

where

$$a = \frac{p}{100}$$

$$b = \frac{p}{500{,}000}$$

s is the non-dimensionalized arc length

From (5.2.1), g the angle between the global y axis and the normal to the locus in the x-y plane, becomes:

$$g = \int_0^s \hat{k}(s)ds = \int_0^s (a - b\,s^2)ds = a\,s - \tfrac{1}{3}\,b\,s^3 \qquad (5.2.2)$$

The vertical distance h and the horizontal distance x from the apex for positive s are defined as the following, respectively:

$$h = \int_0^s \sin\,g ds = \int_0^s \sin(a\,s - \tfrac{1}{3}\,b\,s^3)ds \qquad (0 < s < 50) \qquad (5.2.3)$$

$$x = \int_0^s \cos\,g ds = \int_0^s \cos(a\,s - \tfrac{1}{3}\,b\,s^3)ds \qquad (0 < s < 50) \qquad (5.2.4)$$

Figure 5.1 shows the centerline profile and the positive direction of each axis. At s = 50, the values of h and x are h = 30.63 and x = 34.78, whereas for the circular arch-shell in Chapter 4 they are $h = x = 100/\pi = 31.83$. Therefore, this non-circular profile is shorter and wider than the circular profile.

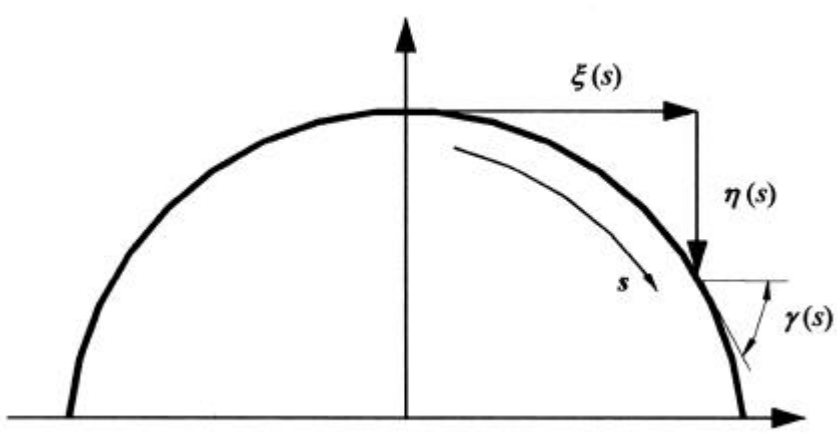

Figure 5.1 Geometry of non-circular arch-shell

5.3 Full Snow Load

The full snow load is applied to the arch-shell as described in section 3.9. The vertical deflection of the top meridian and the cross section of the arch-shell are monitored.

A snow load F_0, with magnitude relative to internal pressure, is applied on the structure. Figure 5.2 shows the vertical deflection of the top meridian (at $f = 0$) with $F_0 = 1$, and the largest deflection occurs at the center of the arch-shell. Figure 5.3 depicts the deformed cross section profile under the same load magnitude but at $s = 0$. The following are the dominant terms for the displacements, stresses, and moment:

$$u_f = \{2.368 \sin f - 2.370 \cos 2px \sin f\} \tag{5.3.1}$$

$$u_s = \{0.1462 \sin 2px \cos f\} \tag{5.3.2}$$

$$w = \{-2.369 \cos f + 2.369 \cos 2px \cos f\} \tag{5.3.3}$$

At $s = 0$

$$N_f = 4.016 + \frac{1}{1 + \frac{100 \sec f}{p}}(-136.7 \cos f) - \frac{p \sin f}{100 + p \cos f}(136.7 \sin f) \tag{5.3.4}$$

At $f = 0$

$$N_s = 0.5461 - 0.6185 \cos 2px + \frac{1}{1 + \frac{500000}{5000p - p\,s^2}}(-225.8 + 225.8 \cos 2px) \tag{5.3.5}$$

$$\begin{aligned} M_s = & \frac{1}{(5000p - ps^2)(1 + \frac{500000}{5000p - p\,s^2})^2}(146.4 \sin 2px) \\ & + \frac{1}{1 - \frac{p(-5000 + s^2)}{500000}}(2.902 * 10^{-6} \cos 2px) \end{aligned} \tag{5.3.6}$$

From the results obtained under the same load magnitude $F_0 = 1$, the non-circular arch-shell has larger deflections for all displacements (u_f, u_s, and w) compared to the circular arch-shell. The plot u_s versus s for the non-circular shape for $F_0 = 1$ is opposite of

that for the circular shape as shown in Figure 5.4 (d). Figures 5.4 (a) – (f) show the plots of the three displacements versus the arc length *s* and the angle *f*, for F_0 =1.

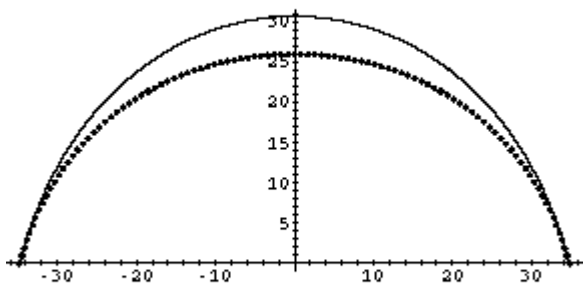

Figure 5.2 Deflection of the top meridian under full snow load at *f* = 0

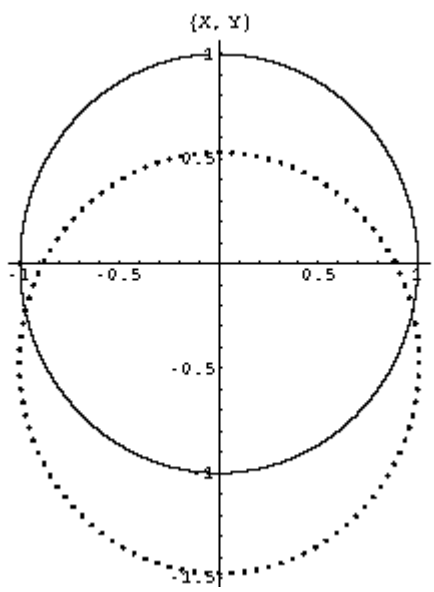

Figure 5.3 Deformation of the cross section under full snow load at *s* = 0

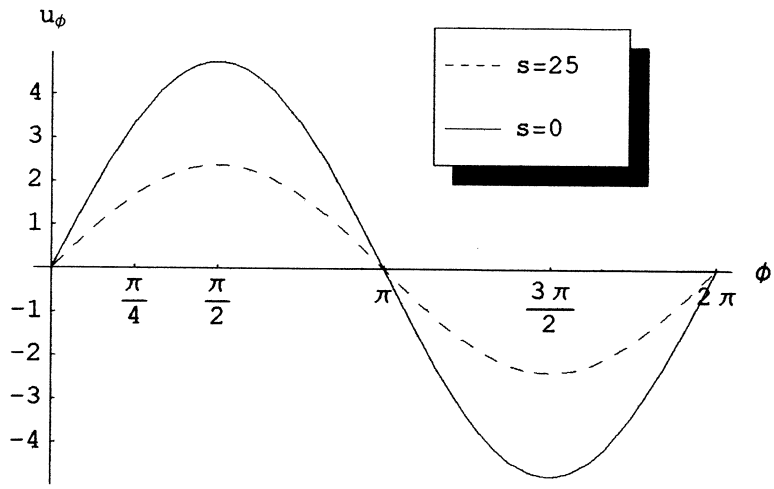

a) u_f versus f for full snow load

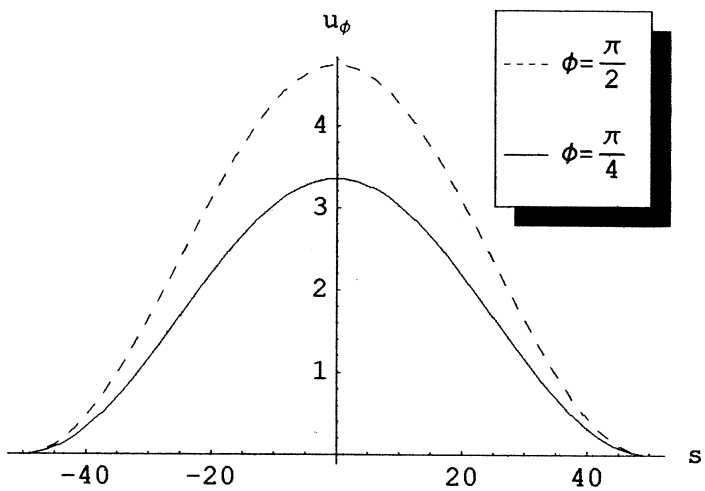

b) u_f versus s for full snow load

Figure 5.4

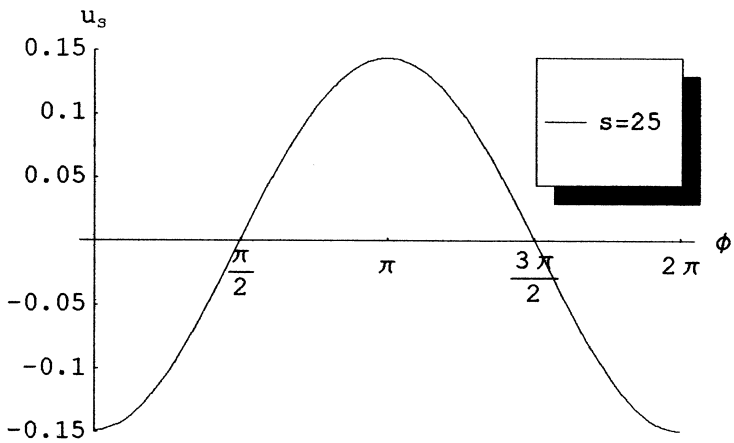

c) u_s versus f for full snow load

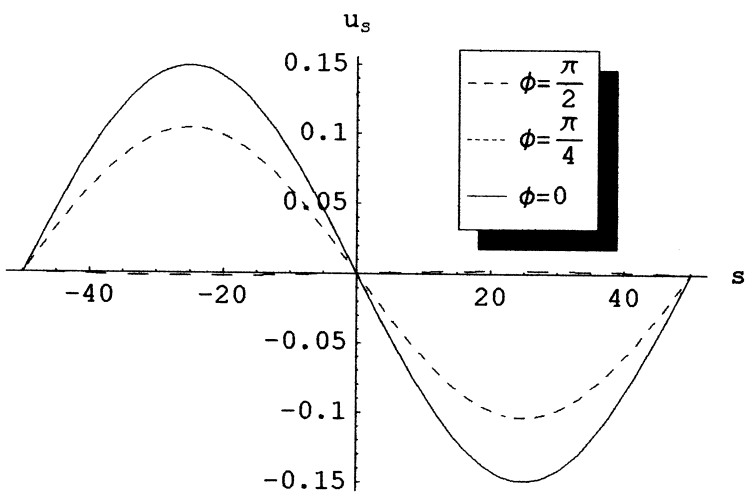

d) u_s versus s for full snow load

Figure 5.4

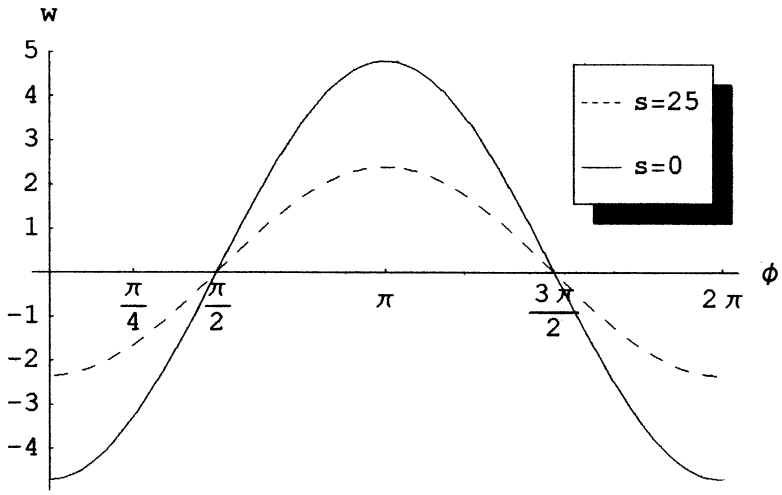

e) *w* versus *f* for full snow load

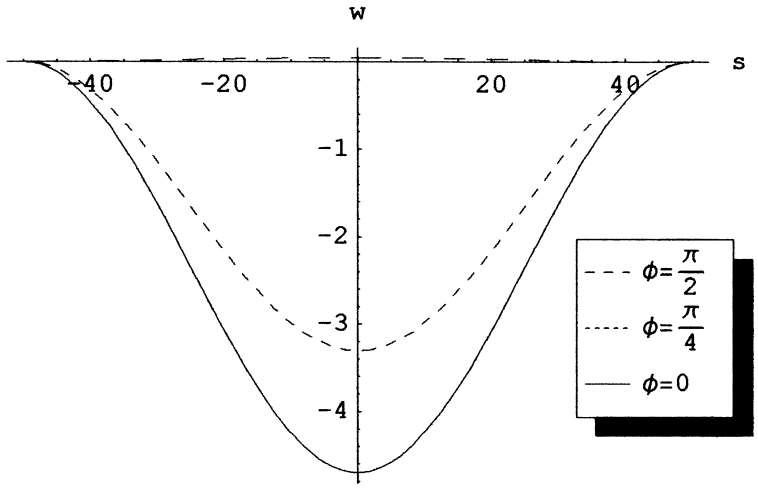

f) *w* versus *s* for full snow load

Figure 5.4 Displacements for full snow load

5.4 Half Snow Load

The half snow load is applied to the non-circular arch-shell as described in section 3.9. Both vertical and longitudinal deflections are monitored as the load is only symmetric about the y-z plane.

Figure 5.5 shows the downward deflection of the top meridian (at f = 0) with the half snow load distribution of F_0 =1. Figure 5.6 depicts the deformed shape of the cross section profile s = 0 under the same load magnitude. The displacement results indicate that there is some non-symmetry in the displacement u_s with the largest occurring at the top of the arch-shell. Figure 5.7 depicts the non-symmetric displacement u_s plotted versus the arc length s at various f under F_0 =1. The following are the dominant terms for displacements, stresses, and moment for F_0 =1:

$$u_f = 1.182 \sin f - 1.183 \cos 2px \sin f \tag{5.4.1}$$

$$u_s = 0.1315 \sin 2x + 0.07299 \sin 2px \cos f \tag{5.4.2}$$

$$w = -1.183 \cos f + 1.183 \cos 2px \cos f \tag{5.4.3}$$

At s = 0

$$N_f = 2.005 + \frac{1}{1+\frac{100 \sec f}{p}}(-227.5 \cos f) - \frac{p \sin f}{100 + p \cos f}(68.22 \sin f) \tag{5.4.4}$$

At f = 0

$$N_s = -0.3088 \cos 2px + \frac{1}{1+\frac{500000}{5000p - p\,s^2}}(-112.7 + 112.7 \cos 2px) \tag{5.4.5}$$

$$\begin{aligned} M_s = & \frac{1}{(5000p - ps^2)(1+\frac{500000}{5000p - p\,s^2})^2}(133.9 \sin 2px) \\ & + \frac{1}{1-\frac{p(-5000+s^2)}{500000}}(1.449 * 10^{-6} \cos 2px) \end{aligned} \tag{5.4.6}$$

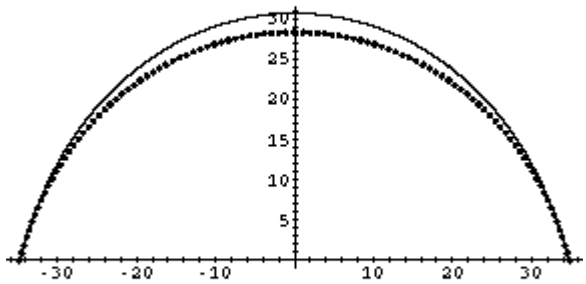

Figure 5.5 Deflection of the top meridian under half snow load at $f = 0$

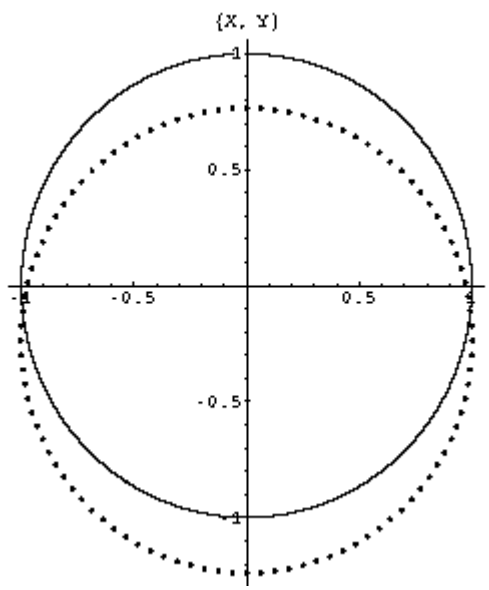

Figure 5.6 Deformation of the cross section under half snow load at $s = 0$

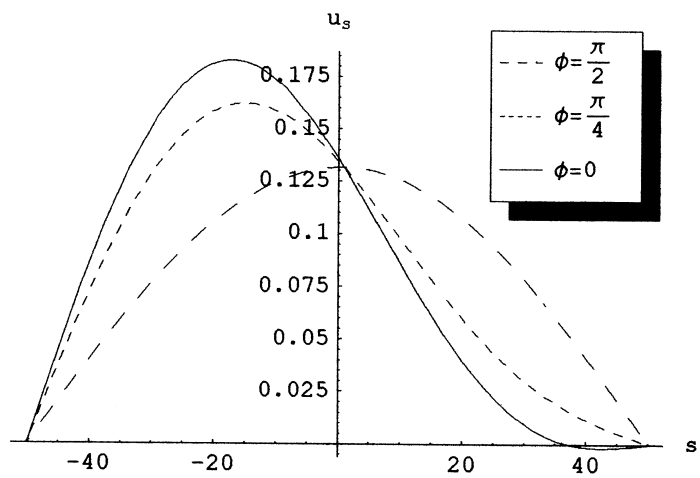

Figure 5.7 u_s versus s for half snow load at various f

5.5 Side Load

The uniform side load is applied on the non-circular arch-shell as described in section 3.9. The vertical deflection of the apex and the cross section shape are monitored.

Figure 5.8 shows the deformation of the cross section of the arch-shell at s = 0 under a uniform side load of J = 0.01. The deflection is largest at the top of the arch at s = 0. From the displacement results obtained, there is little deformation at the ends due to the boundary conditions as described in section 3.7. Figure 5.9 depicts the deflection of the top meridian at f = 0 and J = 0.01. Figures 5.10 (a) –(f) show the plots of the three displacements versus the arc length s and angle f. The following are the dominant terms for displacements, stresses, and moment:

$$u_f = -10.90\cos f + 10.90\cos 2px\cos f \tag{5.5.1}$$

$$u_s = 0.6771\sin 2px\sin f + 0.01299\sin 2px\sin 2f \tag{5.5.2}$$

$$w = -10.89\sin f + 10.89\cos 2px\sin f \tag{5.5.3}$$

At $s = 0$

$$N_f = 0.7136 + \frac{1}{1+\frac{100\sec f}{p}}(-628.3\sin f) - \frac{p\sin f}{100 + p\cos f}(-628.6\cos f) \qquad (5.5.4)$$

At $f = 0$

$$N_s = \frac{1}{1+\frac{500000}{5000p - p\,s^2}}(2.372 - 2.372\cos 2px) \qquad (5.5.5)$$

$$M_s = (6.212 * 10^{-9} + 1.151 * 10^{-9}\cos px) \qquad (5.5.6)$$

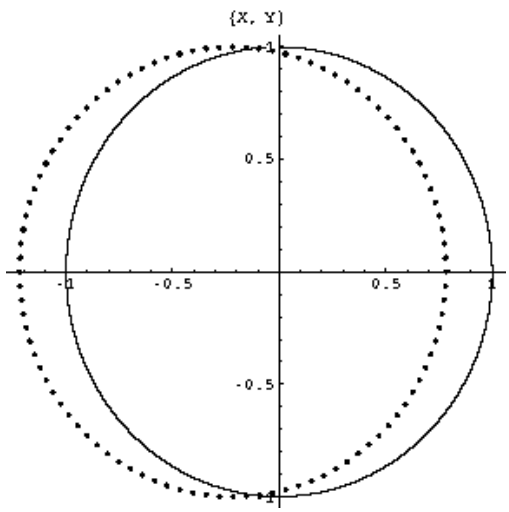

Figure 5.8 Deformation of the cross section under side load at $s = 0$

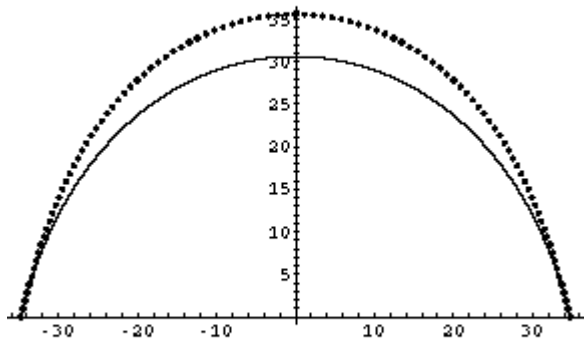

Figure 5.9 Deflection of the top meridian under side load at $f = 0$

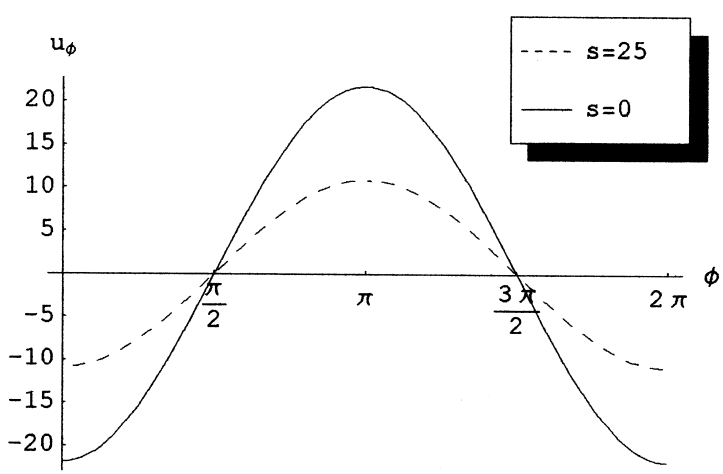

a) u_f versus f for uniform side load

Figure 5.10

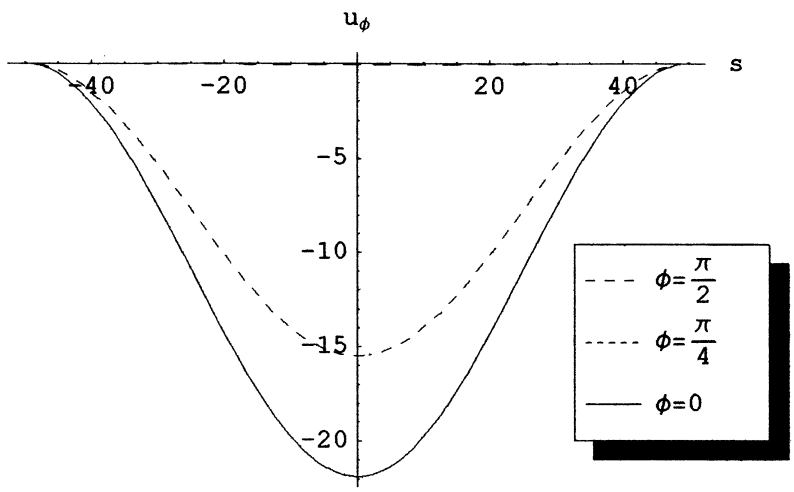

b) u_f versus s for uniform side load

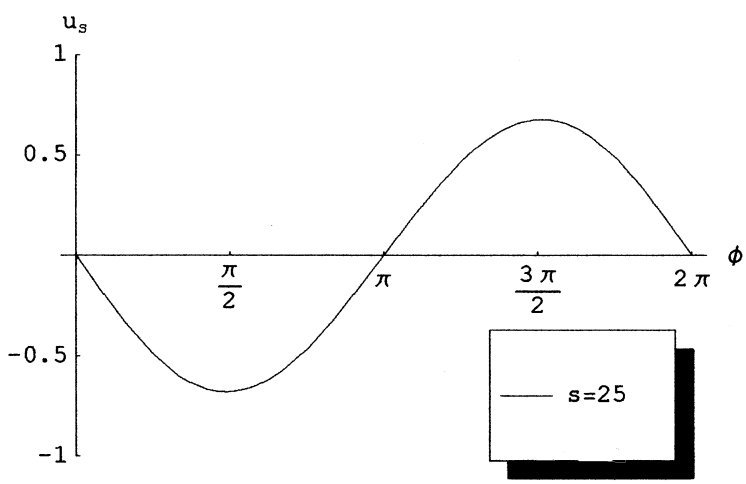

c) u_s versus f for uniform side load

Figure 5.10

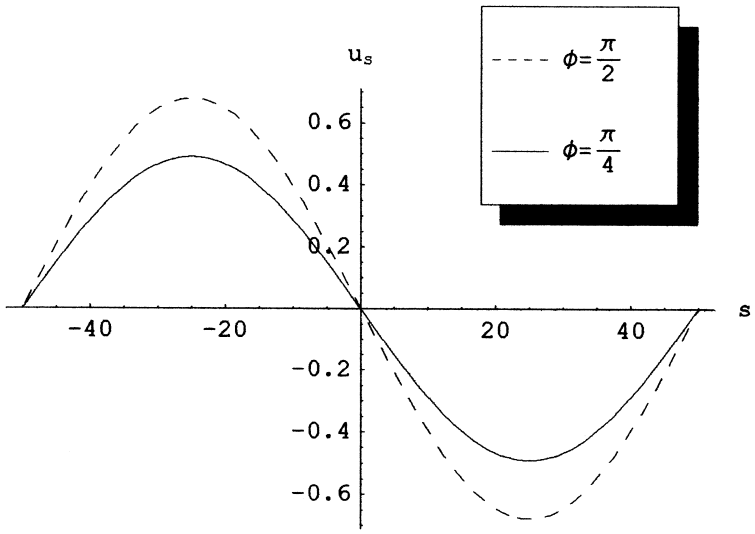

d) u_s versus s for uniform side load

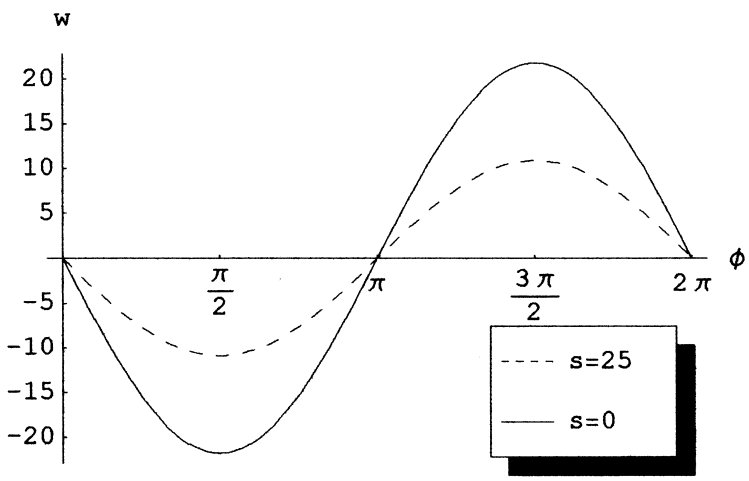

e) w versus f for uniform side load

Figure 5.10

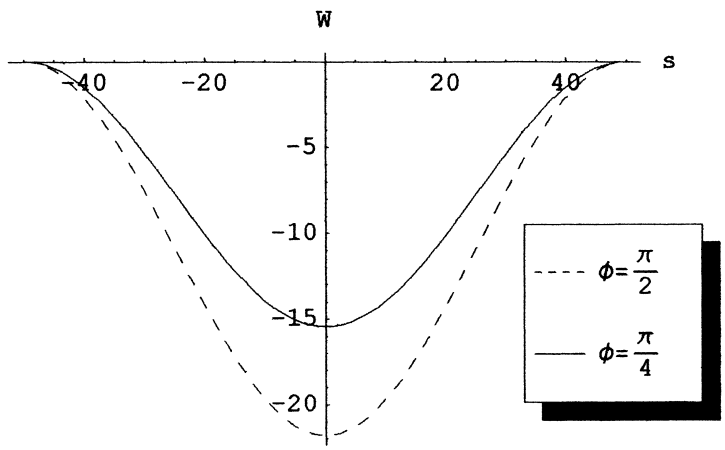

f) *w* versus *s* for uniform side load

Figure 5.10 Displacements for side load

5.6 Wind Load

The rough wind distribution described in (3.9.31) is used as the pressure distribution on the non-circular arch-shell. The distribution is applied to the arch-shell as described in section 3.9.

Figure 5.11 shows the deformed cross section and meridian profile under a wind pressure of Q = 0.01. The plot u_s versus s for the non-circular shape for Q = 0.01 as shown in Figure 5.12 (d) is opposite to that of the circular shape. Figures 5.12 (a) –(f) show the plots of the three displacements versus the arc length s and angle f. The following are the dominant terms for displacements, stresses, and moment under a wind pressure of Q = 0.01:

$$u_f = 0.02696 \sin f + 0.02699 \cos 2px \sin f \tag{5.6.1}$$

$$u_s = 0.001675 \cos f \sin 2px - 0.00002738 \sin 2px \cos 2f \tag{5.6.2}$$

$$w = 0.02698\cos f - 0.02698\cos 2px\cos f \tag{5.6.3}$$

At $s = 0$

$$N_f = -0.04554 + \frac{1}{1+\frac{100\sec f}{p}}(1.557\cos f) - \frac{p\sin f}{100 + p\cos f}(1.556\sin f) \tag{5.6.4}$$

At $f = 0$

$$N_s = \frac{1}{1+\frac{500000}{5000p - p\,s^2}}(2.571 - 2.571\cos 2px) \tag{5.6.5}$$

$$M_s = (1.004*10^{-9} + 1.599*10^{-9}\cos px) \tag{5.6.6}$$

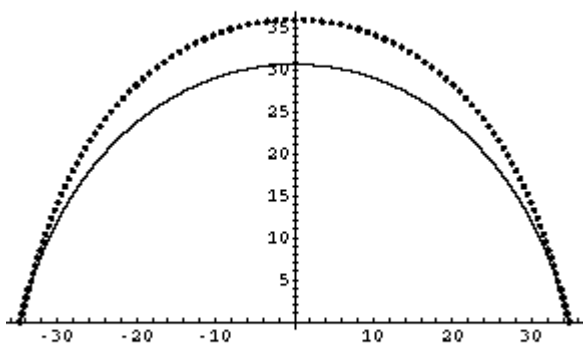

a) Deflection of the top meridian under wind load at $f = 0$

Figure 5.11

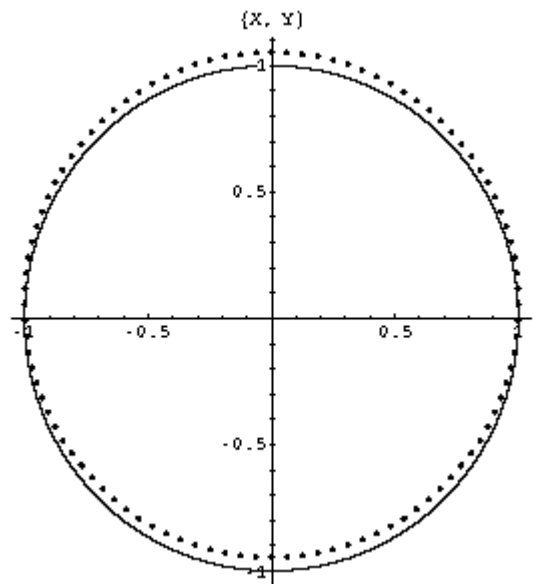

b) Deformation of the cross section under wind load at $s = 0$

Figure 5.11 Deformed meridian and cross section profiles

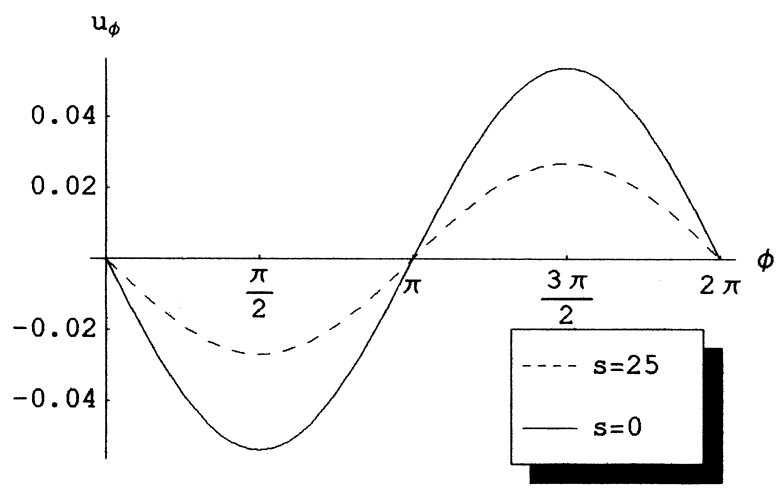

a) u_f versus f for wind load

Figure 5.12

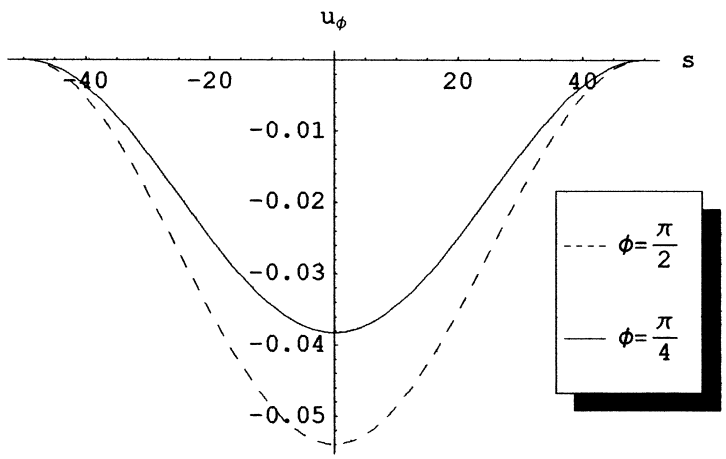

b) u_f versus s for wind load

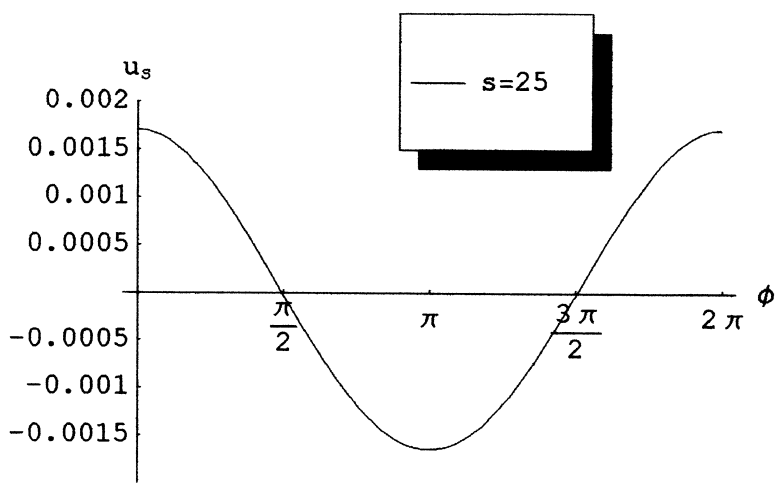

c) u_s versus f for wind load

Figure 5.12

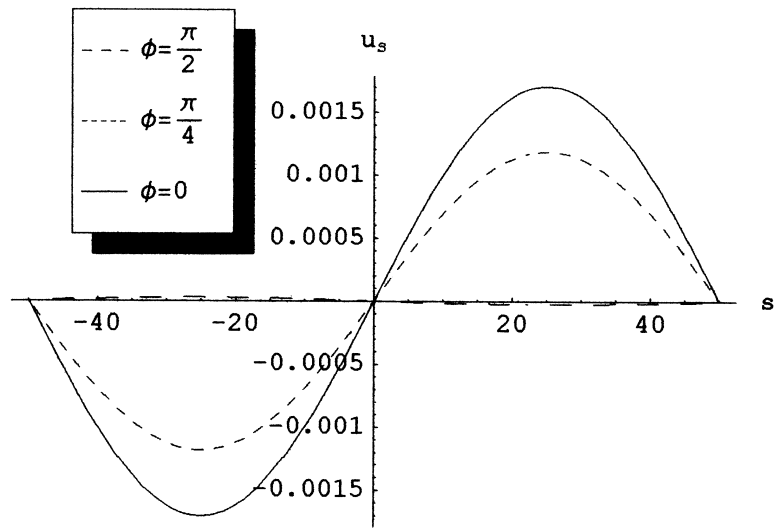

d) u_s versus s for wind load

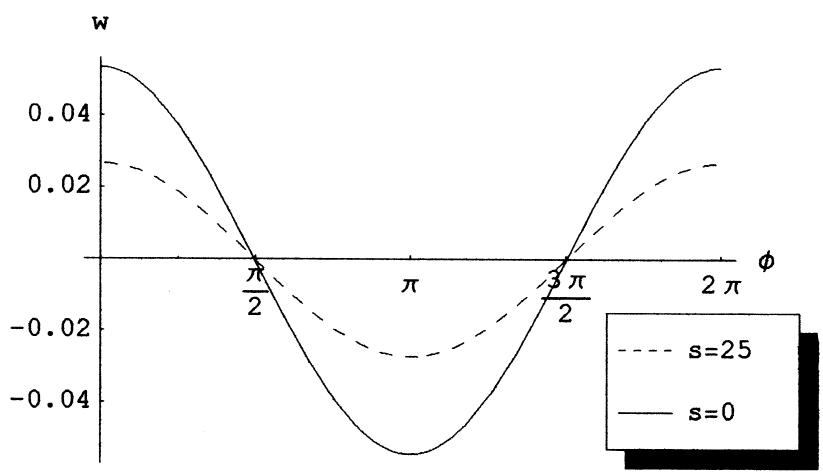

e) w versus f for wind load

Figure 5.12

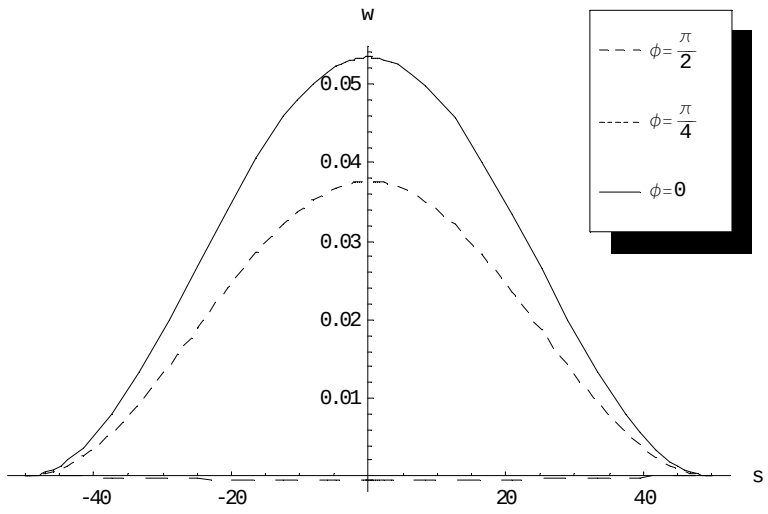

f) *w* versus *s* for wind load

Figure 5.12 Displacements for wind load

CHAPTER 6 FORMULATION USING SYMMETRY

6.1 Introduction

In Chapters 4 and 5, the Rayleigh-Ritz method is used by assuming the displacement equations (3.10.1) – (3.10.3) and incorporating them into the strain-displacement relations of Sanders. The strains and curvatures allow the total potential energy to be fully expressed in terms of displacements, the material properties, and the loads. The displacement equations in (3.10.1) – (3.10.3) are for a general loading. They include forty terms. Within these forty terms, both symmetric and non-symmetric functions are contained to model the behavior of the arch-shells under various types of loading as discussed in section 3.9.

However, from further analysis of the full snow loading which is symmetric in both coordinates f and s, the general displacement equations used in Chapters 4 and 5 are not sufficient to model the behavior of arch-shells under this type of loading. The reason is that the general equations used in (3.8.7) do not have enough symmetric terms to model the deformation of the arch-shell accurately. In order to obtain a better result, additional symmetric terms in f and s for the displacement equations are required. In this chapter, newly formulated displacement functions p_i in (3.10.4) – (3.10.6) are used for a circular arch-shell under various types of loading. The non-symmetric terms, which give zero values for the displacements, are replaced with additional displacement functions.

There are four types of loads being investigated in the following sections. All cases have the same material properties and dimensions unless specified otherwise. In all cases, a circular arch-shell with circular cross section of radius 0.15m is considered. An internal pressure of 400kPa is applied on the structure.

6.2 Full Snow Load

There are two cases of full snow load being investigated, using 26 and 33 displacement functions. The new functions eliminate the need for the springs at the support and for (3.8.5). These new functions model the supports as clamped bases and will give radial displacement $w = 0$ at the bases.

6.2.1 Formulation using 26 Displacement Functions

The full snow load with magnitude F_0 is applied on the circular arch-shell as described in section 3.9. The displacement functions are expanded to twenty-six terms by adding more symmetric functions in f and s. Below are the displacement equations:

$$u_f = \sum_{i=1}^{8} d_i p_i \quad , \quad u_s = \sum_{i=9}^{17} d_i p_i \quad , \quad w = \sum_{i=18}^{26} d_i p_i \tag{6.1}$$

where

d_i is defined in section 3.10.2

$$\begin{aligned}
&p_1 = \sin f && p_2 = \sin f \cos 2px \\
&p_3 = \sin f \cos 4px && p_4 = \sin 2f \\
&p_5 = \sin 2f \cos 2px && p_6 = \sin 2f \cos 4px \\
&p_7 = \sin f \cos 6px && p_8 = \sin 2f \cos 6px \\
&p_9 = \sin 2px && p_{10} = \cos f \sin 2px \\
&p_{11} = \sin 4px && p_{12} = \cos f \sin 4px \\
&p_{13} = \cos 2f \sin 2px && p_{14} = \cos 2f \sin 4px \\
&p_{15} = \sin 6px && p_{16} = \cos f \sin 6px \\
&p_{17} = \cos 2f \sin 6px && p_{18} = 1 - \cos 2px
\end{aligned} \tag{6.2}$$

$p_{19} = 1 - \cos 4px$ $\qquad$ $p_{20} = \cos f(1 - \cos 2px)$

$p_{21} = \cos f(1 - \cos 4px)$ $\qquad$ $p_{22} = \cos 2f(1 - \cos 2px)$

$p_{23} = \cos 2f(1 - \cos 4px)$ $\qquad$ $p_{24} = 1 - \cos 6px$

$p_{25} = \cos f(1 - \cos 6px)$ $\qquad$ $p_{26} = \cos 2f(1 - \cos 6px)$

The following are the displacement results:

d_1 = 2.119	d_2 = -129.9	
d_3 = 112.7	d_4 = 0.03820	
d_5 = 0.03792	d_6 = -0.07367	
d_7 = 15.12	d_8 = -0.003076	
d_9 = -65.05	d_{10} = 2.921	
d_{11} = 28.24	d_{12} = -4.951	
d_{13} = -0.0005101	d_{14} = 0.001761	(6.3)
d_{15} = 2.518	d_{16} = -1.026	
d_{17} = 0.00001215	d_{18} = 0.001540	
d_{19} = 0.002573	d_{20} = -129.9	
d_{21} = 112.7	d_{22} = 0.07543	
d_{23} = -0.1458	d_{24} = 0.002059	
d_{25} = 15.10	d_{26} = -0.005780	

From the displacement results shown in (6.3), certain values are small, particularly those with displacement functions (6.2) that contain $\sin 2f$ and $\cos 2f$. This indicates that those terms are negligible. Figures 6.1 (a) – (f) show the three displacements plotted versus arc length s and angle f under a full snow load F_0 = 1 using the 26 displacement functions. In this case, s = 133.33 and –133.33 at the supports (nondimensionally). Figure 6.2 depicts the plot of displacement w versus arc length s under a full snow load F_0 = 1 without the prestress. Comparing figures 6.1 (f) and 6.2, both plots have the same shape except the latter has a larger magnitude. From the displacement results obtained, the initial prestress on the arch-shell has a significant

impact on the behavior of the structure. The apex deflection is increased by two times when excluding the initial prestress. Figure 6.3 shows the deformation of the cross section at $s = 0$ for $F_0 = 0.001$. Figure 6.4 depicts the deflection of the top meridian (at $f = 0$) for $F_0 = 0.01$ with the solid line representing the undeformed shape.

Results for the stresses and moment under a full snow load of $F_0 = 1$ also are presented. Figure 6.5 shows the plot of stress N_f versus the angle f at $s = 0$. Figure 6.6 depicts the stress N_s versus the arc length s at $f = 0$. Figure 6.7 shows the plot of moment M_s versus the arc length s at $f = 0$. The following are the results for the stresses and moment for $F_0 = 1$:

At $s = 0$ (only the dominant terms),

$$N_f = 20.34\cos f + \frac{1}{1+\frac{800\sec f}{3p}}(-22072\cos f) + \frac{1}{1+\frac{3p\cos f}{800}}(259.3 - 21.57\cos f)$$
$$- \frac{p\sin f}{1+\frac{3p\cos f}{800}}(82.79\sin f)$$

At $f = 0$,

$$N_s = -7.659 - 14.34\cos 2px - 65.99\cos 4px + 21.11\cos 6px$$
$$M_s = -0.0005086 + 0.0001423\cos 2px - 0.0005930\cos 4px$$
$$+ 0.0004523\cos 6px$$

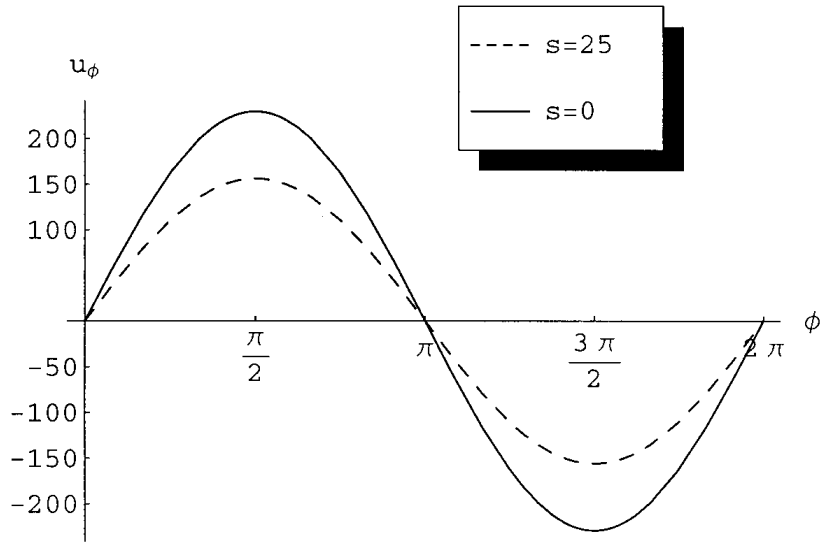

a) u_f versus f for full snow load

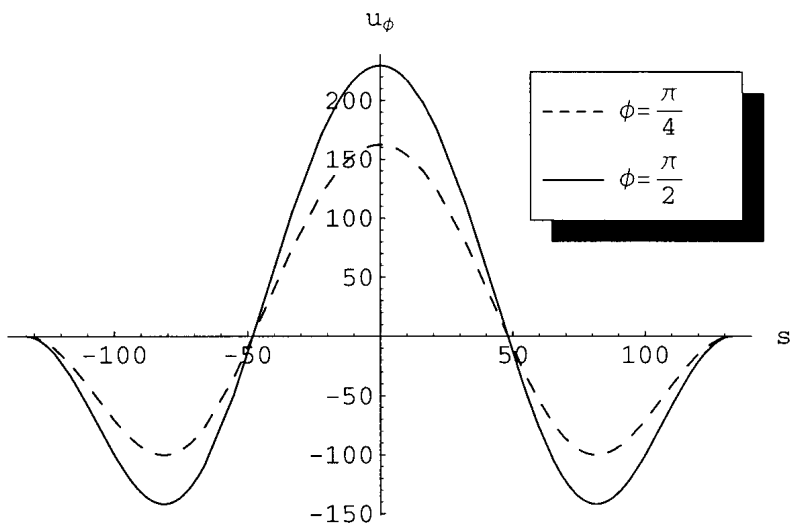

b) u_f versus s for full snow load

Figure 6.1

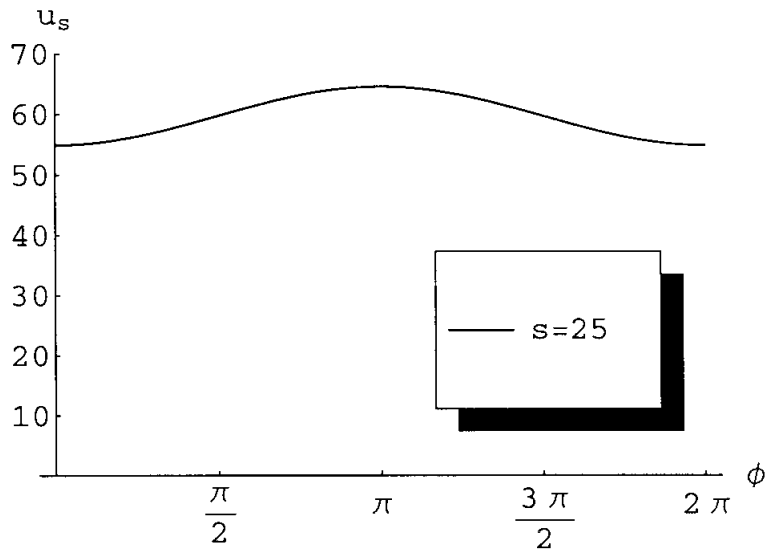

c) u_s versus f for full snow load

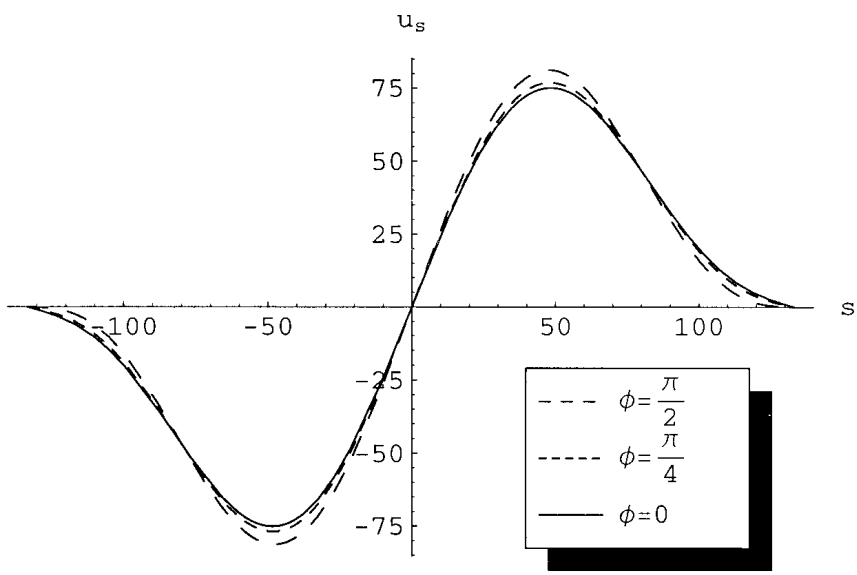

d) u_s versus s for full snow load

Figure 6.1

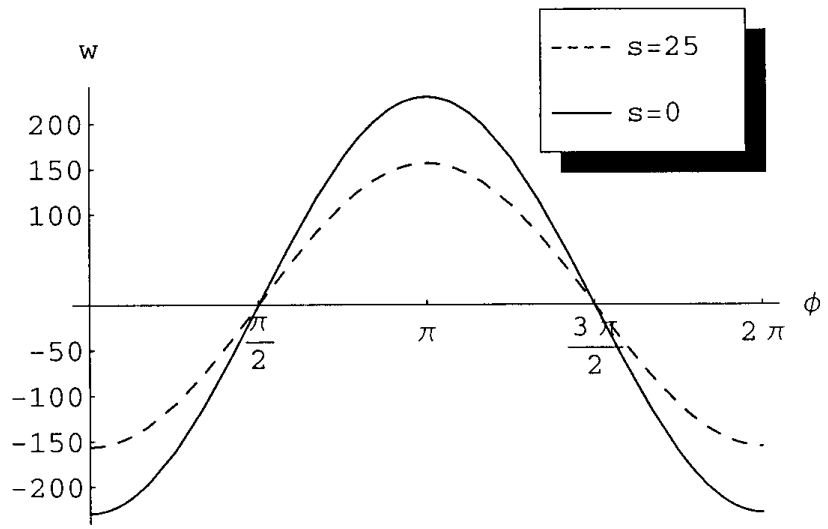

e) *w* versus *f* for full snow load

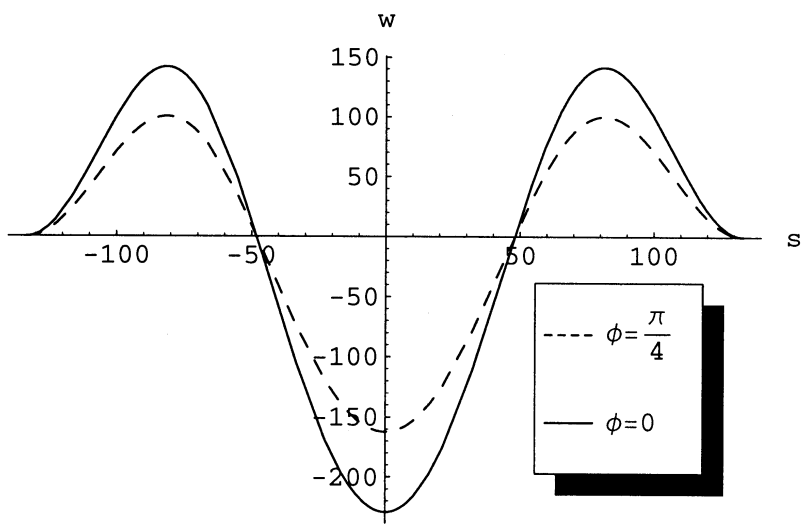

(f) *w* versus *s* for full snow load

Figure 6.1 Displacement plots for full snow load using 26 displacement terms

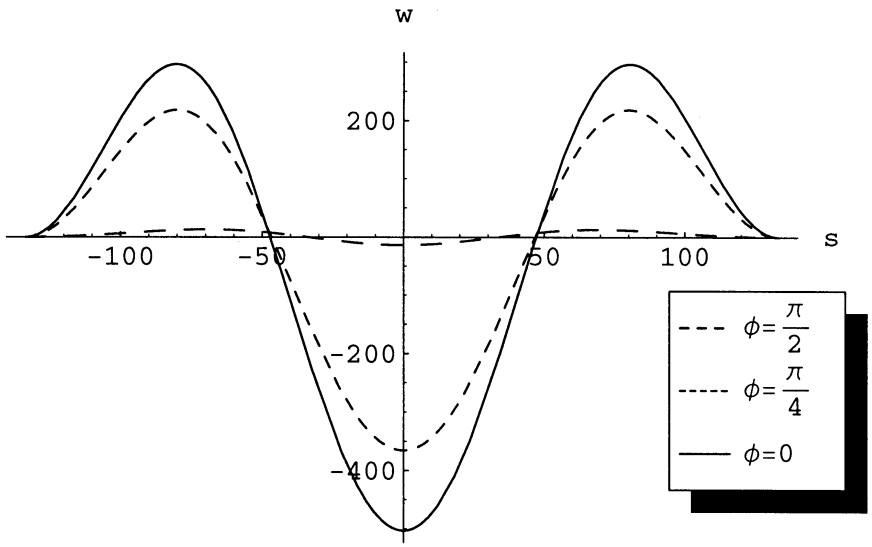

Figure 6.2 *w* versus arc length *s* without prestress

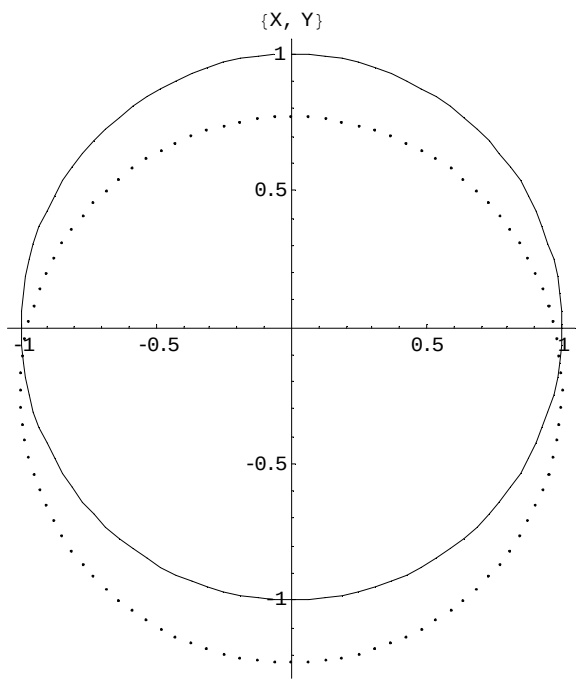

Figure 6.3 Deformation of the cross section at $s = 0$ for $F_0 = 0.001$

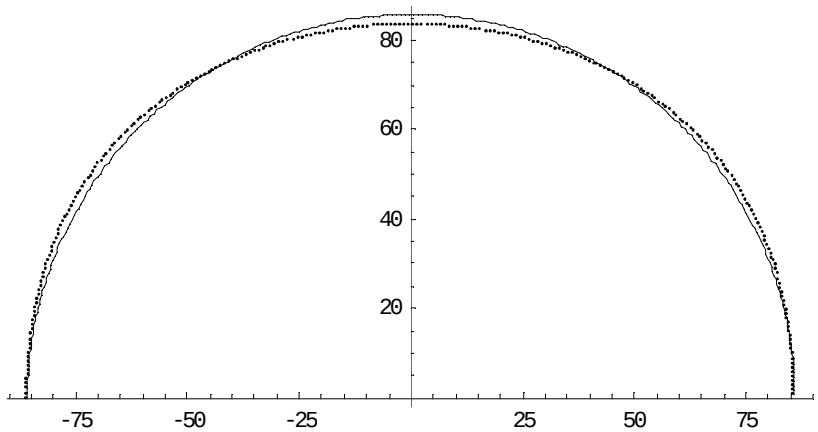

Figure 6.4 Deflection of the top meridian at $f = 0$ for $F_0 = 0.01$

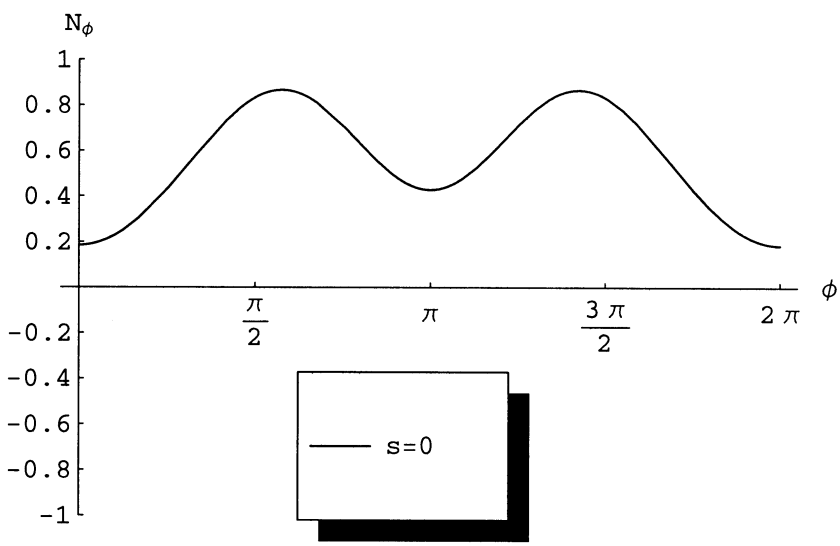

Figure 6.5 N_f versus angle f at $s = 0$ and $F_0 = 1$

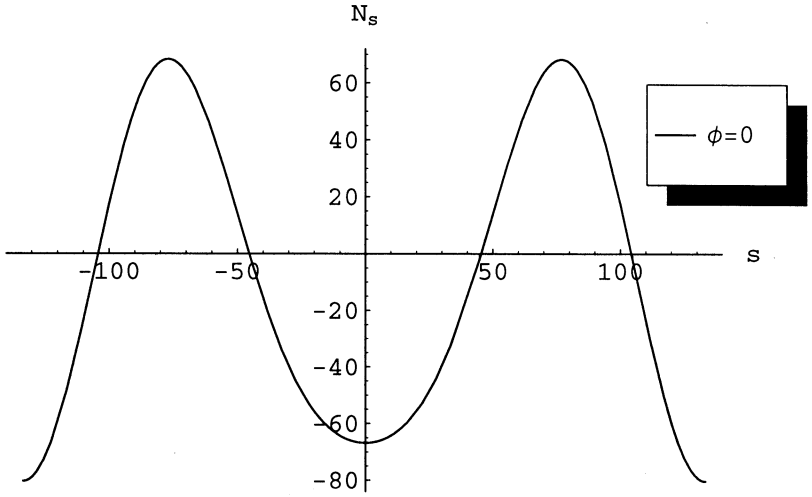

Figure 6.6 N_s versus arc length s at $f = 0$ and $F_0 = 1$

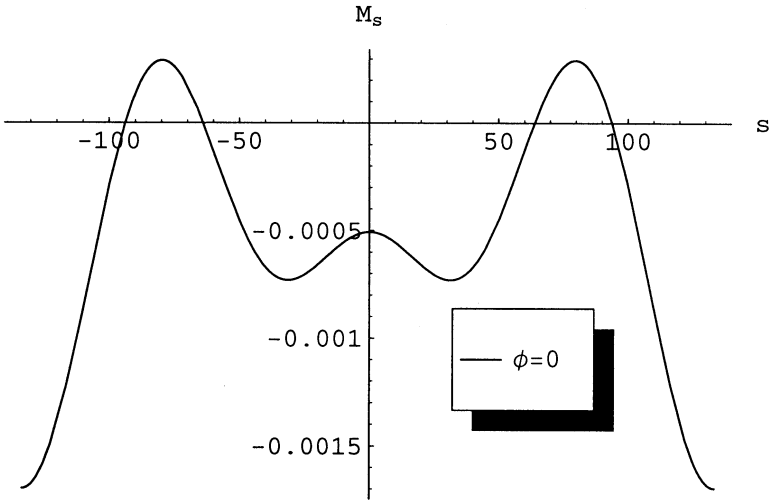

Figure 6.7 M_s versus arc length s at $f = 0$ and $F_0 = 1$

6.2.2 Formulation using 33 Displacement Functions

In this case, the displacement functions are expanded to thirty-three terms by adding more symmetric functions in f and s. The purpose is to determine whether the displacement results change significantly from the formulation using 26 displacement functions. Below are the seven additional displacement functions:

$$
\begin{aligned}
p_{27} &= \sin f \cos 8px & p_{28} &= \sin 2f \cos 8px \\
p_{29} &= \cos f \sin 8px & p_{30} &= \cos 2f \sin 8px \\
p_{31} &= 1 - \cos 8px & p_{32} &= \cos f (1 - \cos 8px) \\
p_{33} &= \cos 2f (1 - \cos 8px)
\end{aligned}
\tag{6.4}
$$

The functions p_{27} and p_{28} are added to u_f, p_{29} and p_{30} are added to u_s, and p_{31} to p_{33} are added to w. The resulting coefficients are:

$$
\begin{aligned}
d_{27} &= 1.065 & d_{28} &= 0.02178 \\
d_{29} &= -0.09798 & d_{30} &= -0.001013 \\
d_{31} &= -0.001188 & d_{32} &= 1.063 \\
d_{33} &= 0.04348
\end{aligned}
\tag{6.5}
$$

From the displacement results obtained, the new values affect the overall displacement very little. The displacement plots are identical to the plots using the formulation of 26 displacement functions except the magnitudes increase a little. This suggests that the solutions are converging.

Figure 6.8 shows the plot of stress N_f versus the angle f at s = 0. Figure 6.9 depicts the stress N_s versus the arc length s at f = 0. Figure 6.10 shows the plot of moment M_s versus the arc length s at f = 0. The following are the results for the stresses and moment for F_0 = 1:

At $s = 0$ (only the dominant terms),

$$N_f = 21.21\cos f + \frac{1}{1+\frac{800\sec f}{3p}}(-22262\cos f) + \frac{1}{1+\frac{3p\cos f}{800}}(259.3 - 21.57\cos f)$$

$$-\frac{p\sin f}{1+\frac{3p\cos f}{800}}(83.51\sin f)$$

At $f = 0$,

$$N_s = -7.545 - 14.49\cos 2px - 65.90\cos 4px + 21.06\cos 6px - 6.701\cos 8px$$

$$M_s = -0.0004663 + 0.00005973\cos 2px - 0.0005083\cos 4px$$

$$+ 0.0003674\cos 6px - 0.0003562\cos 8px$$

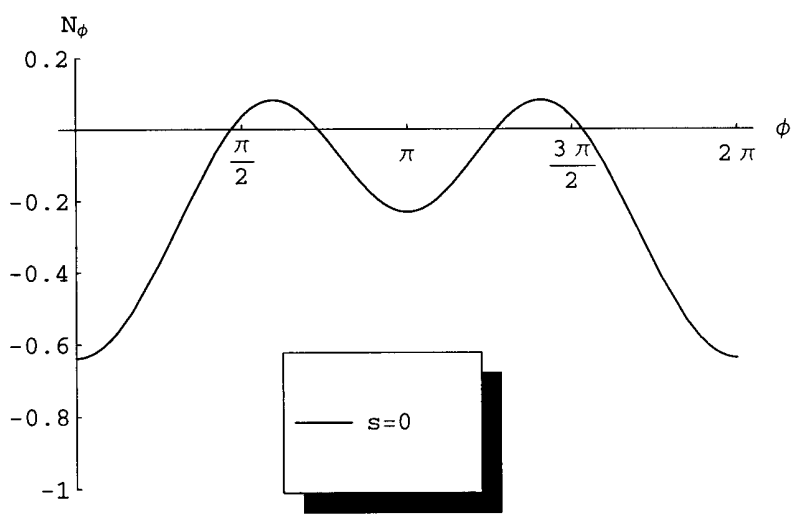

Figure 6.8 N_f versus angle f at s = 0 and F_0 = 1

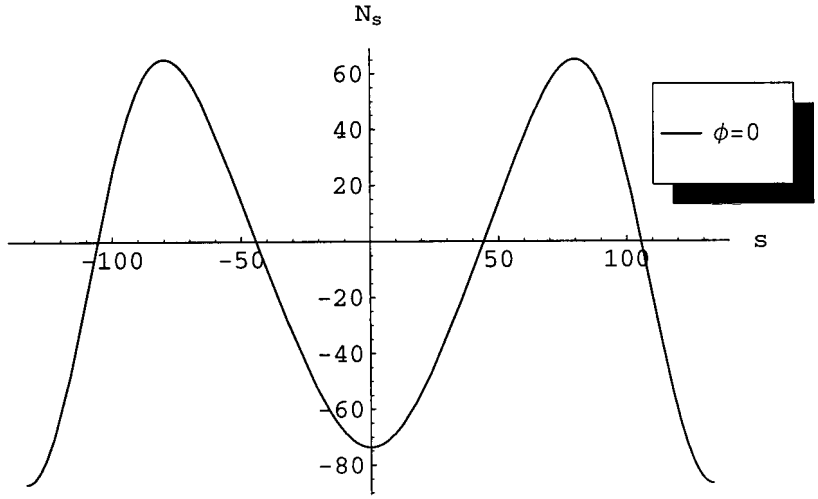

Figure 6.9 N_s versus arc length s at $f = 0$ and $F_0 = 1$

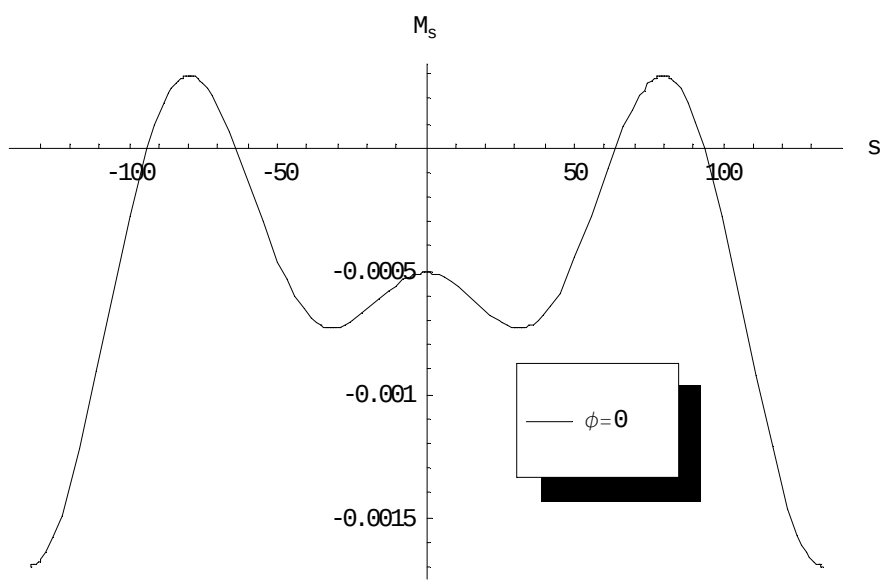

Figure 6.10 M_s versus arc length s at $f = 0$ and $F_0 = 1$

6.3 Half Snow Load

The half snow load with magnitude F_0 is applied on the circular arch-shell as described in section 3.9. The displacement functions are expanded to thirty-three terms by adding more symmetric functions in f. Displacements that are not symmetric in f are not included. The displacement functions used require restriction in displacement w at the base on one side, thus a spring is added to that side (x = 1). Below are the displacement equations:

$$u_f = \sum_{i=1}^{9} d_i p_i \quad , \quad u_s = \sum_{i=10}^{25} d_i p_i \quad , \quad w = \sum_{i=26}^{33} d_i p_i \tag{6.6}$$

where

$$\begin{aligned}
&p_1 = \sin f && p_2 = \sin f \cos px \\
&p_3 = \sin f \cos 2px && p_4 = \sin f \cos 3px \\
&p_5 = \sin f \cos 4px && p_6 = \sin f \cos 5px \\
&p_7 = \sin f \cos 6px && p_8 = \sin f \cos 7px \\
&p_9 = \sin f \cos 8px && p_{10} = \sin px \\
&p_{11} = \sin 2px && p_{12} = \sin 3px \\
&p_{13} = \sin 4px && p_{14} = \cos f \sin px \\
&p_{15} = \cos f \sin 2px && p_{16} = \cos f \sin 3px \\
&p_{17} = \cos f \sin 4px && p_{18} = \sin 5px \\
&p_{19} = \sin 6px && p_{20} = \cos f \sin 5px \\
&p_{21} = \cos f \sin 6px && p_{22} = \sin 7px \\
&p_{23} = \sin 8px && p_{24} = \cos f \sin 7px \\
&p_{25} = \cos f \sin 8px && p_{26} = \cos f (1 - \cos px) \\
&p_{27} = \cos f (1 - \cos 2px) && p_{28} = \cos f (1 - \cos 3px) \\
&p_{29} = \cos f (1 - \cos 4px) && p_{30} = \cos f (1 - \cos 5px)
\end{aligned} \tag{6.7}$$

$$p_{31} = \cos f(1-\cos 6px) \qquad p_{32} = \cos f(1-\cos 7px)$$

$$p_{33} = \cos f(1-\cos 8px)$$

Figure 6.11 shows the downward deflection of the top meridian (at f = 0) with the half snow load distribution of F_0 = 0.5. The displacement results indicate that there is non-symmetry in the displacement u_s with the largest occurring at the top of the arch-shell. From figure 6.11, it can be seen that the right side of the arch-shell near the top deflects downward under the load, and on the left side it bulges outward. Figure 6.12 depicts the deformed shape of the cross section profile at s = 0 under a snow load distribution of F_0 = 0.001. Figure 6.13 (a) – (i) depicts the plots of the three displacements versus the arc length s and angle f under F_0 = 1. The following are the dominant terms for displacements, stresses, and moment for F_0 = 1:

$$u_f = -55.07\sin f\cos px - 66.77\sin f\cos 2px + 66.22\sin f\cos 3px$$
$$+ 56.00\sin f\cos 4px - 14.45\sin f\cos 5px$$
$$u_s = -54.79\sin px - 33.45\sin 2px + 22.07\sin 3px + 14.02\sin 4px$$
$$w = -55.07\cos f(1-\cos px) - 66.77\cos f(1-\cos 2px) + 66.20\cos f(1-\cos 3px)$$
$$+ 55.97\cos f(1-\cos 4px) - 14.44\cos f(1-\cos 5px)$$

At s = 0,

$$N_f = 12.12\cos f + \frac{1}{1+\frac{800\sec f}{3p}}(-11396\cos f) + \frac{1}{1+\frac{3p\cos f}{800}}(133.5 - 12.25\cos f)$$
$$- \frac{p\sin f}{1+\frac{3p\cos f}{800}}(42.75\sin f)$$

At f = 0,

$$N_s = -3.664 - 7.498\cos 2px - 32.97\cos 4px + 10.48\cos 6px - 21.09\sin 3px$$
$$-13.67\sin 5px$$
$$M_s = -0.0001852\cos 2px + 0.0007776\cos 4px - 0.0002436\cos 6px$$
$$-0.0004903\sin 3px - 0.0003212\sin 5px$$

Figure 6.14 shows the plot of stress N_f versus the angle f at s = 0. Figure 6.15 depicts the stress N_s versus the arc length s at f = 0. Figure 6.16 shows the plot of moment M_s versus the arc length s at f = 0. All the stresses and moment are under a load of F_0 = 1

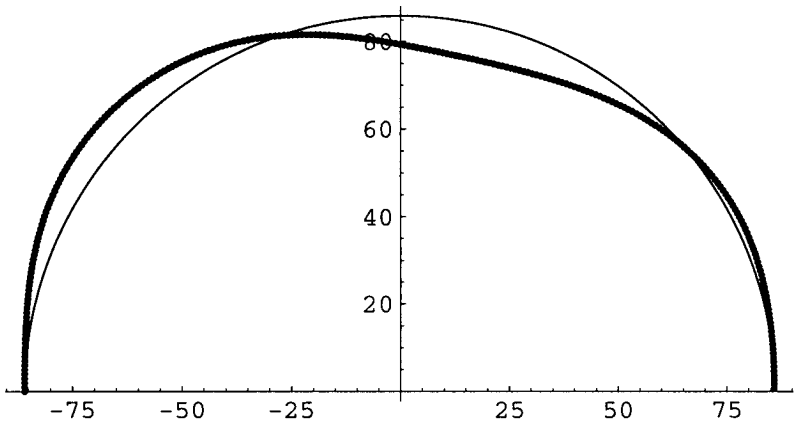

Figure 6.11 Deflection of the top meridian at f = 0 for F_0 = 0.5

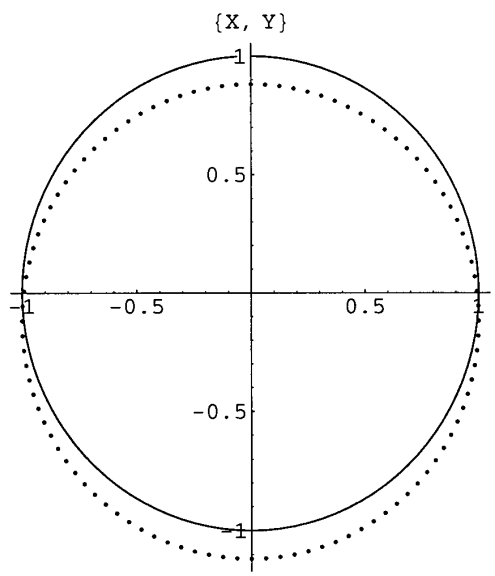

Figure 6.12 Deformation of the cross section at s = 0 for F_0 = 0.001

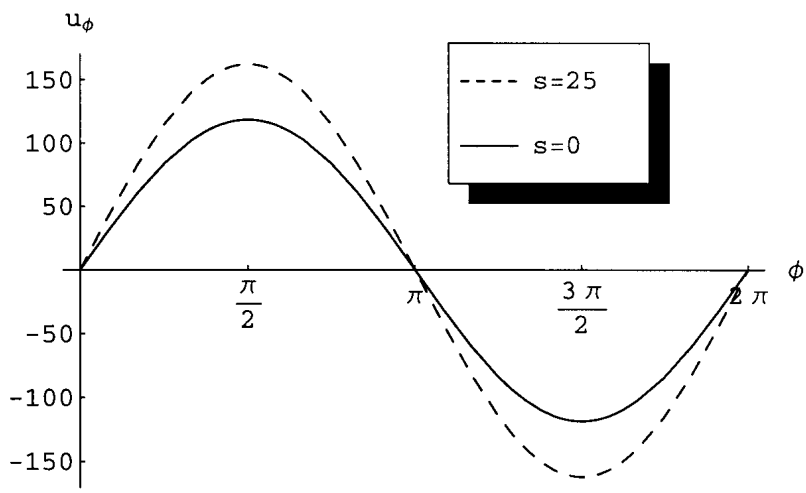

a) u_f versus f for half snow load

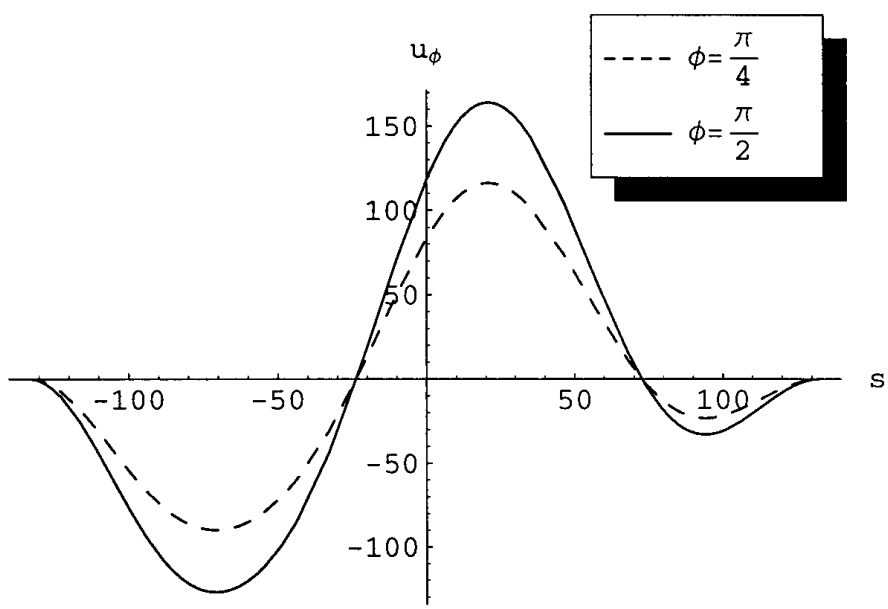

b) u_f versus s for half snow load

Figure 6.13

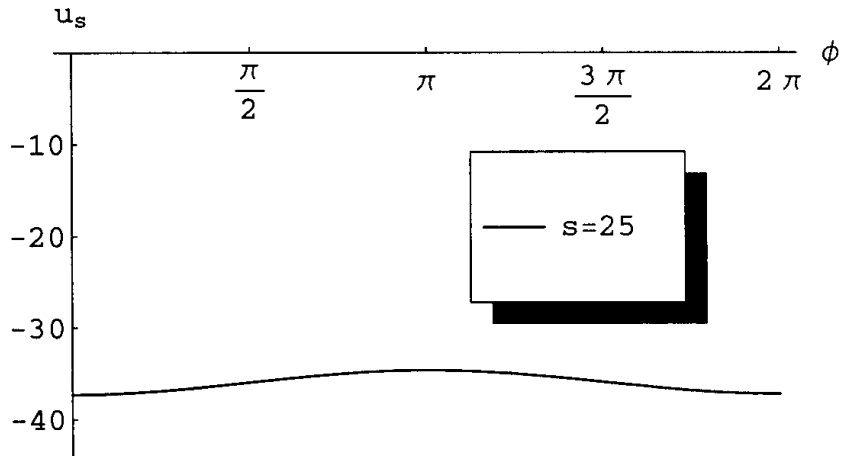

c) u_s versus f for half snow load

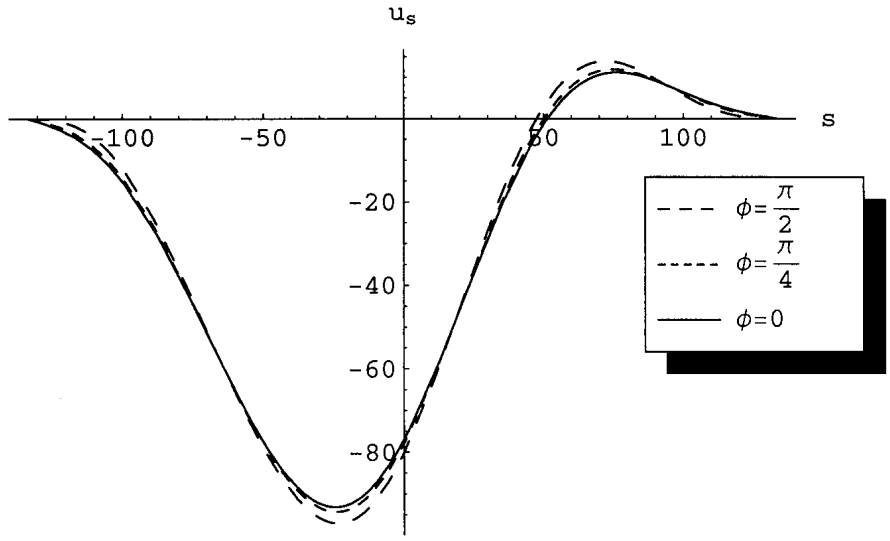

d) u_s versus s for half snow load

Figure 6.13

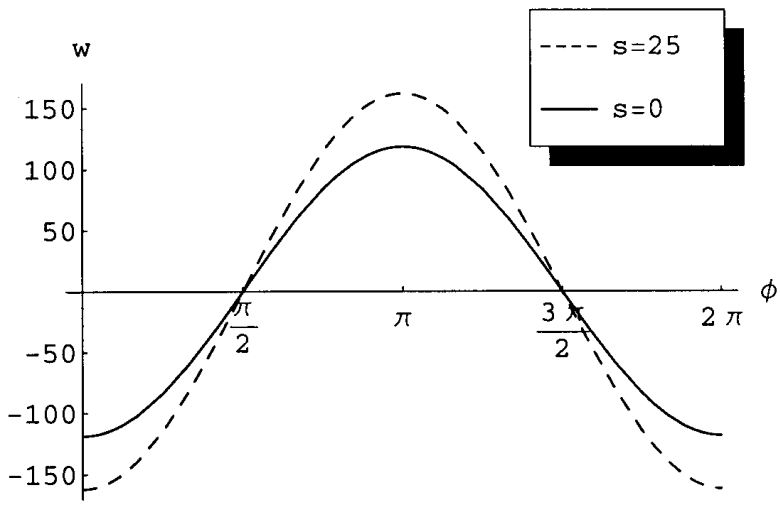

e) *w* versus *f* for half snow load

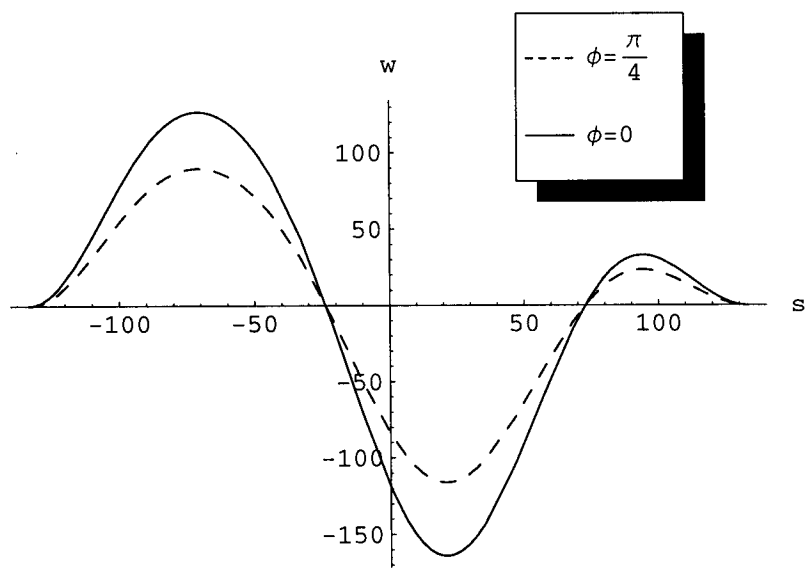

f) *w* versus *s* for half snow load

Figure 6.13 Displacement plots for half snow load

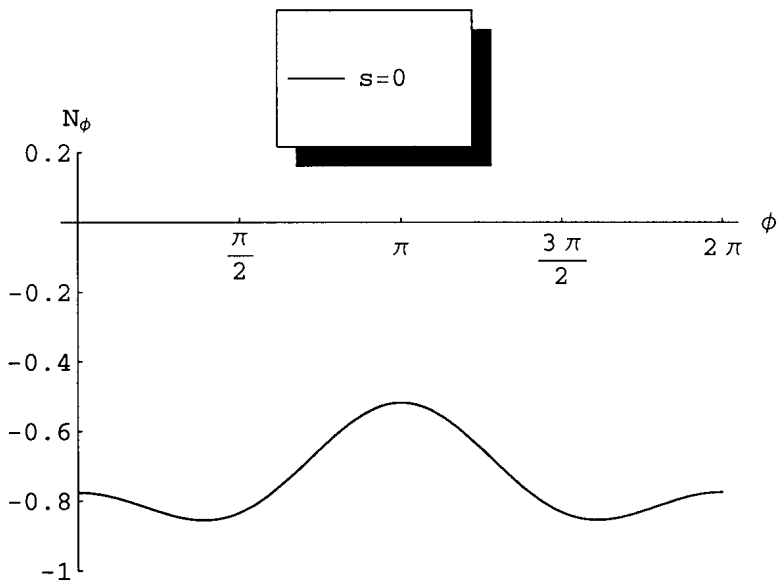

Figure 6.14 N_f **versus angle** f **at** s **= 0 and** F_0 **= 1**

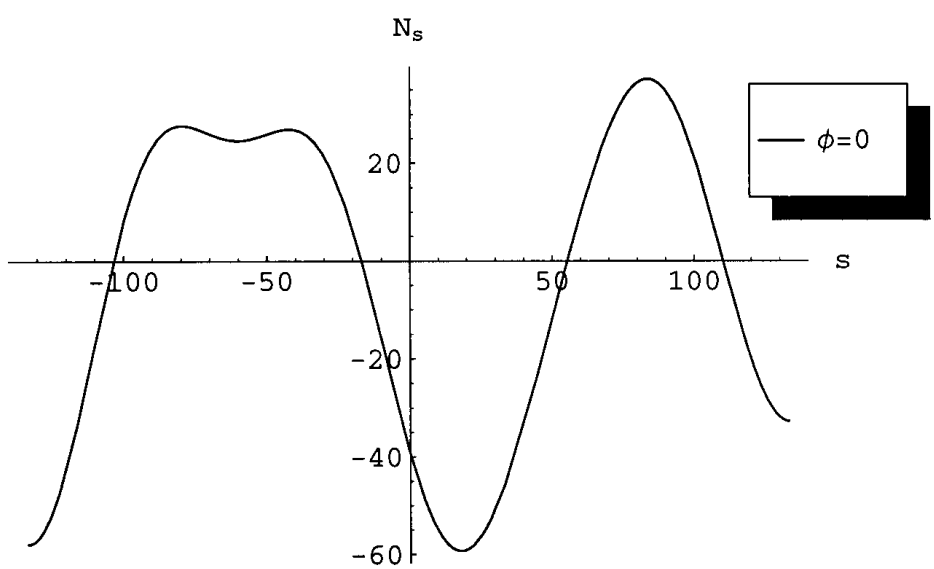

Figure 6.15 N_s **versus arc length** s **at** f **= 0 and** F_0 **= 1**

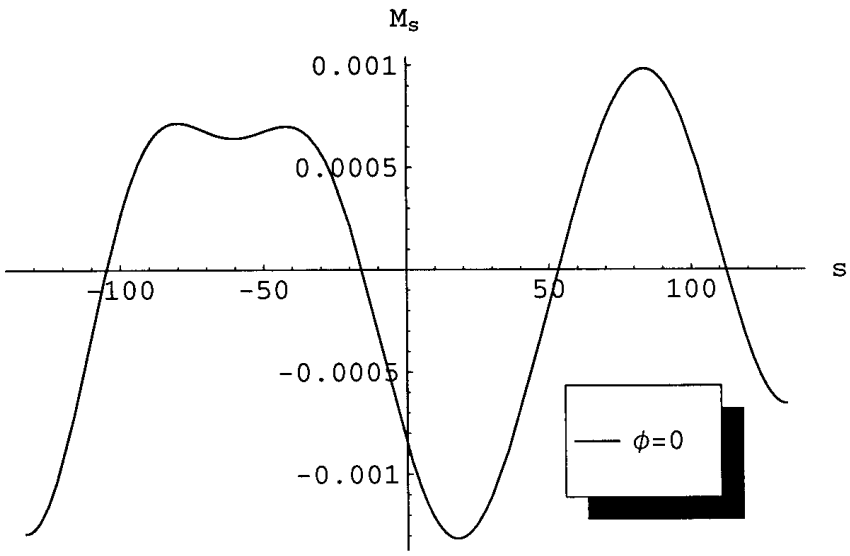

Figure 6.16 M_s versus arc length s at f = 0 and F_0 = 1

6.4 Wind Load

The rough wind distribution as described in (3.9.31) is used as the pressure distribution on the circular arch-shell. The distribution is applied to the arch-shell as described in section 3.9. In this case, the same displacement functions are utilized as in section 6.3 for the half snow load, since the wind pressure is also symmetric in f but not s.

Figures 6.17 shows the deflection of the top meridian (at f = 0) with the wind pressure of Q = 0.05. From figure 6.17, it can be seen that the left side of the arch-shell deflects inwards due to the wind pressure and bulges outward on the right side due to the suction. Figure 6.18 depicts the deformation of the cross section at s = 0 under a wind pressure distribution of Q = 0.001. Figure 6.19 (a) – (f) depicts the plots of the three

displacements versus the arc length s and angle f under $Q = 0.01$. The following are the dominant terms for displacements, stresses, and moment under $Q = 1$:

$$u_f = -132.2\sin f\cos px + 89.44\sin f\cos 2px - 77.67\sin f\cos 3px$$
$$- 61.04\sin f\cos 4px - 41.98\sin f\cos 5px$$
$$u_s = -132.2\sin px + 44.74\sin 2px - 25.90\sin 3px - 15.26\sin 4px$$
$$w = -132.2\cos f(1-\cos px) + 89.43\cos f(1-\cos 2px) - 77.64\cos f(1-\cos 3px)$$
$$- 61.00\cos f(1-\cos 4px) - 41.94\cos f(1-\cos 5px)$$

At $s = 0$,

$$N_f = 12.12\cos f + \frac{1}{1+\frac{800\sec f}{3p}}(-13462\cos f) + \frac{1}{1+\frac{3p\cos f}{800}}(156.2 - 12.35\cos f)$$
$$- \frac{p\sin f}{1+\frac{3p\cos f}{800}}(50.49\sin f)$$

At $f = 0$,

$$N_s = 8.246 + 10.50\cos 2px + 36.20\cos 4px - 26.82\cos 6px + 16.79\cos 8px$$
$$+ 24.53\sin 3px - 39.79\sin 5px + 23.75\sin 7px$$
$$M_s = 0.0002483\cos 2px + 0.0008476\cos 4px - 0.0006308\cos 6px$$
$$+ 0.0003982\cos 8px - 0.0005751\sin 3px - 0.0009331\sin 5px$$
$$+ 0.0005608\sin 7px$$

Figure 6.20 shows the plot of stress N_f versus the angle f at $s = 0$. Figure 6.21 depicts the stress N_s versus the arc length s at $f = 0$. Figure 6.22 shows the plot of moment M_s versus the arc length s at $f = 0$. All the stresses and moment are under a wind pressure of $Q = 1$.

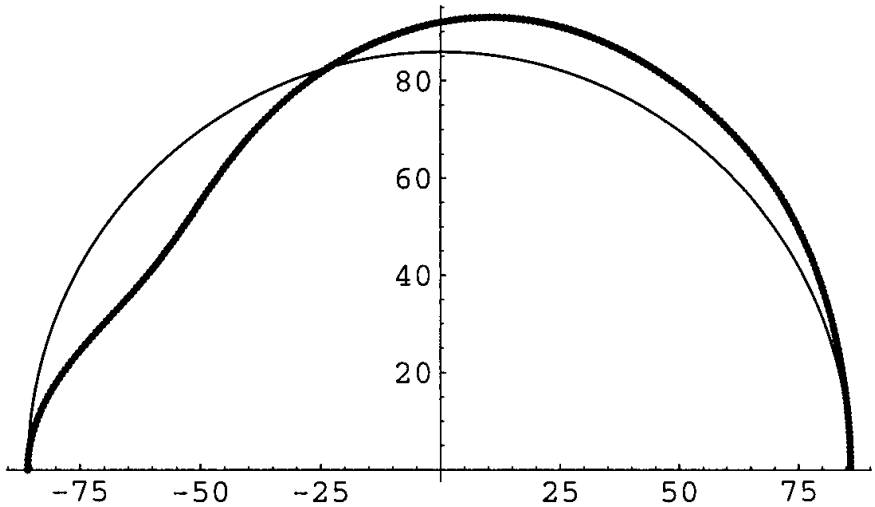

Figure 6.17 Deflection of the top meridian at *f* = 0 for *Q* = 0.05

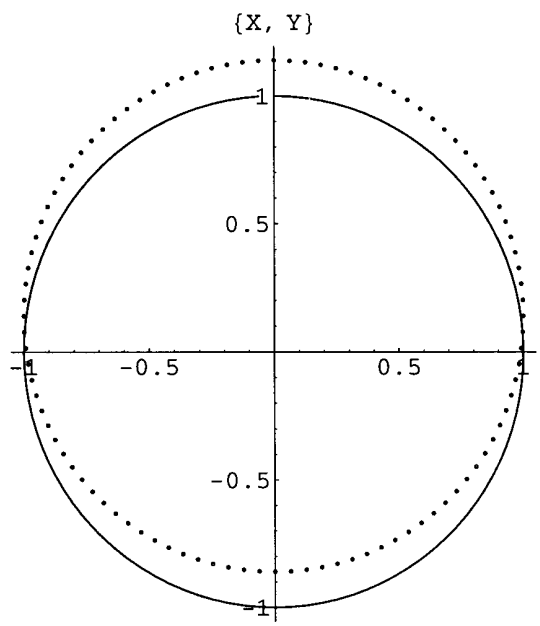

Figure 6.18 Deformation of the cross section at *s* = 0 for *Q* = 0.001

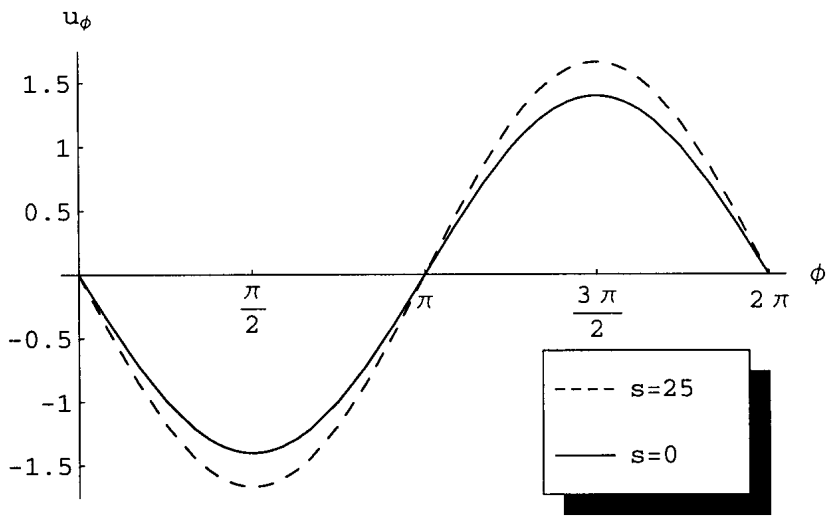

a) u_f versus f for wind load

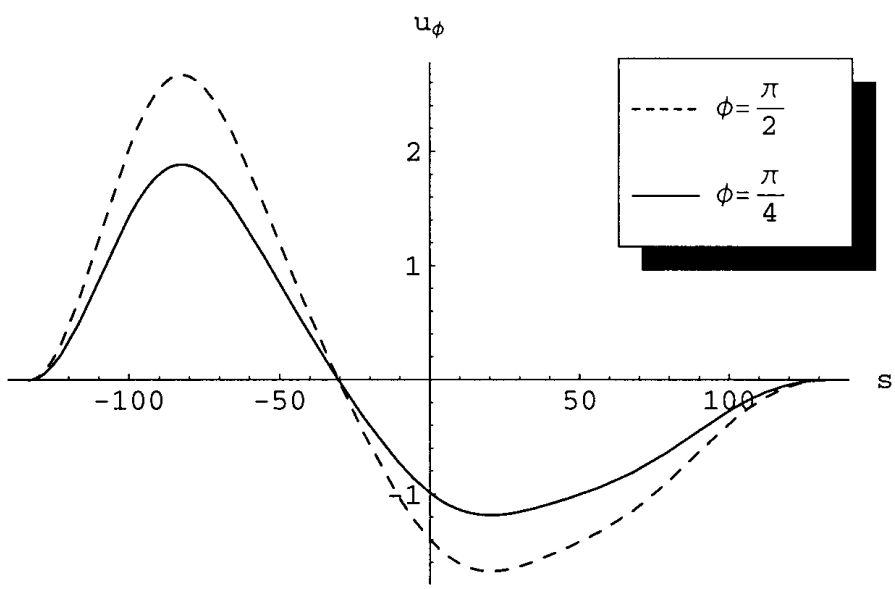

b) u_f versus s for wind load

Figure 6.19

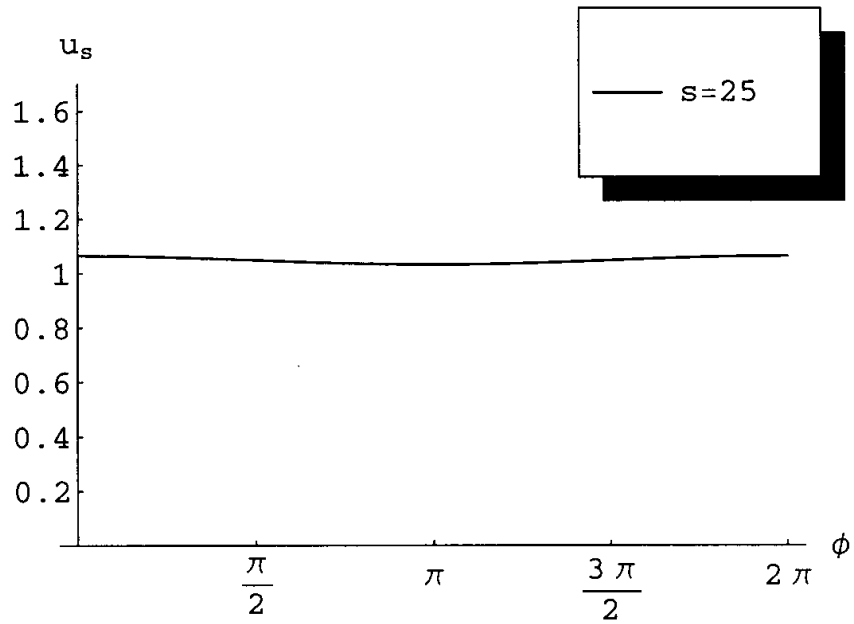

c) u_s versus f for wind load

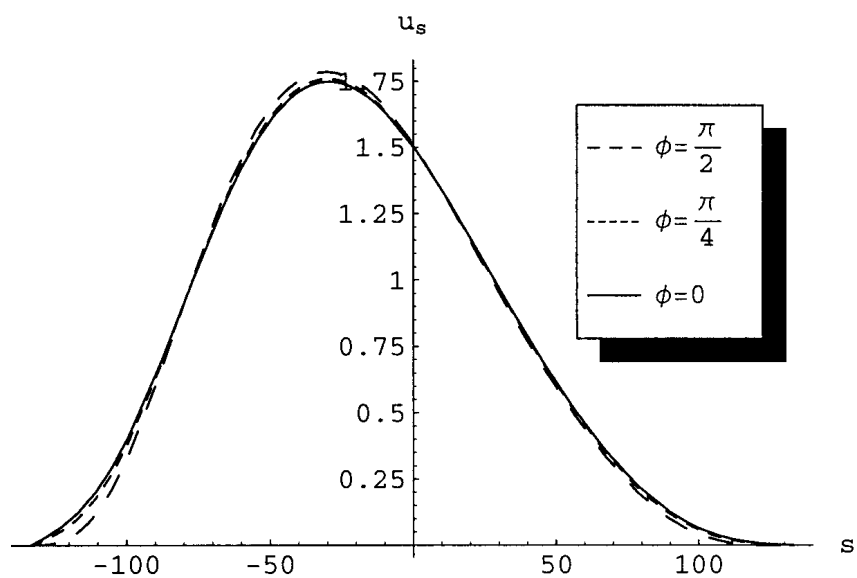

d) u_s versus s for wind load

Figure 6.19

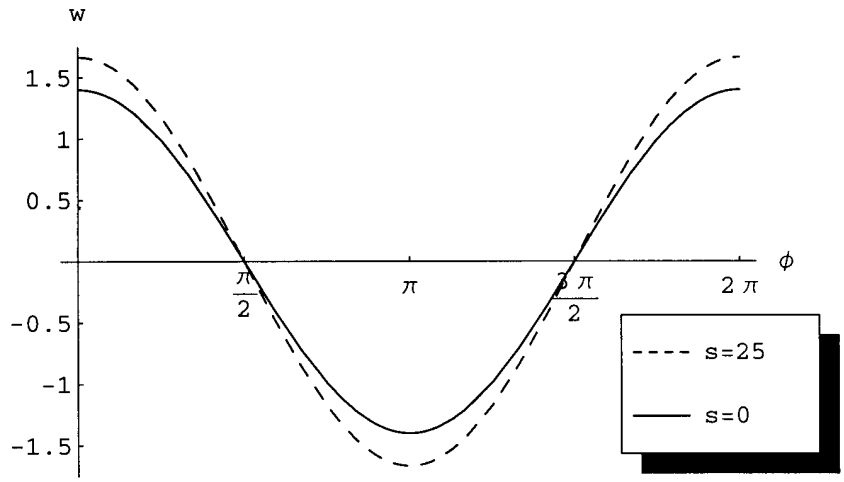

e) *w* versus *f* for wind load

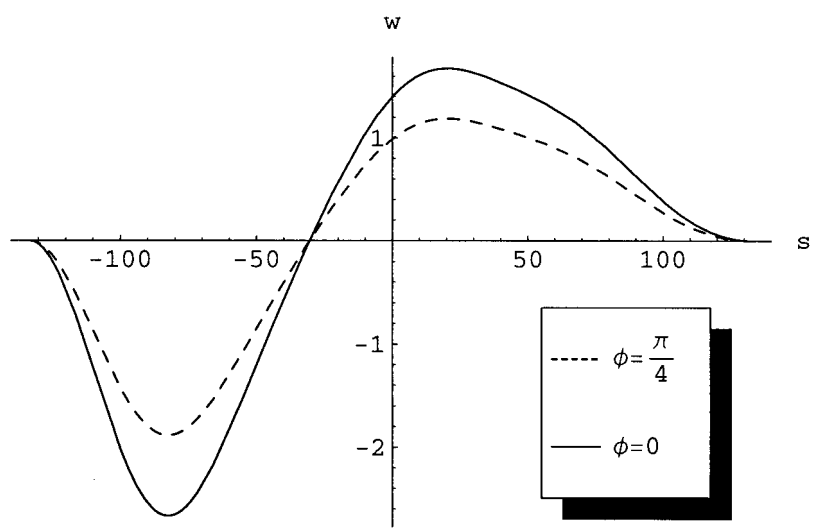

f) *w* versus *s* for wind load

Figure 6.19 Displacement plots for wind load

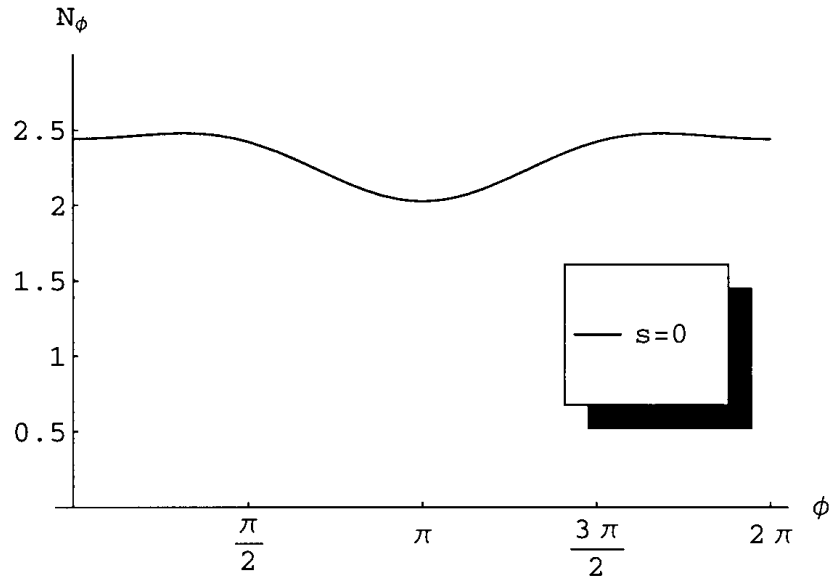

Figure 6.20 N_f versus angle f at s = 0 and Q = 1

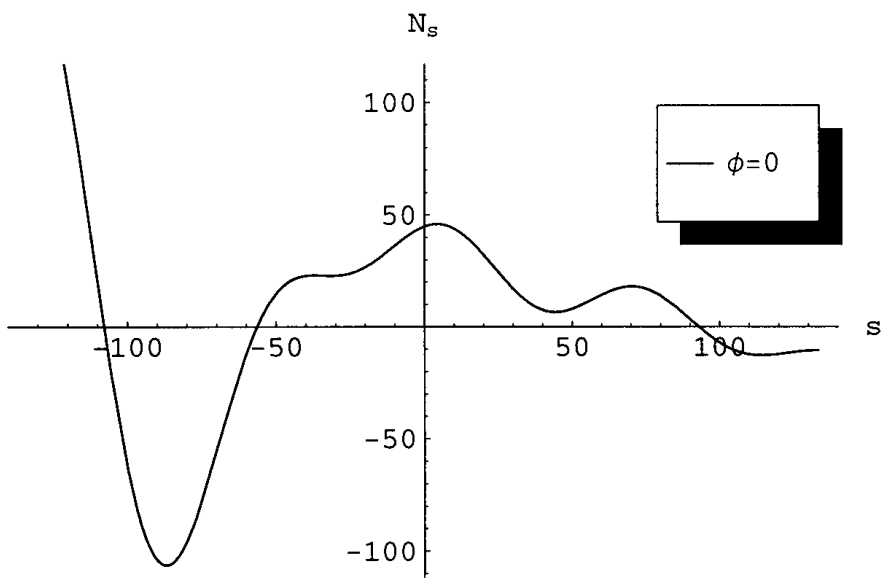

Figure 6.21 N_s versus arc length s at f = 0 and Q = 1

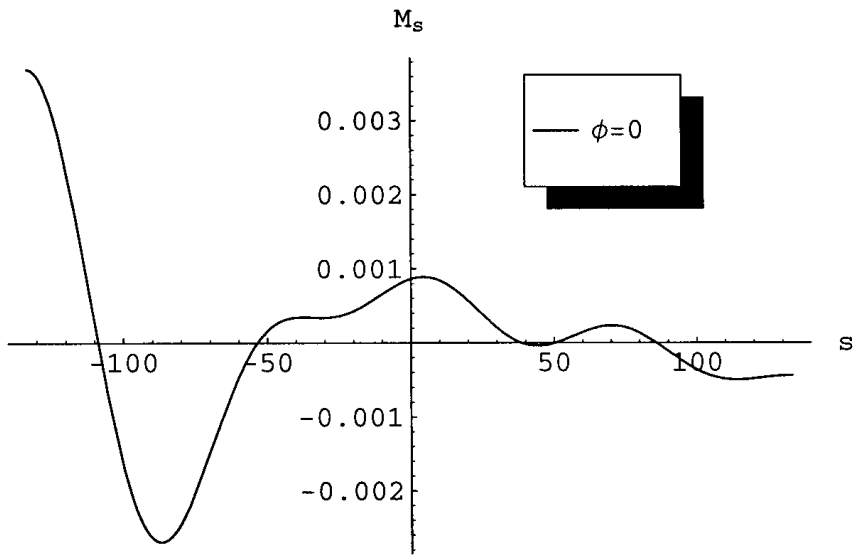

Figure 6.22 M_s versus arc length s at f = 0 and Q = 1

6.5 Side Load

The uniform side load J is applied as described in section 3.9. The displacement functions are expanded to thirty terms by adding more symmetric functions in s. Terms that are not symmetric in s are not included. The new functions, like the case for full snow load eliminate the need for the springs at the support and for (3.8.5). They model the supports as clamped bases and will give radial displacement w = 0 at the bases. Below are the displacement equations:

$$u_f = \sum_{i=1}^{12} d_i p_i \quad , \quad u_s = \sum_{i=13}^{21} d_i p_i \quad , \quad w = \sum_{i=22}^{30} d_i p_i \tag{6.8}$$

where

$$p_1 = 1 \qquad\qquad p_2 = \sin f$$

$$
\begin{aligned}
&p_3 = \cos f && p_4 = \cos 2px \\
&p_5 = \sin f \cos 2px && p_6 = \cos f \cos 2px \\
&p_7 = \cos 4px && p_8 = \sin f \cos 4px \\
&p_9 = \cos f \cos 4px && p_{10} = \cos 6px \\
&p_{11} = \sin f \cos 6px && p_{12} = \cos f \cos 6px \\
&p_{13} = \sin 2px && p_{14} = \sin 4px \\
&p_{15} = \sin f \sin 2px && p_{16} = \sin f \sin 4px \\
&p_{17} = \cos f \sin 2px && p_{18} = \cos f \sin 4px \\
&p_{19} = \sin 6px && p_{20} = \sin f \sin 6px \\
&p_{21} = \cos f \sin 6px && p_{22} = 1 - \cos 2px \\
&p_{23} = 1 - \cos 4px && p_{24} = \sin f (1 - \cos 2px) \\
&p_{25} = \sin f (1 - \cos 4px) && p_{26} = \cos f (1 - \cos 2px) \\
&p_{27} = \cos f (1 - \cos 4px) && p_{28} = 1 - \cos 6px \\
&p_{29} = \sin f (1 - \cos 6px) && p_{30} = \cos f (1 - \cos 6px)
\end{aligned}
\tag{6.9}
$$

Figure 6.23 shows the deformation of the cross section of the arch-shell at arc length s = 0 at the center for J = 0.0001. From figure 6.23, it can be seen the deformed cross section moves sideways. Figure 6.24 (a) – (f) depicts the plots of the three displacements versus the arc length s and angle f under J = 0.1. The following are the dominant terms for displacements, stresses, and moment:

$$
\begin{aligned}
u_f &= 2156 \cos f + 1942 \cos f \cos 2px + 177.3 \cos f \cos 4px \\
&\quad + 37.08 \cos f \cos 6px \\
u_s &= 45.67 \sin f \sin 2px + 8.309 \sin f \sin 4px + 2.588 \sin f \sin 6px \\
w &= -1942 \sin f (1 - \cos 2px) - 177.2 \sin f (1 - \cos 4px) - 37.03 \sin f (1 - \cos 6px)
\end{aligned}
$$

At s = 0,

$$N_f = 8.022\sin f + \frac{1}{1+\frac{800\sec f}{3p}}(-38053\sin f) + \frac{1}{1+\frac{3p\cos f}{800}}(8.346\sin f)$$

$$-\frac{p\sin f}{1+\frac{3p\cos f}{800}}(42.75\sin f)$$

At $f = 0$,

$$N_s = -0.003662 - 0.004351\cos 2px - 0.01597\cos 4px + 0.01256\cos 6px$$

$$M_s = -9.682*10^{-8}\cos 2px - 3.740*10^{-7}\cos 4px + 2.942*10^{-7}\cos 6px$$

Figure 6.25 shows the plot of stress N_f versus the angle f at s = 0. Figure 6.26 depicts the stress N_s versus the arc length s at f = 0. Figure 6.27 shows the plot of moment M_s versus the arc length s at f = 0. All the stresses and moment are under a uniform side load of J = 0.1.

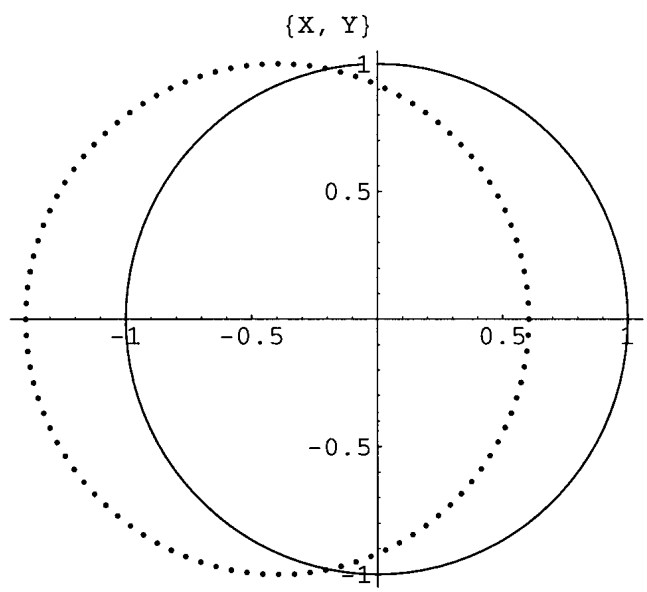

Figure 6.23 Deformation of the cross section at s = 0 for J = 0.0001

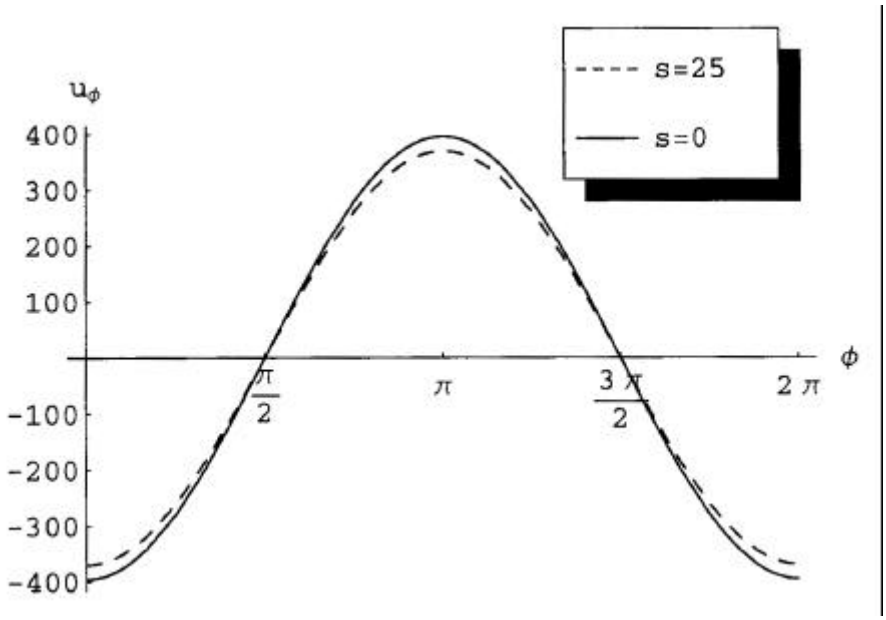

a) u_f versus f for side load

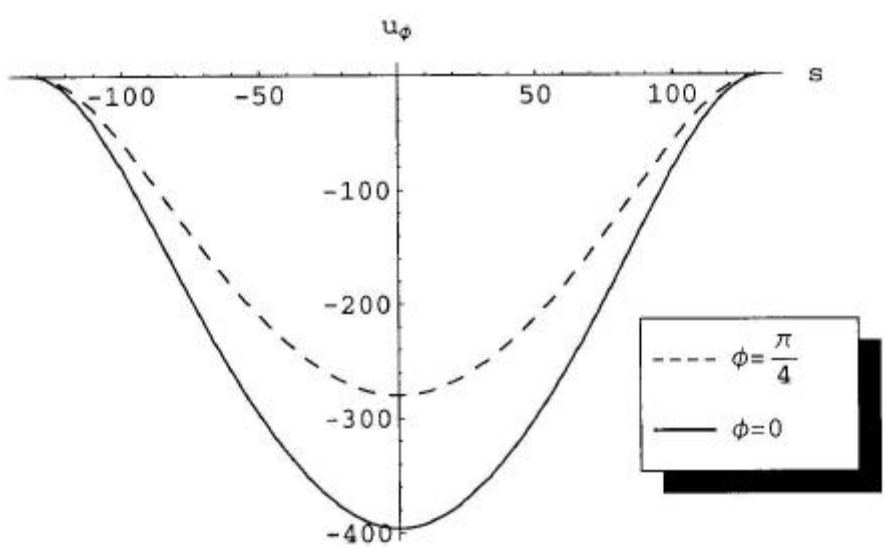

b) u_f versus s for side load

Figure 6.24

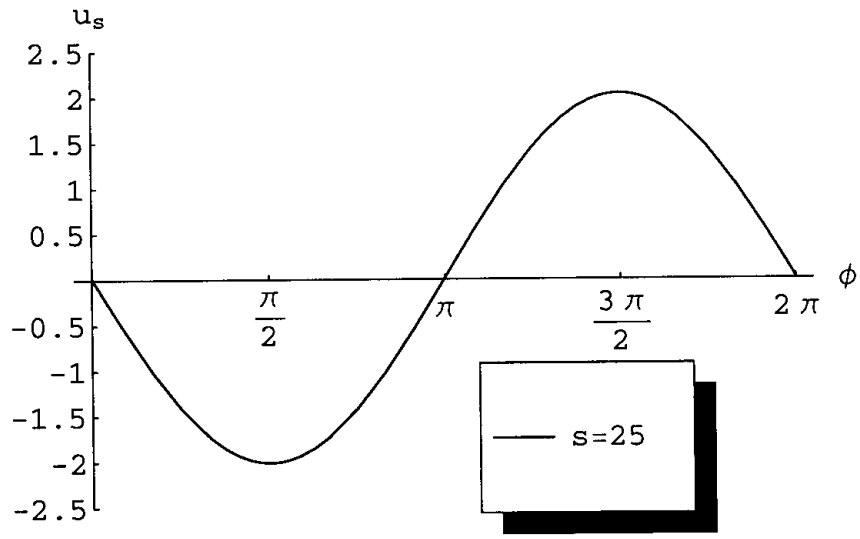

c) u_s versus f for side load

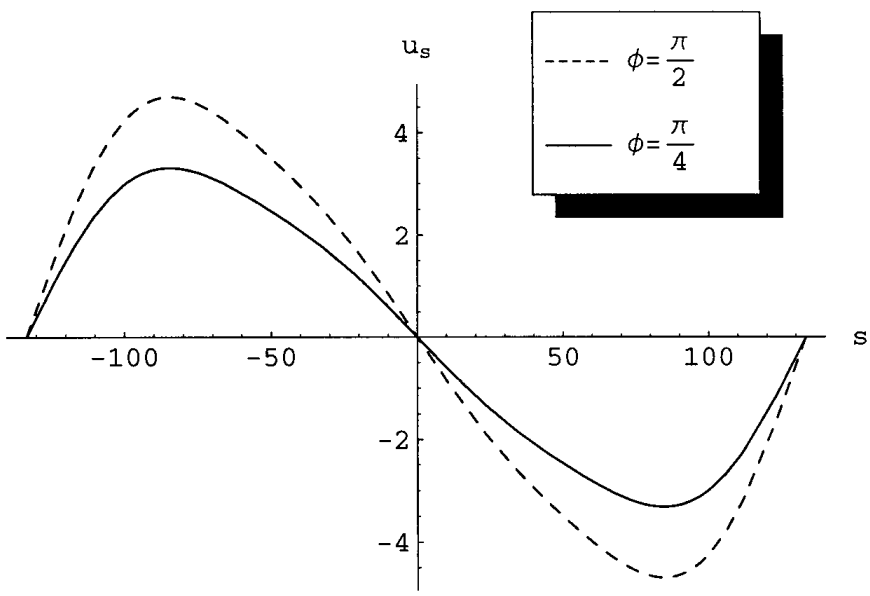

d) u_s versus s for side load

Figure 6.24

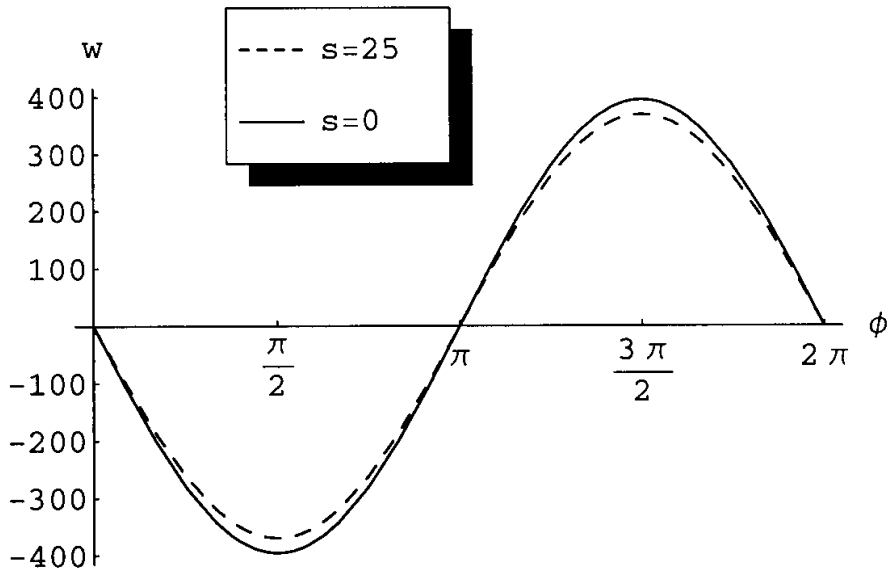

e) *w* versus *f* for side load

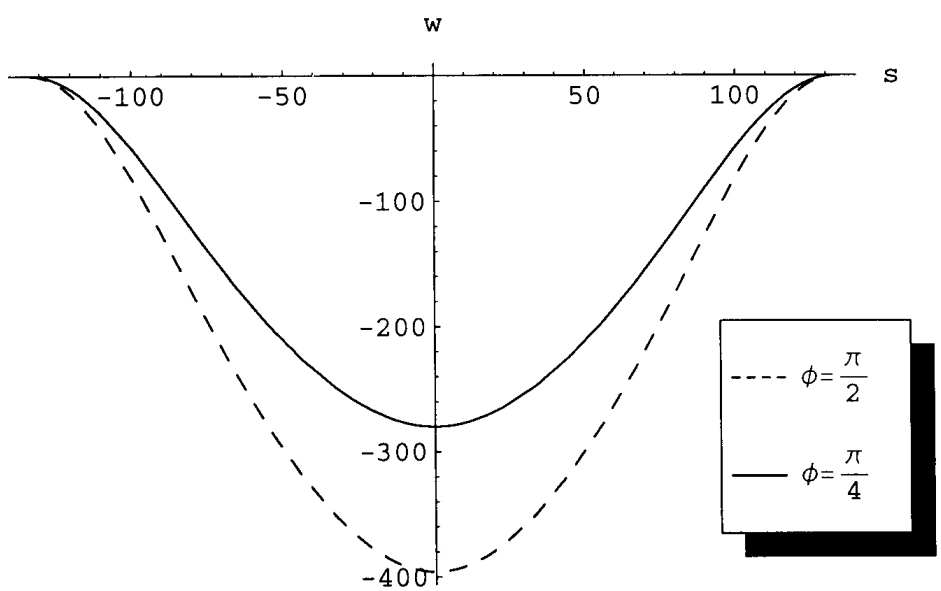

f) *w* versus *s* for side load

Figure 6.24 Displacement plots for side load

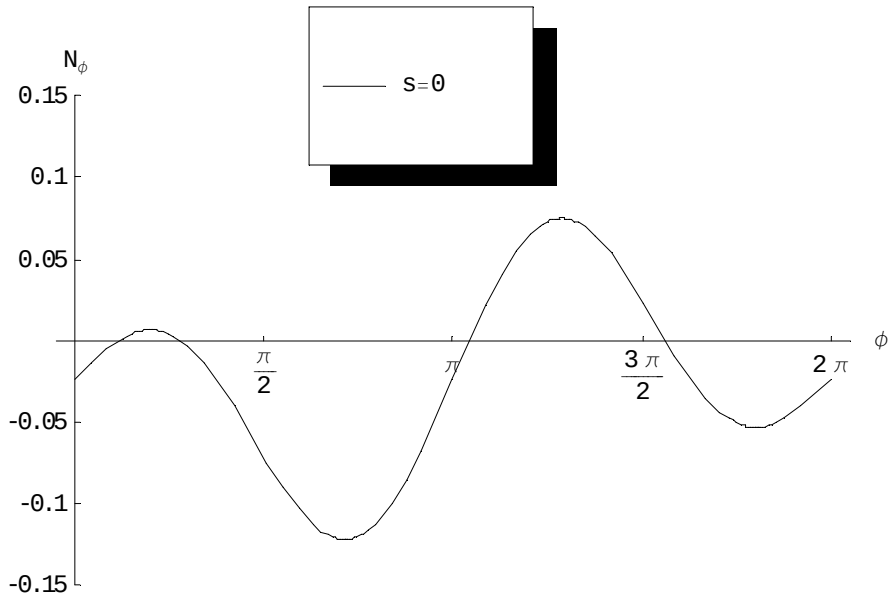

Figure 6.25 N_f versus angle f at s = 0 and J = 0.1

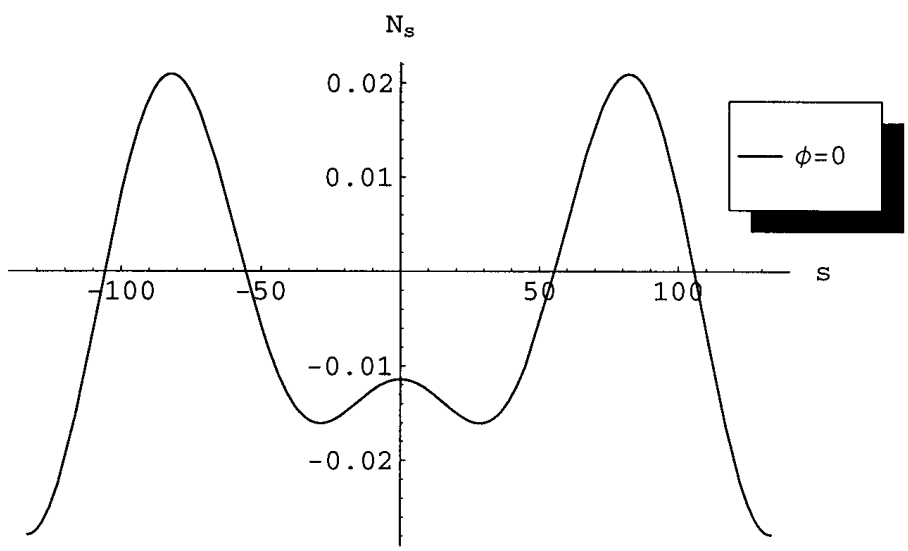

Figure 6.26 N_s versus arc length s at f = 0 and J = 0.1

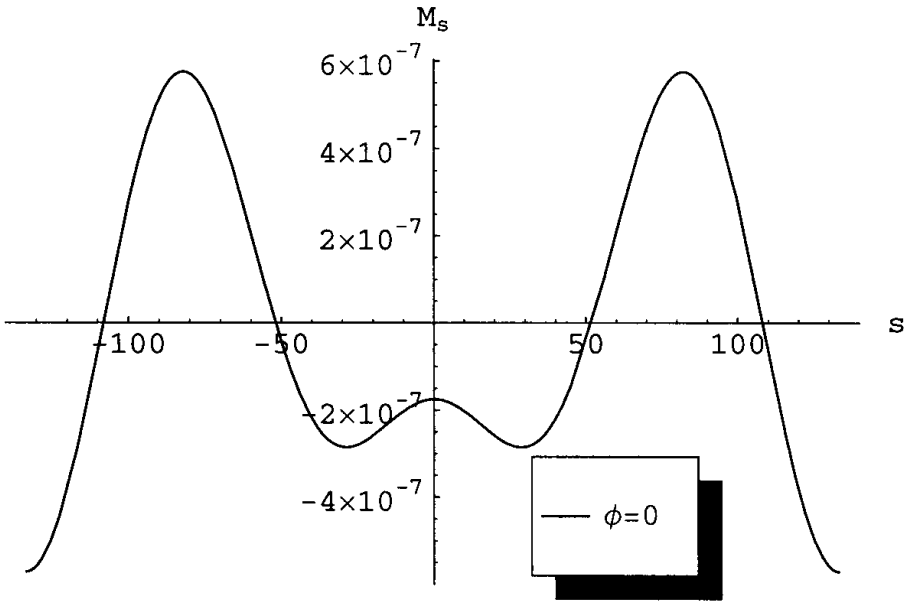

Figure 6.27 M_s versus arc length s at f = 0 and J = 0.1

CHAPTER 7 CONCLUSIONS AND RECOMMENDATIONS

7.1 Conclusions

The behavior of two general arch-shell shapes was investigated under full and half snow loads, a wind load, and uniform side load. In addition, modified symmetric displacement formulations for the circular arch-shell under the loads mentioned above were investigated. The conclusions drawn from these investigations will be summarized below, along with recommendations for future research.

For both shapes, a circular and non-circular arch-shell, the results obtained indicate that the general displacement equations used in (3.10.1) – (3.10.3) are not sufficient to accurately model their behavior under the load types discussed in section 3.9. The reason is that the general equations do not have enough symmetric and non-symmetric terms in f and s, which restricts the displacements of the structure. The displacement u_s for both shapes shows some non-symmetry under half snow loading but the values are very small compared to those from the symmetric terms. This indicates that there might be a lack of important non-symmetric terms in the general displacement equations used in Chapters 4 and 5.

In order to improve the results, modified displacement formulations were investigated for a circular arch-shell under several types of loading. In these new formulations, all the terms in the previous formulations which gave zero values were taken out and replaced by additional terms symmetric in f or s, depending on the loading. In Chapter 6, the behavior of a circular arch-shell was investigated under full and half snow loads, a wind load, and uniform side load. The arch-shell with cross section radius r = 0.15m and an internal pressure p = 400 kPa was considered.

Two cases of full snow load were investigated, using 26 and 33 displacement functions. For the case using 26 displacement functions, the results obtained show a significant improvement in modeling the behavior of the arch-shell under the same

loading magnitude compared to using the general displacement equations in Chapters 4 and 5. Figure 6.4 shows that the arch-shell deflects downward at the apex and bulges outward on the sides, whereas the arch-shell only deflected downward for the general case as shown in figure 4.1. The contribution of initial prestress to the overall deflection is also excluded to investigate its impact on the arch-shell. The results indicate that the initial prestress from the internal pressure has a significant impact on the overall deflection, as the apex displacement increased by two times when excluding the initial prestress. For the case using 33 displacement functions by adding additional symmetric terms in f and s, the results obtained show the same behavior as the previous case using 26 terms under the same loading except for the magnitude which changes a little. This indicates that the solution should be converging.

For the half snow load, using new formulated displacement functions, the results obtained show good behavior of the arch-shell under this type of loading as compared to results from Chapter 4. Figure 6.11 depicts the arch-shell deflecting downward on one side under the loading and bulging outward on the other side, as expected under this type of loading.

The results obtained for the wind pressure show a significant improvement in modeling the arch-shell under this type of load compared to results from Chapter 4. Figure 6.17 shows the arch-shell deflected inward on one side due to the wind pressure compressing the structure and bulging outward on another side due to suction by the wind.

In the case of uniform side load, making use of the symmetric properties, the results obtained were also good in modeling the behavior of the arch-shell under this type of load. Figure 6.23 shows the cross section of the structure moving sideways due to the load.

Overall, if enough symmetric and non-symmetric terms are taken when using the

formulated equations, good results can be obtained in modeling the behavior of the arch-shell under the various loadings mentioned above.

Throughout the analysis in this research, the program Mathematica was applied to the formulated equations to find the displacements, stresses, and moments along the arch-shell. Some conclusions can be drawn from the application of this program. Mathematica is essentially a very useful, powerful, and user-friendly program. It can handle complex derivatives, integration, and differential equations. Plots are easy to generate and to import and export to other software programs. It is compatible with many other software programs such as all of the Microsoft software, which allow data and plots to be transferred. However, Mathematica also has its drawbacks: it requires a great amount of RAM to do any large complex mathematical analysis. Thus, it is suggested that any large complex analysis be done on a processor with very large memory space.

7.2 Recommendations

There are several areas open for future research. These areas which deserve further research should address are discussed below.

The material used during the numerical investigation of this research was assumed to be homogeneous, isotropic, and linearly elastic. However, woven or braided fabrics for pressurized structures may have different properties in various directions and locations, which may significantly impact the behavior of the structure.

Only four types of loads have been considered in this thesis. Other load types, such as a combination of wind and snow loading or loads acting at an oblique angle, should be investigated as well.

For the general displacement functions discussed in section 3.10.2, more symmetric and non-symmetric terms should be included in order to better understand the behavior of the pressurized arch-shell under various loading conditions.

The boundary conditions for the general loading used clamped bases with radial line springs to restrict movement. A pinned base should be investigated to see how it impacts the behavior of the structure.

APPENDIX A: SAMPLE MATHEMATICA INPUT FILE

Parameters (Non-dimensional terms)

- **Snow load:**

$h = 0.0025$

$p = 500000$

$r = 0.4$

$E_\phi = E_s = 7000000000$

$\nu_\phi = \nu_s = 0.3$

$\hat{\kappa} = \frac{\pi}{100}$

$\hat{z} = 50$

$\xi = \frac{s + \hat{z}}{2\hat{z}}$

$\hat{R}_\phi = 1$

$\hat{R}_s = 1/(\hat{\kappa}\,\mathrm{Cos}[\phi]) + 1$

$\hat{A}_\phi = 1$

$\hat{A}_s = 1 + \hat{\kappa}\,\mathrm{Cos}[\phi]$

$\hat{T}_s = 1/2$

$\hat{T}_{\phi s} = 0$

$\hat{T}_\phi = \frac{(2 + \hat{\kappa}\,\mathrm{Cos}[\phi])}{(2 + 2\hat{\kappa}\,\mathrm{Cos}[\phi])}$

$G_{\phi s} = \frac{E_\phi}{2(1 + \nu_\phi)}\,\frac{1}{p}$

$A_{11} = A_{22} = C_\phi = C_s = \frac{E_\phi\, h}{(1 - \nu_\phi \nu_s)}\,\frac{1}{p\, r}$

$\hat{h} = h/r$

$A_{12} = A_{21} = C_\phi\, \nu_s = C_s\, \nu_\phi$

$A_{66} = C_{66} = G_{\phi s}\, \hat{h}$

$D_{11} = D_\phi = D_{22} = D_s = \frac{E_\phi\, h^3}{12(1 - \nu_\phi \nu_s)}\,\frac{1}{p\, r^3}$

$D_{12} = D_{21} = D_\phi\, \nu_s = D_s\, \nu_\phi$

$D_{66} = \frac{G_{\phi s}\, h^3}{12}\,\frac{1}{r^3}$

The Displacements (without using symmetry)

$$u_\phi[\phi, s] = \sum_{n=1}^{2}\sum_{m=0}^{2}(v_m + v_{1,m,n}\,\mathrm{Cos}[n\phi] + v_{2,m,n}\,\mathrm{Sin}[n\phi])\,\mathrm{Cos}[m\pi\xi]$$

$d_1 = 2v_0$, $d_2 = v_{101}$, $d_3 = v_{201}$, $d_4 = v_{102}$, $d_5 = v_{202}$, $d_6 = 2v_1$, $d_7 = v_{111}$, $d_8 = v_{211}$, $d_9 = v_{112}$, $d_{10} = v_{212}$, $d_{11} = 2v_2$, $d_{12} = v_{121}$, $d_{13} = v_{221}$, $d_{14} = v_{122}$, $d_{15} = v_{222}$

$$u_s[\phi, s] = \sum_{n=1}^{2}\sum_{m=1}^{2}(u_m + u_{1,m,n}\,\mathrm{Cos}[n\phi] + u_{2,m,n}\,\mathrm{Sin}[n\phi])\,\mathrm{Sin}[m\pi\xi]$$

$d_{16} = 2u_1$, $d_{17} = u_{111}$, $d_{18} = u_{211}$, $d_{19} = u_{112}$, $d_{20} = u_{212}$, $d_{21} = 2u_2$, $d_{22} = u_{121}$, $d_{23} = u_{221}$, $d_{24} = u_{122}$, $d_{25} = u_{222}$

$$w[\phi, s] = \sum_{n=1}^{2}\sum_{m=0}^{2}(w_m + w_{1,m,n}\,\mathrm{Cos}[n\phi] + w_{2,m,n}\,\mathrm{Sin}[n\phi])\,\mathrm{Cos}[m\pi\xi]$$

$d_{26} = 2w_0$, $d_{27} = w_{101}$, $d_{28} = w_{201}$, $d_{29} = w_{102}$, $d_{30} = w_{202}$, $d_{31} = 2w_1$, $d_{32} = w_{111}$, $d_{33} = w_{211}$, $d_{34} = w_{112}$, $d_{35} = w_{212}$, $d_{36} = 2w_2$, $d_{37} = w_{121}$, $d_{38} = w_{221}$, $d_{39} = w_{122}$, $d_{40} = w_{222}$

$p_1 = p_{26} = 1$
$p_2 = p_{27} = \mathrm{Cos}[\phi]$
$p_3 = p_{28} = \mathrm{Sin}[\phi]$
$p_4 = p_{29} = \mathrm{Cos}[2\phi]$
$p_5 = p_{30} = \mathrm{Sin}[2\phi]$
$p_6 = p_{31} = \mathrm{Cos}[\pi\xi]$
$p_7 = p_{32} = \mathrm{Cos}[\phi]\,\mathrm{Cos}[\pi\xi]$
$p_8 = p_{33} = \mathrm{Sin}[\phi]\,\mathrm{Cos}[\pi\xi]$
$p_9 = p_{34} = \mathrm{Cos}[2\phi]\,\mathrm{Cos}[\pi\xi]$
$p_{10} = p_{35} = \mathrm{Sin}[2\phi]\,\mathrm{Cos}[\pi\xi]$
$p_{11} = p_{36} = \mathrm{Cos}[2\pi\xi]$
$p_{12} = p_{37} = \mathrm{Cos}[\phi]\,\mathrm{Cos}[2\pi\xi]$
$p_{13} = p_{38} = \mathrm{Sin}[\phi]\,\mathrm{Cos}[2\pi\xi]$
$p_{14} = p_{39} = \mathrm{Cos}[2\phi]\,\mathrm{Cos}[2\pi\xi]$
$p_{15} = p_{40} = \mathrm{Sin}[2\phi]\,\mathrm{Cos}[2\pi\xi]$

$p_{16} = \mathrm{Sin}[\pi\xi]$
$p_{17} = \mathrm{Cos}[\phi]\,\mathrm{Sin}[\pi\xi]$
$p_{18} = \mathrm{Sin}[\phi]\,\mathrm{Sin}[\pi\xi]$
$p_{19} = \mathrm{Cos}[2\phi]\,\mathrm{Sin}[\pi\xi]$
$p_{20} = \mathrm{Sin}[2\phi]\,\mathrm{Sin}[\pi\xi]$
$p_{21} = \mathrm{Sin}[2\pi\xi]$
$p_{22} = \mathrm{Cos}[\phi]\,\mathrm{Sin}[2\pi\xi]$
$p_{23} = \mathrm{Sin}[\phi]\,\mathrm{Sin}[2\pi\xi]$
$p_{24} = \mathrm{Cos}[2\phi]\,\mathrm{Sin}[2\pi\xi]$
$p_{25} = \mathrm{Sin}[2\phi]\,\mathrm{Sin}[2\pi\xi]$

Strain Displacement of Sanders

- **The stiffness matrix for A_{11} term**

$$\hat{\epsilon}_{\phi}[\phi, s] = \frac{1}{\hat{A}_{\phi}} \partial_{\phi} u_{\phi}[\phi, s] + \frac{w[\phi, s]}{\hat{R}_{\phi}}$$

$$\text{Table}[r_i = \partial_{\phi}\, p_i,\ \{i, 1, 15\}]$$

$$\text{Table}[r_i = 0,\ \{i, 16, 25\}]$$

$$\text{Table}[r_i = p_i,\ \{i, 26, 40\}]$$

$$N1 = \text{Table}\left[k_{i,j} = \text{ComplexExpand}\left[\text{Re}\left[\int_{-50}^{50}\int_{0}^{2\pi}\left(A_{11}\hat{A}_s r_i r_j\right) d\phi\, ds\right]\right],\ \{i, 1, 40\},\ \{j, 1, 40\}\right]$$

- **The stiffness matrix for A_{22} term**

$$\hat{\epsilon}_s[\phi, s] = 1/\hat{A}_s \partial_s u_s[\phi, s] + 1\ \left(\hat{A}_{\phi}\hat{A}_s\right) u_{\phi}[\phi, s]\ (-\hat{\kappa}\,\text{Sin}[\phi]) + w[\phi, s]/\hat{R}_s$$

$$\text{Table}\left[t_i = -\frac{\hat{\kappa}\,\text{Sin}[\phi]}{\hat{A}_s}\, p_i,\ \{i, 1, 15\}\right]$$

$$\text{Table}\left[t_i = \frac{1}{\hat{A}_s}\, \partial_s\, p_i,\ \{i, 16, 25\}\right]$$

$$\text{Table}\left[t_i = \frac{1}{\hat{R}_s}\, p_i,\ \{i, 26, 40\}\right]$$

$$N2 = \text{Table}\left[k_{i,j} = \text{ComplexExpand}\left[\text{Re}\left[\int_{-50}^{50}\int_{0}^{2\pi}\left(A_{22}\hat{A}_s t_i t_j\right) d\phi\, ds\right]\right],\ \{i, 1, 40\},\ \{j, 1, 40\}\right]$$

- **The stiffness matrix for A_{12} term**

$$N3 = \text{Table}\left[k_{i,j} = \text{ComplexExpand}\left[\text{Re}\left[\int_{-50}^{50}\int_{0}^{2\pi}\left(A_{12}\hat{A}_s r_i t_j\right) d\phi\, ds\right]\right],\ \{i, 1, 40\},\ \{j, 1, 40\}\right]$$

$$N4 = \text{Table}\left[k_{i,j} = \text{ComplexExpand}\left[\text{Re}\left[\int_{-50}^{50}\int_{0}^{2\pi}\left(A_{12}\hat{A}_s t_i r_j\right) d\phi\, ds\right]\right],\ \{i, 1, 40\},\ \{j, i, 40\}\right]$$

- **The stiffness matrix for A_{66} term**

$$\hat{\gamma}_{\phi s}[\phi, s] = \frac{1}{\hat{A}_{\phi}\hat{A}_s}\left(\hat{A}_s \partial_{\phi} u_s[\phi, s] + \hat{A}_{\phi} \partial_s u_{\phi}[\phi, s] - u_s[\phi, s]\ (-\hat{\kappa}\,\text{Sin}[\phi])\right)$$

$$\text{Table}\left[f_i = \frac{1}{\hat{A}_s}\, \partial_s\, p_i,\ \{i, 1, 15\}\right]$$

$$\text{Table}\left[f_i = \partial_{\phi}\, p_i + \frac{\hat{\kappa}\,\text{Sin}[\phi]}{\hat{A}_s}\, p_i,\ \{i, 16, 25\}\right]$$

$$\text{Table}[f_i = 0,\ \{i, 26, 40\}]$$

$$N5 = \text{Table}\left[k_{i,j} = \text{ComplexExpand}\left[\text{Re}\left[\int_{-50}^{50}\int_{0}^{2\pi}\left(A_{66}\hat{A}_s f_i f_j\right) d\phi\, ds\right]\right],\ \{i, 1, 40\},\ \{j, 1, 40\}\right]$$

- **The stiffness matrices to restrict outward movement at the ends**

```
s = -50

p26 = 1
p27 = Cos[ϕ]
p28 = Sin[ϕ]
p29 = Cos[2 ϕ]
p30 = Sin[2 ϕ]
p31 = Cos[π ξ]
p32 = Cos[ϕ] Cos[π ξ]
p33 = Sin[ϕ] Cos[π ξ]
p34 = Cos[2 ϕ] Cos[π ξ]
p35 = Sin[2 ϕ] Cos[π ξ]
p36 = Cos[2 π ξ]
p37 = Cos[ϕ] Cos[2 π ξ]
p38 = Sin[ϕ] Cos[2 π ξ]
p39 = Cos[2 ϕ] Cos[2 π ξ]
p40 = Sin[2 ϕ] Cos[2 π ξ]

Table[Ni = 0, {i, 1, 15}]

Table[Ni = 0, {i, 16, 25}]

Table[Ni = pi, {i, 26, 40}]

N6 = Table[ki,j = ComplexExpand[Re[c ∫_0^{2π} (Ni Nj) dϕ]], {i, 1, 40}, {j, 1, 40}]

s = 50

p26 = 1
p27 = Cos[ϕ]
p28 = Sin[ϕ]
p29 = Cos[2 ϕ]
p30 = Sin[2 ϕ]
p31 = Cos[π ξ]
p32 = Cos[ϕ] Cos[π ξ]
p33 = Sin[ϕ] Cos[π ξ]
p34 = Cos[2 ϕ] Cos[π ξ]
p35 = Sin[2 ϕ] Cos[π ξ]
p36 = Cos[2 π ξ]
p37 = Cos[ϕ] Cos[2 π ξ]
p38 = Sin[ϕ] Cos[2 π ξ]
p39 = Cos[2 ϕ] Cos[2 π ξ]
p40 = Sin[2 ϕ] Cos[2 π ξ]
```

$\text{Table}[N_i = 0, \{i, 1, 15\}]$

$\text{Table}[N_i = 0, \{i, 16, 25\}]$

$\text{Table}[N_i = p_i, \{i, 26, 40\}]$

$N7 = \text{Table}\left[k_{i,j} = \text{ComplexExpand}\left[\text{Re}\left[c \int_0^{2\pi} (N_i N_j)\, d\phi\right]\right], \{i, 1, 40\}, \{j, 1, 40\}\right]$

- **The stiffness matrix for T_ϕ term**

$\text{Table}[ta_i = p_i, \{i, 1, 15\}]$

$\text{Table}[ta_i = 0, \{i, 16, 25\}]$

$\text{Table}[ta_i = -\partial_\phi\, p_i, \{i, 26, 40\}]$

$N8 = \text{Table}\left[k_{i,j} = \text{ComplexExpand}\left[\text{Re}\left[\int_{-50}^{50}\int_0^{2\pi} \left(\hat{T}_\phi\, \hat{A}_s\, ta_i\, ta_j\right) d\phi\, ds\right]\right], \{i, 1, 40\}, \{j, 1, 40\}\right]$

- **The stiffness matrix for T_s term**

$\text{Table}[tb_i = 0, \{i, 1, 15\}]$

$\text{Table}\left[tb_i = \frac{1}{\hat{R}_s}\, p_i, \{i, 16, 25\}\right]$

$\text{Table}\left[tb_i = -\frac{1}{\hat{A}_s}\, \partial_s\, p_i, \{i, 26, 40\}\right]$

$N9 = \text{Table}\left[k_{i,j} = \text{ComplexExpand}\left[\text{Re}\left[\frac{1}{2} \int_{-50}^{50}\int_0^{2\pi} \left(\hat{A}_s\, tb_i\, tb_j\right) d\phi\, ds\right]\right], \{i, 1, 40\}, \{j, 1, 40\}\right]$

- **The stiffness matrix for D_{11} term**

$$\hat{\kappa}_\phi[\phi, s] = \frac{1}{\hat{A}_\phi}\, \partial_\phi \left(\frac{u_\phi[\phi, s]}{\hat{R}_\phi} - \frac{1}{\hat{A}_\phi}\, \partial_\phi\, w[\phi, s]\right)$$

$\text{Table}[G_i = \partial_\phi\, p_i, \{i, 1, 15\}]$

$\text{Table}[G_i = 0, \{i, 16, 25\}]$

$\text{Table}[G_i = -\partial_\phi\, (\partial_\phi\, p_i), \{i, 26, 40\}]$

$N10 = \text{Table}\left[k_{i,j} = \text{ComplexExpand}\left[\text{Re}\left[\int_{-50}^{50}\int_0^{2\pi} \left(D_{11}\, \hat{A}_s\, G_i\, G_j\right) d\phi\, ds\right]\right], \{i, 1, 40\}, \{j, 1, 40\}\right]$

- **The stiffness matrix for D_{22} term**

$$\hat{\kappa}_s[\phi, s] = \frac{1}{\hat{A}_s}\, \partial_s \left(\frac{u_s[\phi, s]}{\hat{R}_s} - \frac{1}{\hat{A}_s}\, \partial_s\, w[\phi, s]\right) + \frac{1}{\hat{A}_\phi\, \hat{A}_s}\, (-\hat{\kappa}\, \text{Sin}[\phi]) \left(\frac{u_\phi[\phi, s]}{\hat{R}_\phi} - \frac{1}{\hat{A}_\phi}\, \partial_\phi w[\phi, s]\right)$$

$\text{Table}\left[H_i = -\frac{\hat{\kappa}\, \text{Sin}[\phi]}{\hat{A}_s}\, p_i, \{i, 1, 15\}\right]$

$\text{Table}\left[H_i = \frac{1}{\hat{A}_s}\, \partial_s \left(\frac{p_i}{\hat{R}_s}\right), \{i, 16, 25\}\right]$

$\text{Table}\left[H_i = \text{Simplify}\left[\frac{\hat{\kappa}\, \text{Sin}[\phi]}{\hat{A}_s}\, \partial_\phi\, p_i - \frac{1}{\hat{A}_s}\, \partial_s \left(\frac{\partial_s\, p_i}{\hat{A}_s}\right)\right], \{i, 26, 40\}\right]$

$$N11 = \text{Table}\left[k_{i,j} = \text{ComplexExpand}\left[\text{Re}\left[\int_0^{2\pi}\int_{-50}^{50}\left(D_{22}\,\hat{A}_s\,H_i\,H_j\right)\,ds\,d\phi\right]\right],\ \{i,1,40\},\ \{j,1,40\}\right]$$

- **The stiffness matrix for D_{12} term**

$$N12 = \text{Table}\left[k_{i,j} = \text{ComplexExpand}\left[\text{Re}\left[\int_{-50}^{50}\int_0^{2\pi}\left(D_{12}\,\hat{A}_s\,G_i\,H_j\right)\,d\phi\,ds\right]\right],\ \{i,1,40\},\ \{j,1,40\}\right]$$

$$N13 = \text{Table}\left[k_{i,j} = \text{ComplexExpand}\left[\text{Re}\left[\int_{-50}^{50}\int_0^{2\pi}\left(D_{12}\,\hat{A}_s\,H_i\,G_j\right)\,d\phi\,ds\right]\right],\ \{i,1,40\},\ \{j,1,40\}\right]$$

- **The stiffness matrix for D_{66} term**

$$\overline{\kappa_{\hat{\phi}}}\,s[\phi, s] = 1\ \left(2\,\hat{A}_\phi\,\hat{A}_s\right)\left(\hat{A}_s\,\partial_\phi\left(u_s[\phi, s]/\hat{R}_s - 1/\hat{A}_s\,\partial_s\,w[\phi, s]\right) + \hat{A}_\phi\,\partial_s\left(u_\phi[\phi, s]/\hat{R}_\phi - 1/\hat{A}_\phi\,\partial_\phi\,w[\phi, s]\right) - (-\hat{\kappa}\,\text{Sin}[\phi])\left(u_s[\phi, s]/\hat{R}_s - 1/\hat{A}_s\,\partial_s\,w[\phi, s]\right) + 1/2\left(1/\hat{R}_s - 1/\hat{R}_\phi\right)\left(\partial_\phi\left(\hat{A}_s\,u_s[\phi, s]\right) - \partial_s\left(\hat{A}_\phi\,u_\phi[\phi, s]\right)\right)\right)$$

$$\text{Table}\left[L_i = \text{Simplify}\left[\frac{1}{2\,\hat{A}_s}\left(\frac{1}{2}\left(3 - \frac{1}{\hat{R}_s}\right)\partial_s\,p_i\right)\right],\ \{i,1,15\}\right]$$

$$\text{Table}\left[L_i = \text{Simplify}\left[\frac{1}{2\,\hat{A}_s}\left(\hat{A}_s\,\partial_\phi\left(\frac{p_i}{\hat{R}_s}\right) + \frac{\hat{\kappa}\,\text{Sin}[\phi]}{\hat{R}_s}\,p_i + \frac{1}{2}\left(\frac{1}{\hat{R}_s} - 1\right)\partial_\phi\left(\hat{A}_s\,p_i\right)\right)\right],\ \{i,16,25\}\right]$$

$$\text{Table}\left[L_i = \text{Simplify}\left[\frac{1}{2\,\hat{A}_s}\left(-\hat{A}_s\,\partial_\phi\left(\frac{\partial_s\,p_i}{\hat{A}_s}\right) - \partial_s\,\partial_\phi\,p_i - \frac{\hat{\kappa}\,\text{Sin}[\phi]}{\hat{A}_s}\,\partial_s\,p_i\right)\right],\ \{i,26,40\}\right]$$

$$N14 = \text{Table}\left[k_{i,j} = \text{ComplexExpand}\left[\text{Re}\left[4\int_{-50}^{50}\int_0^{2\pi}\left(D_{66}\,\hat{A}_s\,L_i\,L_j\right)\,d\phi\,ds\right]\right],\ \{i,1,40\},\ \{j,i,40\}\right]$$

- **The load terms under full snow load**

$$\gamma = \int_0^s \hat{\kappa}\,ds$$

$$q_\phi[\phi, s] = F_0\,(\text{Cos}[\gamma])^2\,\text{Sin}[\phi]\,\text{Cos}[\phi]$$

$$\text{Table}\left[m_i = \int_{-16.67}^{16.67}\int_{-\frac{\pi}{6}}^{\frac{\pi}{6}}\left(q_\phi[\phi, s]\,p_i\,\hat{A}_s\right)\,d\phi\,ds,\ \{i,1,15\}\right]$$

$$q_s[\phi, s] = F_0\,(\text{Sin}[\gamma])\,(\text{Cos}[\gamma])\,\text{Cos}[\phi]$$

$$\text{Table}\left[m_i = \int_{-16.67}^{16.67}\int_{-\frac{\pi}{6}}^{\frac{\pi}{6}}\left(q_s[\phi, s]\,p_i\,\hat{A}_s\right)\,d\phi\,ds,\ \{i,16,25\}\right]$$

$$q_n[\phi, s] = -F_0\,(\text{Cos}[\gamma])^2\,(\text{Cos}[\phi])^2$$

$$\text{Table}\left[m_i = \int_{-16.67}^{16.67}\int_{-\frac{\pi}{6}}^{\frac{\pi}{6}}\left(q_n[\phi, s]\,p_i\,\hat{A}_s\right)\,d\phi\,ds,\ \{i,26,40\}\right]$$

$$B = \text{Table}[m_i,\ \{i,1,40\}]$$

- **Solutions**

$$Sol1 = N1 + N2 + N3 + N4 + N5 + N6 + N7 + N8 + N9 + N10 + N12 + N13 + N14$$

$$Soln = \text{LinearSolve}[Sol1, B]$$

$$\text{Table}[d_i = Soln[[i]],\ \{i,1,40\}]$$

- **The moment M_S and stresses N_ϕ and N_S under full snow load**

$$u_\phi[\phi, S] = \sum_{i=1}^{15} d_i\, p_i$$

$$u_S[\phi, S] = \sum_{i=16}^{25} d_i\, p_i$$

$$w[\phi, S] = \sum_{i=26}^{40} d_i\, p_i$$

$$\hat{\epsilon}_\phi[\phi, S] = \frac{1}{\hat{A}_\phi}\, \partial_\phi\, u_\phi[\phi, S] + \frac{w[\phi, S]}{\hat{R}_\phi}$$

$$\hat{\epsilon}_S[\phi, S] = 1/\hat{A}_S\, \partial_S\, u_S[\phi, S] + 1 \quad \left(\hat{A}_\phi\, \hat{A}_S\right) u_\phi[\phi, S]\, (-\hat{\kappa}\, \mathrm{Sin}[\phi]) + w[\phi, S] / \hat{R}_S$$

$$\hat{\kappa}_\phi[\phi, S] = \frac{1}{\hat{A}_\phi}\, \partial_\phi \left(\frac{u_\phi[\phi, S]}{\hat{R}_\phi} - \frac{1}{\hat{A}_\phi}\, \partial_\phi\, w[\phi, S]\right)$$

$$\hat{\kappa}_S[\phi, S] = \frac{1}{\hat{A}_S}\, \partial_S \left(\frac{u_S[\phi, S]}{\hat{R}_S} - \frac{1}{\hat{A}_S}\, \partial_S\, w[\phi, S]\right) +$$

$$\frac{1}{\hat{A}_\phi\, \hat{A}_S}\, (-\hat{\kappa}\, \mathrm{Sin}[\phi]) \left(\frac{u_\phi[\phi, S]}{\hat{R}_\phi} - \frac{1}{\hat{A}_\phi}\, \partial_\phi\, w[\phi, S]\right)$$

$$\hat{N}_\phi = \frac{E_\phi\, h}{1 - \nu_\phi\, \nu_S}\, \frac{1}{p\, r}\, (\hat{\epsilon}_\phi[\phi, S] + \nu_S\, \hat{\epsilon}_S[\phi, S])$$

$$\hat{N}_S = \frac{E_S\, h}{1 - \nu_\phi\, \nu_S}\, \frac{1}{p\, r}\, (\hat{\epsilon}_S[\phi, S] + \nu_\phi\, \hat{\epsilon}_\phi[\phi, S])$$

$$\hat{M}_S = \frac{E_S\, h^3}{12\, (1 - \nu_\phi\, \nu_S)}\, \frac{1}{p\, r^3}\, (\hat{\kappa}_S[\phi, S] + \nu_\phi\, \hat{\kappa}_\phi[\phi, S])$$

$$S1 = \hat{N}_\phi + \hat{T}_\phi$$

$$S2 = \hat{N}_S + \hat{T}_S$$

REFERENCES

Carradine, D. M. (1998). "Experiments on the Response of Arch-Supported Membrane Shelters to Snow and Wind Loading," Master's Thesis, Virginia Polytechnic Institute and State University, Blacksburg, VA.

Dym. C. L. (1990). *Introduction to the Theory of Shells*. Hemisphere, New York.

Gould, P. L. (1988). *Analysis of Shells and Plates*. Springer-Verlag, New York.

Jones, R. M. (1975). *Mechanics of Composite Materials*. Hemisphere, New York.

Kim, J.-Y, Plaut, R. H. and Kwun, T.-J. (1998). "Analysis of Tent-Like Structures Supported by Pressurized Fabric Arches," *Lightweight Structures in Architecture, Engineering and Construction.* (LSA98), Vol. 2, Edited by R. Hough and R. Melchers, pp. 821-829.

Kigudde, M. (1996). "General Formulation of Equations for Arch-Tube," Progress Report, Virginia Polytechnic Institute and State University, Blacksburg, VA.

Mohan, P., and Kapania, R. K. (1998a). "Analysis of General Shells Under Deformation Dependent Pressure Loads Using a Flat Triangular Shell Element," Proceedings of 39th Structures, Structural Dynamics and Materials Conference, AIAA, Reston, VA, pp. 534-541.

Mohan, P., and Kapania, R. K. (1998b). "Updated Lagrangian Formulation of a Flat Triangular Element for Thin Laminated Shells," *AIAA Journal*, Vol. 36, pp. 273-281.

Molloy, S. J. (1998). "Finite Element Analysis of a Pair of Leaning Pressurized Arch-Shells Under Snow and Wind Loads," Master's Thesis, Virginia Polytechnic Institute and State University, Blacksburg, VA.

Plaut, R. H. (1997). Notes.

Plaut, R. H. (1998). Notes.

Reddy, J. N. (1984). *Energy and Variational Methods in Applied Mechanics*. John Wiley and Sons, New York.

Sanders, Jr., J. L. (1959). "An Improved First-Approximation Theory for Thin Shells," NASA Technical Report R-24, NASA, Washington D. C.

Soare, M. (1967). *Application of Finite Difference Equations to Shell Analysis*, Pergamon Press, New York.

Szilard, R. (1974). *Theory and Analysis of Plates: Classical and Numerical Methods*, Prentice-Hall, Englewood Cliffs, NJ.

Zhang, F., and Redekop, D. (1992a). "Comparison of Elastic Solutions for Three-Point Bending of Curved Pipes," *Thin-Walled Structures*, Vol. 14, pp. 223-239.

Zhang, F., and Redekop, D. (1992b). "Local Loads on a Toroidal Shell," *Journal of Strain Analysis*, Vol. 27, pp.59-66.

Zhang, F., and Redekop, D. (1992c). "Surface Loading of a Thin-Walled Toroidal Shell," *Computers and Structures*, Vol. 43, pp. 1019-1038.

Wolfram, S. (1996). *Mathematica: A System of Doing Mathematics by Computer*, 3rd edition, Wolfram Research, Inc., Champaign, IL.

VITA

Julian Goh Kok Seng was born in Kuching, Sarawak, Malaysia, on July 8, 1974. He graduated Magna Cum Laude from Michigan Technological University in December 1996 with a Bachelor of Science degree in Civil Engineering. He worked as an intern in the summers of 1996 and 1997 with Sarawak Structural Engineers, a consulting firm based in Kuching, Malaysia. In December of 1998, he received a Master of Science degree in Civil Engineering from Virginia Polytechnic Institute and State University.